

Study of Irradiation Effects in Reduced Activation Ferritic/Martensitic Steel Using Positron Beam Based Doppler Broadening Spectroscopy

By

RENJITH RAMACHANDRAN

Enrolment No: PHYS 02 2013 04 011

Indira Gandhi Centre for Atomic Research, Kalpakkam

*A thesis submitted to the
Board of Studies in Physical Sciences
In partial fulfillment of requirements
for the Degree of
DOCTOR OF PHILOSOPHY
of
HOMI BHABHA NATIONAL INSTITUTE*



July, 2019

Homi Bhabha National Institute

Recommendations of the Viva Voce Committee

As members of the Viva Voce Committee, we certify that we have read the dissertation prepared by Renjith Ramachandran entitled "Study of Irradiation Effects in Reduced Activation Ferritic/Martensitic Steel Using Positron Beam Based Doppler Broadening Spectroscopy" and recommend that it may be accepted as fulfilling the thesis requirement for the award of Degree of Doctor of Philosophy.

N.V. Chandra Shekar

26/11/19

Chairman- Prof. N. V. Chandra Shekar

Date:

G. Amarendra

Nov 26, 2019

Guide / Convener- Prof. G. Amarendra

Date:

K. Sivaji

26/11/19

Examiner - Dr. K. Sivaji

Date:

M. Kamruddin

26/11/19

Member 1- Prof. M. Kamruddin

Date:

R. Rajaraman

26/11/19

Member 2- Prof. R. Rajaraman

Date:

A. Dasgupta

26/11/19

Member 3- Dr. Arup Dasgupta

Date:

Final approval and acceptance of this thesis is contingent upon the candidate's submission of the final copies of the thesis to HBNI.

I hereby certify that I have read this thesis prepared under my direction and recommend that it may be accepted as fulfilling the thesis requirement.

Date: NOV 26, 2019

Place: IGCAR, Kalpakkam

G. Amarendra
(Prof. G. Amarendra)
Thesis Supervisor

STATEMENT BY AUTHOR

This dissertation has been submitted in partial fulfillment of requirements for an advanced degree at Homi Bhabha National Institute (HBNI) and is deposited in the library to be made available to borrowers under rules of the HBNI.

Brief quotations from this dissertation are allowable without special permission, provided that accurate acknowledgement of source is made. Requests for permission for extended quotation from or reproduction of this manuscript in whole or in part may be granted by the Competent Authority of HBNI when in his or her judgment the proposed use of the material is in the interests of scholarship. In all other instances, however, permission must be obtained from the author.



(Renjith Ramachandran)

Ph.D Candidate

DECLARATION

I, hereby declare that the investigation presented in the thesis has been carried out by me. The work is original and has not been submitted earlier as a whole or in part for a degree / diploma at this or any other Institution / University.



(Renjith Ramachandran)

Ph.D Candidate

LIST OF PUBLICATIONS

Journals

Published:

1. **Renjith Ramachandran**, C. David, R. Rajaraman, B. K. Panigrahi and G. Amarendra, “*Evolution, migration and clustering of helium-vacancy complexes in RAFM steel-depth resolved positron annihilation Doppler broadening study*”, Philosophical Magazine, **96** (2016), pp. 2385-2396.
2. **Renjith Ramachandran**, Sujay Chakravarty, S. Balaji, Padmalochan Panda, C. David, R. Rajaraman, R. Ramaseshan, R. Govindaraj and G. Amarendra, “*Study of vacancy defects and their thermal stability in MeV Fe ion irradiated RAFM steel using positron beam Doppler broadening spectroscopy*”, Philosophical Magazine, **99** (2019), pp. 38-54.
3. **Renjith Ramachandran**, C. David, P. Magudapathy, R. Rajaraman, R. Govindaraj and G. Amarendra, “*Study of defect complexes and their evolution with temperature in hydrogen and helium irradiated RAFM steel using positron annihilation spectroscopy*”, Fusion Engineering and Design **142** (2019), pp. 55-62.

Under Preparation:

1. **Renjith Ramachandran**, C. David, P. Magudapathy, R. Rajaraman and G. Amarendra, “*High-temperature irradiation damage studies in RAFM steel at fusion relevant He/dpa Ratio*”, (manuscript under preparation).

Conferences:

1. **Renjith Ramachandran**, C. David, R. Rajaraman, B. K. Panigrahi, and G. Amarendra, “*Investigation of helium implanted RAFM steel by positron annihilation Doppler broadening spectroscopy*”, Positron and Positronium Chemistry (PPC-11), November 9-14, 2014, Goa.
2. **Renjith Ramachandran**, C. David, R. Rajaraman, S. Abhaya, B. K. Panigrahi, and G. Amarendra, “*Isochronal annealing studies on 1.1 MeV Fe ion irradiated RAFM steel*

using variable energy slow positron beam”, AIP conference proceedings **1832** (2017), p. 080045.

3. **Renjith Ramachandran**, C. David, R. Rajaraman, R. Govindaraj and G. Amarendra, “*Effect of hydrogen on the formation and growth of He-vacancy clusters in RAFM steel studied using positron beam Doppler broadening spectroscopy*”, Third DAE-BRNS Trombay positron meeting (Positron 2018), March 23-24, 2018, BARC, Mumbai.

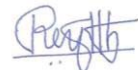
Other Publications (not included in thesis)

Journals

1. R. Ramani, V. Das, A. Singh, **Renjith Ramachandran**, G. Amarendra, and S. Alam, “*Free volume study on the origin of dielectric constant in a fluorine containing polyimide blend: poly(vinylidene fluoride-co-hexa fluoropropylene)/poly(ether imide)*”, *The journal of physical chemistry B* **118** (2014), pp. 12282-12296.
2. Deepalekshmi Ponnamma, **Renjith Ramachandran**, Shamima Hussain, R.Rajaraman, G. Amarendra, K. T. Varughese, and Sabu Thomas, “*Free volume correlation with mechanical and dielectric properties of natural rubber/multi walled carbon nanotubes composites*”, *Composites: Part A* **77** (2015), pp. 164-171.
3. R. Ramani, T. M. Kotresh, R. Indu Shekar, F. Sanal, U. K. Singh, **Renjith Ramachandran** and G. Amarendra, “*Positron probes free volume to identify para- and meta-aramid fibres and correlation with mechanical strength*”, *Polymer* **135** (2018), pp. 39-49.
4. Elizabeth Francis, Lindong Zhai, Hyun Chan Kim, **Renjith Ramachandran**, G. Amarendra, G. M. Balerao, Nandakumar Kalarikkal, K. T. Varughese, Jaehwan Kim and Sabu Thomas, “*Morphology correlated free volume studies of multi-walled carbon nanotube plasticized poly (vinyl chloride) nano composites: positronium probes and electrical properties*”, *Polymer* **141** (2018), pp. 232-243.
5. Sitakanta Panda, P. Vinodkumar, U. Madhusoodanan, **Renjith Ramachandran**, V. Sridharan and B. S. Panigrahi, “*Synthesis, characterization and optical properties of BaCeO₃:Eu-An efficient red phosphor for w-LED applications*”, *Journal of Luminescence* **214** (2019), p. 116538.

Conferences

1. R. Ramani, **Renjith Ramachandran**, G. Amarendra and S. Alam, “*Direct correlation between free volume and dielectric constant in a fluorine containing polyimide blend*”, Journal of physics: conference series **618** (2015), p. 012025.
2. Alaka Panda, L. Herojit Singh, S. Rajagopalan, R. Govindaraj, **Renjith Ramachandran**, S. Kalavathi, and G. Amarendra, “*Mossbauer spectroscopic studies in U-Fe and U-Fe-Zr alloys*”, AIP conference proceedings **1731** (2016), p. 140065.
3. P. A. Manojkumar, G. Mangamma, **Renjith Ramachandran**, Nandagopala Krishna, P. Magudapathy, S. Ilango, S.K. Dhara, M. Kamruddin, and S.K. Albert, “*Probing the evolution of chemical state and defect structure due to N^+ and N^{2+} ion implantation on zirconium thin film*”, ICONSTAT-2018, March 21-23, 2018, Bengaluru.
4. J. Parimala, S. Abhaya, **Renjith Ramachandran**, R. Rajaraman and G. Amarendra, “*Automation of variable low energy positron beam experiments using LabVIEW based programme*”, Symposium on Nuclear and Radiochemistry (NUCAR-2019), January 15-19, 2019, BARC, Mumbai.
5. R. Ramani, T. M. Kotresh, R. Indu Shekhar, U. K. Singh, **Renjith Ramachandran** and G. Amarendra, “*Free volume properties of high performance aramid fibers*”, World Chemistry Conference and Exhibition (WCCE-2019), June 13-15, 2019, Brussels, Belgium.



(Renjith Ramachandran)

Ph.D Candidate

**DEDICATED TO
MY FAMILY**

ACKNOWLEDGEMENTS

Foremost, I express sincere gratitude to my research supervisor Dr. G. Amarendra, Director, Materials Science Group, for his guidance, support, and motivation during the Ph.D work. I thank him for his extreme patience and freedom given to me during this period. I consider myself to be extremely privileged to have been his student.

I thank my doctoral committee members Dr. N. V. Chandra Shekar, Head, CMPD, Dr. M. Kamruddin, Associate Director, ANG, MSG and Dr. Arup Dasgupta, Head, SAMS, MMG for their support and valuable suggestions. I thank my former doctoral committee members Dr. C. S. Sundar and Dr. Sitaram Dash, for their support and suggestions.

I thankfully acknowledge Dr. A. K. Bhaduri, Director, IGCAR and former directors Dr. S. A. V. Satya Murty, Dr. P. R. Vasudeva Rao and Mr. S. C. Chetal for their permission for pursuing higher studies.

I express my gratitude to Dr. R. Rajaraman, Head, MPS, MSG for his suggestions and encouragement.

I am grateful to Dr. R. Govindaraj, Head, MPD, MSG for his suggestions and encouragement.

I thank Ms. M. Premila for her advice, suggestions and careful reading of my thesis. I thank Ms. J. Parimala for providing electronic support to maintain the instruments. I thank Dr. G. Venugopal Rao for all his suggestions and help in my personal and professional life.

I thank Dr. Varghese Anto Chirayath for introducing me to positron annihilation spectroscopy and initial training.

I am deeply indebted to Dr. C. David, Head, ARDS, MSG for all irradiations and discussions during this period.

I express my deep gratitude to Dr. P. Magudapathy for hydrogen and helium irradiations. I thank Dr. S. Balaji and Ms. Julie for Fe ion irradiation. I thank Dr. Sujay Chakravarthi for GIXRD measurements. I also thank Dr. R. Ramaseshan and Dr. Padmalochan Panda for nanoindentation measurements. I express my gratitude to Dr. A. K. Balamurugan for SIMS measurements and discussions. I am thankful to Mr. Siva Kumar, Mr. Pradyumna Kumar Parida for FIB sample preparation, and Ms. Alphy George for TEM analysis. I thank Dr. K. Laha for providing INRAFM samples.

I thank Dr. K. Vinod for his friendship and care. I thank Dr. C. Lakshmanan for reading my thesis and all his help during this period. I also thank my MPS colleagues Dr. S. Abhaya, Mr. V. Ragunathan, Dr. T. N. Sairam, Mr. Ravi Kumar Yadav, Ms. Parvathy for

their support and well wishes. I also thank Dr. Gurpreet Kaur for discussions. I thank Mr. Manoj Kumar and P. Jegadeesan for all their help during the preparation of thesis. I also acknowledge members of liquid nitrogen plant for uninterrupted supply of liquid nitrogen. I thank office staffs of CMPD, MSG and HBNI for all their help during my Ph.D.

I thank Elsevier, Taylor & Francis and Springer publishing groups for all copyright permissions.

I also gratefully acknowledge all of my teachers who taught me at various stages.

And last but not least; I thank my family for all their love, support, and understanding.

(Renjith Ramachandran)

Table of Contents

| | |
|----------------------------|--------|
| LIST OF PUBLICATIONS | viii |
| ACKNOWLEDGEMENTS | xiv |
| ABSTRACT | xx |
| LIST OF FIGURES | xxii |
| LIST OF TABLES | xxviii |

Chapter 1 Introduction 1

| | |
|----------------------------------------------------------------------------------------|----|
| 1.1. Preamble | 1 |
| 1.2. Radiation resistant steels..... | 1 |
| 1.3. Fusion reactor program and the need for low activation structural materials | 2 |
| 1.4. Reduced Activation Ferritic/Martensitic (RAFM) steel | 3 |
| 1.5. Indian Reduced Activation Ferritic/Martensitic (INRAFM) steel..... | 4 |
| 1.6. Irradiation effects in materials | 6 |
| 1.7. Radiation damage models..... | 9 |
| 1.8. Helium diffusion mechanisms in metals..... | 11 |
| 1.8.1. Helium diffusion at low radiation damage conditions | 11 |
| 1.8.2. Helium diffusion under normal irradiation conditions..... | 12 |
| 1.9. Helium bubble nucleation and growth mechanisms upon irradiation | 14 |
| 1.9.1. Helium bubble nucleation during implantation..... | 15 |
| 1.9.2. He bubble coarsening mechanisms up on post-irradiation annealing | 18 |
| 1.9.3. Equilibrium pressure and mechanical stability limit of bubbles | 19 |
| 1.10. Hydrogen trapping in materials | 20 |
| 1.11. Experimental investigation of irradiation-induced microstructural changes..... | 21 |
| 1.12. Positron Annihilation Spectroscopy (PAS) | 22 |
| 1.13. Study of irradiation effects in materials using PAS..... | 26 |
| 1.14. Motivation for present work | 28 |

Chapter 2 Experimental Methods 31

| | |
|----------------------------------------------------------------------------------|----|
| 2.1. Introduction..... | 31 |
| 2.2. Sample preparation | 31 |
| 2.3. Helium and hydrogen ion irradiations | 32 |
| 2.4. Fe ion irradiation..... | 33 |
| 2.5. Variable low-energy positron beam based Doppler broadening spectroscopy.... | 35 |
| 2.6. Secondary Ion Mass Spectrometry (SIMS) | 41 |
| 2.7. Transmission Electron Microscopy (TEM) | 42 |
| 2.8. Grazing Incidence X-ray Diffraction (GIXRD)..... | 42 |
| 2.9. Nanoindentation..... | 43 |
| 2.10. Summary | 45 |

| | |
|-----------------------------------------------------------------------------------------------------------------|-----------|
| Chapter 3 Nucleation and growth of helium-vacancy complexes in RAFM steel..... | 47 |
| 3.1. Introduction..... | 47 |
| 3.2. Experimental..... | 48 |
| 3.2.1. Helium ion irradiation | 48 |
| 3.2.2. Secondary Ion Mass Spectrometry..... | 49 |
| 3.2.3. Positron annihilation studies | 49 |
| 3.2.4. Transmission Electron Microscopy..... | 50 |
| 3.3. Results and discussion | 50 |
| 3.3.1. Secondary Ion Mass Spectrometry study | 50 |
| 3.3.2. Positron annihilation studies | 52 |
| 3.3.3. Transmission Electron Microscopy study | 63 |
| 3.4. Summary | 64 |
| Chapter 4 Effect of sequential irradiation of hydrogen and helium in RAFM steel | 67 |
| 4.1. Introduction..... | 67 |
| 4.2. Experimental..... | 68 |
| 4.3. Results and discussion | 69 |
| 4.3.1. Defect studies in as-irradiated samples | 69 |
| 4.3.2. Isochronal annealing studies | 72 |
| 4.4. Conclusion | 81 |
| Chapter 5 Study of vacancy defects and their thermal stability in MeV Fe ion irradiated RAFM steel | 83 |
| 5.1. Introduction..... | 83 |
| 5.2. Experimental..... | 84 |
| 5.2.1. Irradiation procedure | 84 |
| 5.2.2. Positron annihilation studies | 85 |
| 5.2.3. GIXRD studies | 85 |
| 5.2.4. Nanoindentation studies | 87 |
| 5.3. Results and discussion | 87 |
| 5.3.1. Defect recovery under isochronal annealing in low-dose (0.1 dpa) sample..... | 87 |
| 5.3.2. Defect studies in as-irradiated high-dose (1-100 dpa) samples..... | 91 |
| 5.3.3. Defect-recovery under isochronal annealing in 1 dpa and 100 dpa samples | 100 |
| 5.3.4. High-temperature irradiation studies..... | 103 |
| 5.4. Conclusion | 108 |

| | |
|--------------------------------------------------------|------------|
| <i>Chapter 6 Summary and future scope</i> | 109 |
| 6.1. Summary of the thesis..... | 109 |
| 6.2. Future scope..... | 110 |
| <i>References</i> | 112 |

Chapter 1

Introduction

1.1. Preamble

The core structural materials of a nuclear reactor undergo severe displacement damage due to neutron irradiation. The gases such as helium and hydrogen introduced by nuclear transmutation reactions further complicate the issue by stabilizing the irradiation-induced vacancies against the vacancy-interstitial recombination. The survival and growth of irradiation-induced defects during normal reactor operation conditions lead to the loss of ductility and premature failure of the core-structural materials. In fusion reactors, material degradation is even faster due to the synergistic effect of hydrogen and helium produced along with high displacement damage. Apart from the desirable mechanical and high-temperature properties, low induced-activity is another requirement that ensures the safe and easy disposal of spent nuclear core components. Low activation steels have been developed in many countries as a part of the Test Blanket Module (TBM) development programme of the International Thermonuclear Experimental Reactor (ITER) project. In India, Indian Reduced Activation Ferritic/Martensitic (INRAFM) steel has been developed as a structural material for Indian Lead-Lithium Ceramic Breeder Test Blanket module (LLCB-TBM) in ITER. Scope of this thesis work is to study the irradiation effects in INRAFM steel at conditions that are relevant to fusion reactor first-wall environment. Study of defect-complexes induced by hydrogen and helium irradiation and their thermal evolution is one of the prime focuses of the thesis. This chapter discusses about the classification of radiation-resistant steels, proposed low-activation materials for fusion reactors, Indian TBM in ITER and INRAFM steel, irradiation effects in materials, helium migration mechanisms at various irradiation environments, helium bubble nucleation and growth mechanisms, hydrogen traps in materials, positron annihilation spectroscopic techniques and their effectiveness in studying irradiation effects in materials.

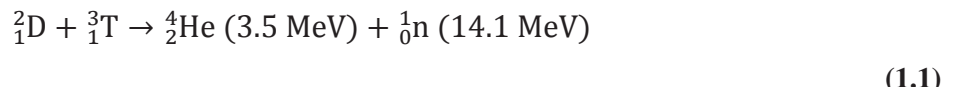
1.2. Radiation resistant steels

Core-structural components in nuclear reactors must possess adequate resistance to neutron-induced displacement damage, better thermal conductivity and high-temperature mechanical properties, and compatibility with the coolant, fuel and transmutation products [1-7]. In thermal nuclear reactors where the average energy of neutrons is ~ 25 meV, zirconium-based alloys are mainly used as the core structural components [8]. But in fast

reactors, where the average neutron energy is in a few MeV's, specially designed steels with high resistance against void swelling are used [9]. Radiation resistant steels are broadly classified into two categories; austenitic steels and ferritic steels. Austenitic stainless steels have face-centered cubic structure, contain 15-25% chromium and are non-magnetic. The fcc microstructure of the austenitic steel has been derived by the addition of nickel, manganese and nitrogen. Commonly used austenitic steels for nuclear applications are SS 316, SS 304, alloy D9, etc. [7, 9]. Ferritic steels possess body-centered cubic structure and are magnetic in nature. Ferritic steels containing 9-12% chromium is considered as a potential candidate for future reactor systems due to their excellent resistance against irradiation-induced swelling as compared to austenitic steels [3, 10-13]. Ferritic steels that are being used in reactor applications are Mod.9Cr-1Mo (T91 grade) steel, HT9 and Reduced Activation Ferritic/Martensitic (RAFM) steels such as EUROFER-97, CLAM steel, JLF-1 etc.

1.3. Fusion reactor program and the need for low activation structural materials

Energy production in a nuclear fusion reactor is due to the deuterium-tritium (D-T) fusion reaction:



The 14.1 MeV neutrons resulting from the D-T fusion reaction will have detrimental effects on core structural materials. These fusion neutrons induce severe displacement damage and radioactivity via nuclear transmutation in the core structural materials. For the successful realization of fusion reactors, a high-performance structural material which can withstand high displacement damage from fusion neutrons, stability against the void swelling and embrittlement due to transmutation gases, high tolerance to intense thermo-mechanical stresses and compatibility with high-temperature coolants is required. Other important international mandates, such as intrinsic safety and minimum long-term environmental impact put additional constraints on the selection of fusion reactor components [14]. The long-term environmental impact, due to the presence of long-lived radioisotopes induced by high energy neutrons put an additional burden of long term interim storage of radioactive waste and their safe disposal. Owing to the demand for high-performance structural materials with low induced-radioactivity, the fusion research community is left with a few options for the core-structural materials. Ferritic/Martensitic steels with well-optimized composition to attain the criteria of reduced activity, refractory alloys based on tungsten or vanadium and SiC/SiC ceramic composites are the prime candidates undergoing extensive studies to test

their compatibility with future fusion reactor systems [15, 16]. Another class of ferritic steels named Oxide Dispersion Strengthened (ODS) steel in which highly stable nano-scale oxide clusters are dispersed in the ferritic matrix has also been under consideration for future fusion reactor systems [12, 17].

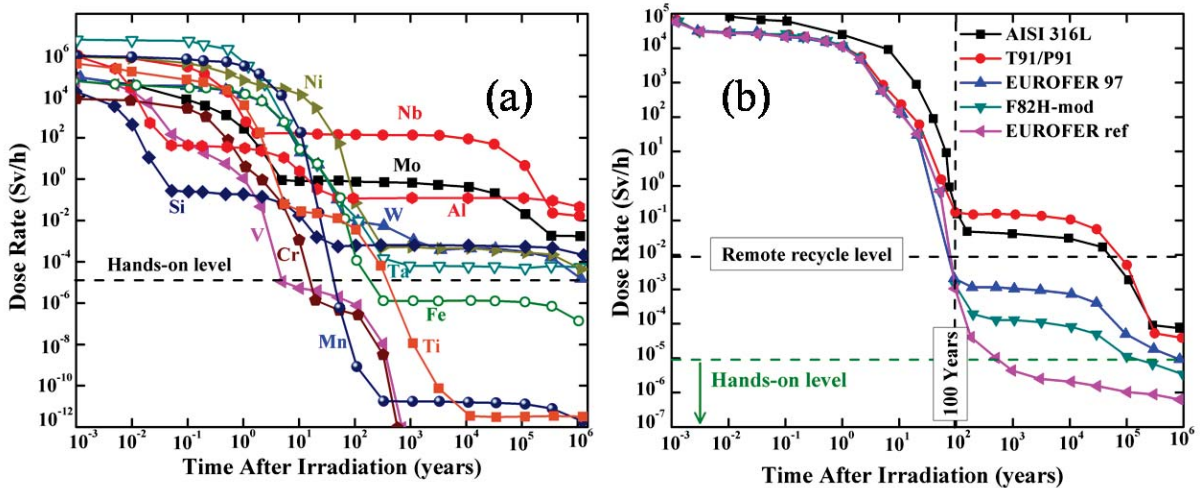


Figure 1.1 a) Specific dose rate vs. cooling time of twelve technologically important elements (reused with permission from ref [18], Copyright: Taylor and Francis (1990)) and b) variation of surface gamma dose rate with respect to cooling time for conventional austenitic steel (316L), ferritic steel (T91/P91) and different RAFM steels under fusion reactor first-wall demo conditions (reused with permission from ref [17], Copyright: Elsevier (2005)).

1.4. Reduced Activation Ferritic/Martensitic (RAFM) steel

Since the conventional steels contain elements that induce long-lived radioactive transmutation products, the prolonged radioactivity of these steels makes the post-irradiation handling and storage very difficult. Hence, long term interim storage is necessary for these materials before permanent disposal. This will have considerable environmental and cost implications. High amount of long-term induced-activity is mainly due to the presence of elements such as Mo, Nb, Ni, Cu, B, Co, N, Al etc. [19]. Neutron-induced transmutation reactions convert these elements into their long-lived radioisotopes. Figure 1.1(a) shows the variation of induced-activity measured in specific dose rate (Sv/h) as a function of cooling time or time after irradiation for some technologically important component elements of structural materials [18]. The dose rate was calculated for the fusion reactor first-wall demo-conditions. When the elements like V, Cr, Mn, Ti and Fe reaches the hands-on level radiation after 10^3 years of irradiation, other elements like Mo, Nb, Al etc. show a high amount of induced-activity even after 10^6 years [18]. To solve this issue, another class of Ferritic/Martensitic (FM) steels named Reduced Activation Ferritic/Martensitic (RAFM)

steels have been developed from conventional FM steels, by replacing the elements such as Mo and Nb that induce long-lived transmutation products by W and Ta, and strictly restricting other minor alloying elements such as Ni, Cu, Al, Co and B [17, 20]. Figure 1.1 (b) shows the induced-activity in steels under fusion reactor first-wall demo environment [17]. The conventional austenitic steel (AISI 316L) and ferritic steel (T91/P91) show high induced-radioactivity above the remote recycle level ($\sim 10^{-2}$ Sv/h) for 10^4 - 10^5 years after irradiation [17]. But in RAFM steels (EUROFER-97, F82H-mod, EUROFER-ref), proper tailoring of composition brings the induced-activity to remote recycle level within 100 years [17]. This reduces the risk associated with long-term interim storage and reprocessing of irradiated core-structural materials. RAFM steels have been developed in many countries as a structural material for the Test Blanket Module (TBM) in ITER, France. EUROFER-97 (Europe), CLAM steel (China), F82H and JLF-1 (Japan) and INRAFM (India) are a few examples [3, 21-23]. All the above RAFM steels are Fe-(9-12) wt% Cr based and contains 1-2 wt% W and 0.02-0.08 wt% Ta [24].

Table 1.1 Composition of Indian Reduced Activation Ferritic/Martensitic (INRAFM) steel used in this study [19].

| Elements | wt.% | Elements | wt.% |
|----------|--------|----------|---------|
| Cr | 9.03 | B | <0.0005 |
| W | 1.39 | Ti | <0.005 |
| Ta | 0.06 | Nb | <0.001 |
| V | 0.24 | Mo | <0.002 |
| C | 0.126 | Ni | 0.005 |
| Mn | 0.56 | Cu | 0.002 |
| N | 0.03 | Al | 0.0035 |
| O | 0.002 | Si | 0.06 |
| P | <0.002 | Co | 0.005 |
| S | <0.001 | As+Sn+Sb | <0.004 |

1.5. Indian Reduced Activation Ferritic/Martensitic (INRAFM) steel

Indian Reduced Activation Ferritic/Martensitic (INRAFM) steel has been developed as a core structural material for Indian Lead-Lithium Ceramic Breeder Test Blanket Module (LLCB-TBM) to be used in ITER [9, 19, 23, 25]. The complete composition of INRAFM steel used in this study is given in table 1.1 [19]. The elements that induce high radioactivity

(Mo, Nb, B, Cu, Ni, Al, Co, Ti) and the elements that promote embrittlement (S, P, As, Sb, Sn, Zr, O) are strictly controlled by careful selection of raw materials and stringent manufacturing methods [26]. The composition of W and Ta was optimized based on the desired performance of the material under mechanical testing such as tensile, impact, low-cycle fatigue, and creep [25]. More details on the optimization of composition were given in ref [19]. The steel ingots were fabricated in Mishra Dhatu Nigam (MIDHANI) Limited, India. Normalizing and tempering heat treatments were optimized at 1253 K for 30 minutes and 1033 K for 1 h. The heat treatment was optimized based on the variation of prior austenite grain size and hardness of the steel with temperature and time [12]. The normalization heat treatment at 1253 K ensures complete dissolution of $M_{23}C$ type carbide precipitates and the desired growth of austenitic grains [12]. The subsequent air cooling from 1253 K leads to the formation of martensite. The tempering treatment at 1033 K relieves the stress and improves the ductility of the steel. A more detailed study on the microstructure of INRAFM steel using electron microscopic techniques has been reported in the literature [12, 26-28]. The microstructural studies show that the tempered martensitic structure of INRAFM steel contains chromium and tungsten rich $M_{23}C_6$ precipitates on the lath and prior austenite grain boundaries, and fine tantalum and vanadium-rich MX-type precipitates on the dislocations inside the laths [12].

Indian LLCB-TBM has been developed with a prime objective of testing its capability to breed the tritium with a breeding ratio >1 , and the extraction of heat from tokamak with acceptable thermal efficiency [25]. A schematic of the major components of TBM is shown in figure 1.2 [25]. Indian LLCB-TBM consists of both solid and liquid breeder blanket assemblies. The solid ceramic breeder consists of lithium titanate in the form of packed pebble beds, and the liquid breeder consists of PbLi eutectic. The PbLi eutectic acts as both tritium breeder and coolant. INRAFM steel has been used as the structural material for the first-wall, which is being cooled by high-pressure helium gas. As shown in figure 1.2(a), the first-wall, top plate, bottom plate and the back plates are made up of INRAFM steel [25]. Figure 1.2(b) shows the cross-sectional view of the TBM [29]. A low-pressure helium purge circuit at 1.2 bar with 0.1% hydrogen is used to extract the tritium produced in the ceramic breeding zone [30].

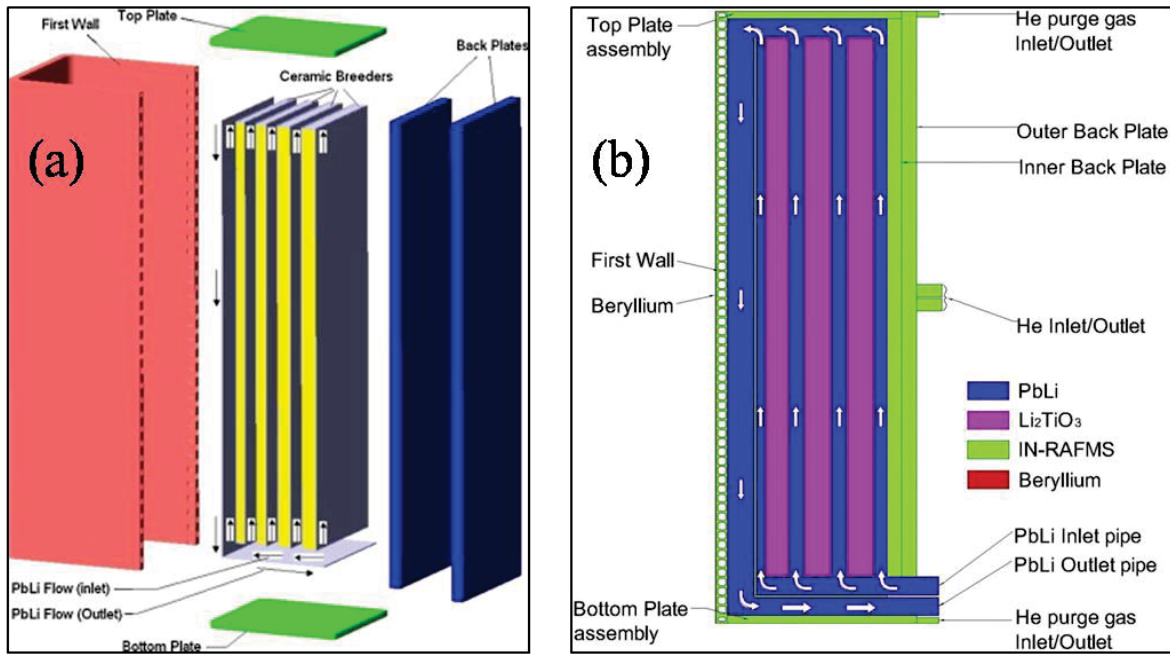


Figure 1.2 Schematic of the a) major components and b) cross-sectional view of Indian LLCB-TBM at ITER. The figures were adopted with permission from ref [25, 29] (Copyrights: Elsevier (2014)).

1.6. Irradiation effects in materials

High energy particles knock off the atoms from their lattice positions and produce vacancy-interstitial pairs or Frankel pairs as primary irradiation-induced defects. The atom displaced from its lattice site due to direct collision with the incident high energy particle is known as the primary knock-on atom (PKA). The energetic PKA atom collides with the surrounding atoms in the lattice and displaces some of them from their lattice positions. This process continues for all those atoms displaced from their lattice sites having energy greater than displacement threshold and ultimately end up in a “displacement cascade”. The extent of irradiation damage has been measured in displacement per atom (dpa), which is defined as the average number of times that an atom has been displaced from its lattice position for a given fluence of incident particles. Both vacancy and interstitial type defects are mobile at reactor operating temperatures, they can either recombine and eliminate each other or migrate towards sinks such as grain boundaries, dislocations, surfaces precipitate-matrix interfaces and get absorbed. Those point defects that survive from the sinks or recombination can agglomerate and form various types of higher-order defects such as clusters, voids, dislocations/dislocation loops, stacking faults etc. Typical time scales of the chain of events that happens during irradiation is given in Table 1.2 [31]. The irradiation damage events that start from the creation of PKA's to the formation of defect clusters happen within 10^{-11} s of irradiation. Thermal migration of point defects and defect-clusters that leads to their

recombination, additional clustering or dissolution, and trapping happens at a time scale greater than 10^{-8} s.

Table 1.2 Approximate time scale for the production of defects under irradiation in metals. This table is adopted from ref [31] with permission (Copyright: Springer Nature (2007)).

| Time (seconds) | Event | Result |
|-------------------|--------------------------------------------------------------|----------------------------------------------------------------------|
| 10^{-18} | Energy transfer from the incident particle | Creation of a primary knock-on atom (PKA) |
| 10^{-13} | Displacement of lattice atoms by PKA | Displacement cascade |
| 10^{-11} | Energy dissipation, spontaneous recombination and clustering | Stable Frenkel pairs and defect clusters |
| $>10^{-8}$ | Defect reactions by thermal migration | SIA and vacancy recombination, clustering, trapping, defect emission |

The core structural materials in nuclear reactors undergo degradation of their physical/chemical/mechanical properties due to neutron irradiation-induced microstructural changes. A schematic representation of different irradiation events that leads to the degradation of materials properties is shown in figure 1.3 [32]. The incident high energy radiations such as neutrons, electrons, gamma, fission products and ions lose their energy via atomic displacement cascades and electronic excitations. The defects such as PKA, point defects, gaseous and solid transmutation products produced during the primary radiation damage stage may cluster together during the displacement cascade or diffuse and segregate under the influence of temperature and stress. This clustering and segregation of defects lead to the formation of higher-order defects such as dislocation loops and networks (2-dimensional), voids, gas-filled bubbles and precipitates (3-dimensional). The microstructural changes introduced by the above defects influence the performance of the materials by altering thermal, physical, mechanical and chemical properties.

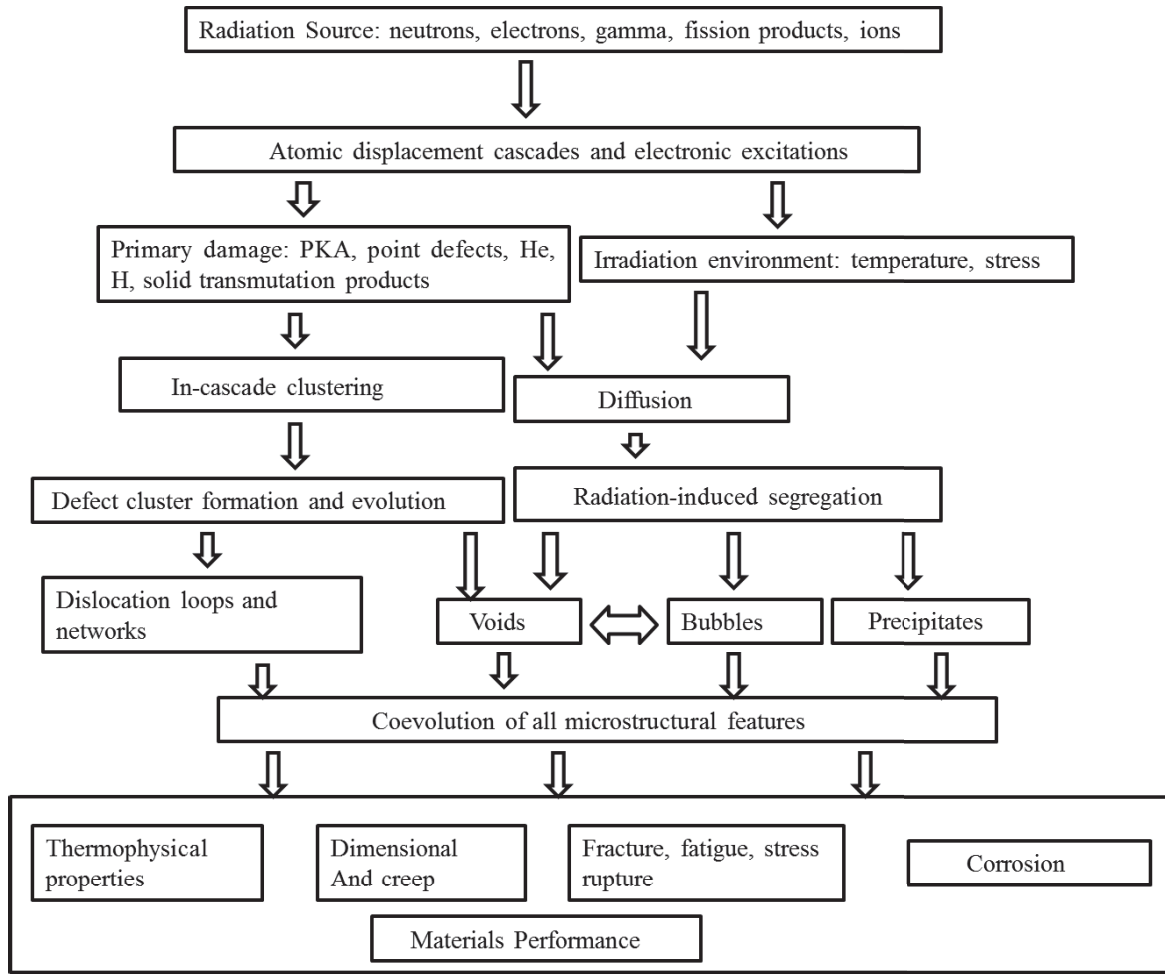


Figure 1.3 Schematic representation of various events caused by irradiation and their consequent effects on the performance of materials. This figure is reused with permission from ref [32] (Copyright: Elsevier (2017)).

The consequences of irradiation depend on the nature of the radiation, its energy, flux, fluence, irradiation temperature as well as on the microstructure of the material. Apart from the clustering of point defects that form higher-order defects, irradiation-induced segregation of alloying elements and impurities are also a major concern [33-37]. In addition to that, the interaction of point defects and their higher-order clusters with the alloying elements and impurities may change their energetics and kinetics. For example, the formation of carbon-vacancy complexes can influence the segregation of carbon, and the migration and clustering of vacancies [38]. Presence of vacancies even promotes the segregation of impurities or minor alloying elements such as Cr, Al, Si, P, S, Ga, Ge, Ni, Mn etc. in Fe based systems [36, 39]. Irradiation-induced segregation of alloying elements occurs at the sinks such as grain boundaries, dislocations, precipitate/matrix interfaces [34]. Irradiation-induced segregation or depletion of Cr from grain boundaries significantly changes the grain boundary chemistry, and that may expose the structural materials made up of steel to irradiation-assisted stress

corrosion cracking and enhanced inter-granular corrosion [33]. The enrichment of Cr, C, V, W, and Ti at the dislocation loops were observed in RAFM steel under irradiation in a mixed spectrum of spallation neutrons and high energy protons [35]. Formation and growth of voids and bubbles lead to volumetric swelling and hence the dimensional changes of in-core structural material and its premature failure [40-42]. The presence of transmutation gases such as helium can enhance the growth of voids by stabilizing the vacancies against vacancy-interstitial recombination. In thermal nuclear reactors, the main burn-up limiting factor is the fission-product poisoning whereas, in fast reactors, the loss of material ductility and its premature failure due to void swelling is the major burn-up limiting factor [9]. In fusion reactors, due to high neutron flux, the material failure due to irradiation damage is even faster as compared to fission reactor systems. Hence, as the world moves from fission to fusion reactor or Accelerator Driven Systems (ADS), suitable in-core as well as out-core materials have to be developed. It is essential to have thorough knowledge on the irradiation damage processes, the tolerance of materials to irradiation, the interaction of transmutation or fission/fusion reaction products with the materials and their effect on the material degradation in order to design and develop safer, reliable and efficient nuclear facilities.

1.7. Radiation damage models

The simplest estimation of the number of displacements produced by PKA is given by the Kinchin and Pease (K-P) model for atomic displacements. According to the K-P model, the number of atomic displacements $v(T)$ from a PKA atom of energy T is given by [31],

$$v(T) = \begin{cases} 0 & \text{for } T < E_D \\ 1 & \text{for } E_D < T < 2E_D \\ \frac{T}{2E_D} & \text{for } 2E_D < T < E_C \\ \frac{E_C}{2E_D} & \text{for } T \geq E_C \end{cases} \quad (1.2)$$

Where E_D is the displacement energy and E_C is the cut off energy for electronic energy loss. The K-P model assumes that the displacement damage occurs due to a sequence of binary collisions between atoms. When the kinetic energy (T) of PKA atom is less than the displacement energy (E_D), no atomic displacements will occur. The atoms get displaced from their lattice positions once $T>E_D$.

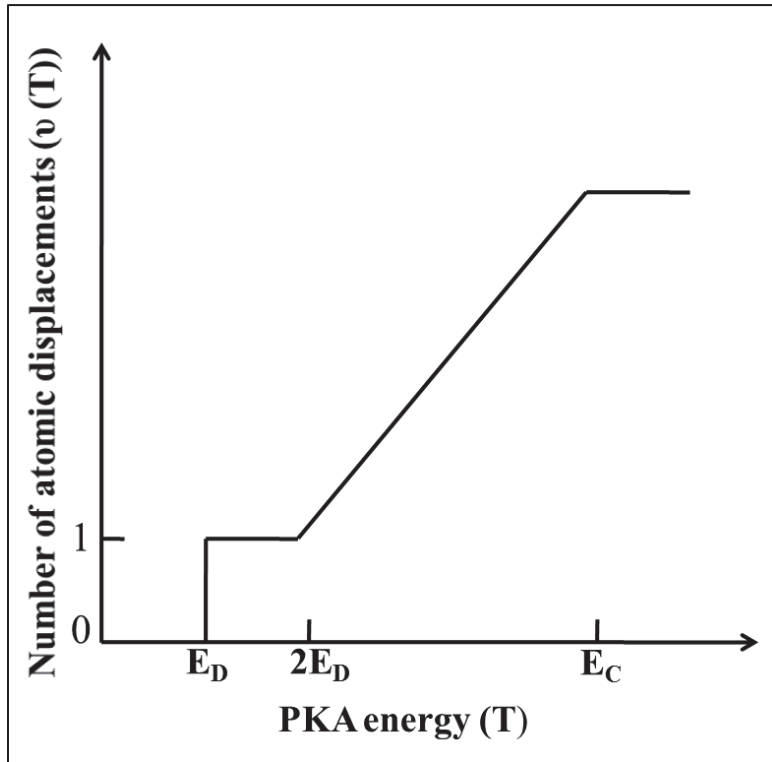


Figure 1.4 Variation of the number of displaced atoms as a function of PKA energy as predicted by the K-P model [31]. E_D is the displacement energy and E_C is the cut-off energy for electronic energy loss.

Figure 1.4 shows the number of atomic displacements in the cascade as a function of PKA energy according to K-P model. Energy loss by electronic interaction is given by the cut-off energy E_C . The atomic displacements increase linearly with the PKA energy in the range $T/2E_D < T < E_C$. The atomic displacements become independent of the PKA energy at $T \geq E_C$. If the PKA energy is greater than E_C , no additional atomic displacements occur until the electron energy losses reduce the PKA energy to E_C . However, the crystal lattice effects were not considered in the K-P model.

The K-P formula for atomic displacements was further modified by Norgett, Robinson and Torrens using the results obtained from the Binary Collision Approximation (BCA) simulations [43]. This modified formula is known as NRT formula or modified Kinchin-Pease formula and is given by [43],

$$v_{\text{NRT}}(T) = \begin{cases} 0 & \text{for } T < E_D \\ 1 & \text{for } E_D < T < \frac{2E_D}{0.8} \\ \frac{0.8T_d}{2E_D} & \text{for } \frac{2E_D}{0.8} < T < \infty \end{cases} \quad (1.3)$$

The factor 0.8 came from BCA simulation and is known as the displacement efficiency. The displacement efficiency is independent of the energy, target material and temperature. T_d is the damage energy, which is defined as the energy available to generate atomic displacements by elastic collisions.

1.8. Helium diffusion mechanisms in metals

Helium bubble nucleation and growth in materials is associated with the migration/diffusion of helium atoms followed by their segregation/accumulation at open-volume defects. An isolated He atom occupying a tetrahedral or octahedral interstitial position migrates faster due to its low migration energy of the order of 0.06-0.08 eV [44]. Helium atoms exhibit a strong attractive interaction with vacancies with a binding energy of ~ 1.5 eV and a weaker interaction with self-interstitial atoms (SIA) with a binding energy of ~0.3 eV [44, 45]. Due to its strong binding to He atoms, the presence of open-volume defects such as vacancies, dislocations and grain boundaries reduces the mobility of He atoms drastically. The dominant processes of helium trapping and migration depend on the temperature and the presence of intrinsic as well as irradiation-induced defects [46]. Since the presence of open-volume defects strongly influences the diffusion of helium in materials, the helium diffusion mechanisms can be basically divided under two categories, 1) helium diffusion at low radiation damage and 2) helium diffusion under normal irradiation conditions. The basic mechanisms involved in the migration of helium are illustrated in figure 1.5.

1.8.1. Helium diffusion at low radiation damage conditions

Helium diffusion at low radiation damage is basically divided into three categories [46], 1) interstitial migration, 2) vacancy migration and 3) impeded interstitial migration. In interstitial migration, He atoms occupying the interstitial positions migrate interstitially until they get trapped by any other defects. Since interstitial migration energy of helium is very low in metals, the interstitial migration is very fast even below the room temperature. This type of helium migration is dominant in situations where both the displacement damage and the concentration of thermal vacancies are less. At $T > 0.5T_m$, the concentration of thermal vacancies is very high and He atoms migrating through interstitial positions will be trapped by thermal vacancies. In this case, where $T > 0.5T_m$, the other two mechanisms - vacancy mechanism and impeded interstitial migration mechanism contribute to He migration. In the vacancy mechanism, a transient di-vacancy-He complex (HeV_2 complex) is formed and the He jumps from one vacancy to other. The migration energy of He atom associated with a

HeV_2 complex by vacancy mechanism is ~ 1.1 eV, whereas the dissociation energy of HeV_2 complex is ~ 1.45 eV in bcc-Fe [47]. Hence, HeV_2 complex is expected to migrate by vacancy mechanism. The impeded interstitial migration or He-vacancy dissociation mechanism is characterized by the dissociation of He from an already existing He-vacancy complex, migration through the interstitial positions and re-trapping by another vacancy.

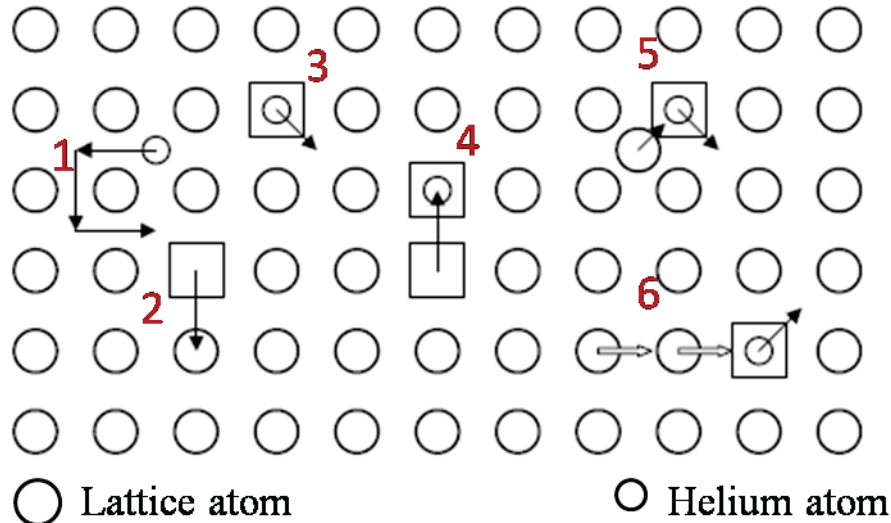


Figure 1.5 Schematic representation of helium diffusion mechanisms in materials. (1) Interstitial migration of helium, (2) migration of vacancy, (3) thermally activated dissociation of a substitutional helium atom from a vacancy to the interstitial position, (4) jumping of helium from one vacancy to another, (5) replacement of substitutional helium atom from a lattice site to interstitial by a SIA atom and (6) collisional displacement of helium atom. This figure is reused with permission from ref [46] (Copyright: Elsevier (2003)).

1.8.2. Helium diffusion under normal irradiation conditions

During irradiation, helium may be dissociated from a He-vacancy cluster by athermal mechanisms. The presence of irradiation-induced defects such as vacancies, self-interstitial atoms (SIA) and their clusters influence the diffusion of He under irradiation. Three He migration mechanisms that occur during irradiation are 1) displacement or cascade mixing mechanism, 2) replacement mechanism and 3) radiation enhanced vacancy mechanism. In displacement or cascade mixing mechanism, He migration/diffusion is due to direct displacements. This mechanism is dominant below the annealing stage III (at $T < 0.2T_m$) where vacancies are immobile. In replacement mechanism, He atom occupying vacancy is replaced by a SIA, the He atom then migrates interstitially and re-trapped by another vacancy. This mechanism is expected to be dominant between $0.2T_m$ and $0.5T_m$. At temperatures above $0.5T_m$, radiation enhanced vacancy mechanism dominates the

replacement mechanism. All three migration mechanisms are cooperative; the fastest mechanism is the dominant one.

During irradiation, He atoms can preferentially occupy irradiation-induced vacancy sites and form a He-vacancy (He-V) complex. In the initial stages of irradiation (incubation stage), in which the number of atomic defects dominates the defect clusters, the kinetic equilibrium yields [48],

$$\frac{C_{He}}{C_{HeV}} \approx \frac{D_{He} e^{-G_{HeV}^B/kT} + D_i C_i}{D_{He} C_V} \quad (1.4)$$

Where C_{He} , C_{HeV} , C_i and C_V are the atomic concentrations of interstitial He, substitutional He, self-interstitials and vacancies, D_{He} and D_i are the diffusion coefficients of He interstitials and self-interstitials respectively, and G_{HeV}^B is the binding free enthalpy of a He atom and vacancy. In the above equation, $C_{HeV} < C_V$ has been assumed.

At temperatures above annealing stage III ($T \sim 500$ K), where the vacancies are mobile, it can be assumed that [48],

$$N_z : F_z = \frac{C_0}{z} \quad (1.5)$$

Where N_z is the vacancy diffusion coefficient and C_0 is the thermal equilibrium vacancy concentration, and G_0 is the vacancy formation free enthalpy.

The vacancy concentration N_z is related to the production rate (λ) of Frenkel pairs by relation [48],

$$\lambda = v N_z k z F_z = C_0 \cdot E_{LC} z / 3 \quad (1.6)$$

Where r is the recombination radius and v is the atomic volume.

From the above equations, it follows that if $E_{LC} z \gg \lambda$ and $E_{LC} \gg z$ the substitutional He dominates the interstitial He in the temperature range for which these equations are valid.

The vacancy mechanism and dissociative mechanism are the preferential He diffusion mechanisms in the presence of vacancies. Under high-temperature irradiation conditions, where the dissociative mechanism is dominant, the effective He diffusion coefficient D_{eff} is given by [48],

$$D_{He}^{eff} = D_{He} \frac{C_{He}}{C_{HeV} + C_{He}} \approx D_{He} \frac{C_{He}}{C_{HeV}}$$
(1.7)

The effective He diffusion coefficient has been determined by considering three different temperature regions above stage III [48]:

1. At high temperatures where thermal vacancies dominate irradiation-induced vacancies ($T > 1030$ K), from equations 1.4 and 1.7 gives,

$$D_{He}^{eff} \approx D_{He} e^{-(G_{HeV}^B - G_V^F)/kT}$$
(1.8)

2. At medium temperatures, where irradiation-induced vacancies dominate thermal vacancies but the dissociation of He from vacancies is still governed by thermal activation ($850 \text{ K} < T < 1030 \text{ K}$),

$$D_{He}^{eff} = \left(\frac{4\pi r_F D_V}{\Omega P_F} \right)^{1/2} D_{He} e^{-\frac{G_{HeV}^B}{kT}}$$
(1.9)

Where $C_{HeV} < C_V$ has been assumed.

3. At low temperatures, where irradiation-induced vacancies are dominant, and the He dissociation from vacancies is governed by recombination ($500 \text{ K} < T < 850 \text{ K}$),

$$D_{He}^{eff} \approx D_V$$
(1.10)

1.9. Helium bubble nucleation and growth mechanisms upon irradiation

Helium bubbles formation in metals has been studied by two methods i) introducing helium into the material via irradiation or nuclear transmutation at elevated temperatures or ii) introducing helium at a lower temperature followed by post-irradiation annealing at elevated temperatures [46]. In the first case, apart from the helium production rate, the displacement damage rate and temperatures play a crucial role in bubble nucleation. In the second case, the bubble nucleation and growth depends on the accumulated helium content, the annealing temperature and the duration of annealing. The nucleation of the bubbles may happen during the implantation itself, whereas their growth can happen either during the helium implantation itself or during post-irradiation annealing treatment. A schematic representation of the time-dependent variation of various parameters characterizing helium bubble nucleation and growth during helium implantation and post-irradiation annealing is given in figure 1.6 [46].

1.9.1. Helium bubble nucleation during implantation

He bubble nucleation mechanism during implantation depends on the irradiation conditions such as displacement damage rate, total irradiation dose, He production rate, accumulated He concentration, irradiation temperature etc. He bubble nucleation can be either homogeneous or heterogeneous depending on the sink strength. Major He bubble nucleation mechanisms at various irradiation conditions are described below.

1.9.1.1. Irradiation at low displacement damage and low total implanted He concentration

During irradiation with helium ions or their introduction via nuclear transmutation reactions associated with displacement damage, bubble nucleation occurs within the material by simultaneous diffusion and clustering of vacancies and helium atoms. The dominating process of helium bubble nucleation during irradiation even depends on the ratio of helium production to displacement damage rates and irradiation temperatures. The variation of time-dependent concentration of helium atoms in the matrix (C), nucleation rate (dN_b/dt), density (N_b), and average size (r_b) of the nucleated bubbles during irradiation at high helium production to displacement rates are shown in figure 1.6. During irradiation or continuous generation of He, the bubble evolution can be divided into three stages [46, 48]:

- 1) Incubation stage: In the incubation stage, after a short transient, a quasi-static kinetic equilibrium is reached according to equations 1.4 to 1.6. During the incubation stage, C_i and C_v become constant, while C_{He} and N_b (or C_{HeV}) increase continuously but remains small enough such that the He clustering is nominal.
- 2) Nucleation stage: During the nucleation stage, with increasing C_{He} and dN_b/dt , helium clustering process increases, thereby, a rapid increase in N_b occurs. Newly nucleated embryos act as deep sinks for He. Hence, C_{He} and dN_b/dt reaches a maximum at $t=t_c$, and decreases with further increase in time. At t_c , the production and absorption rates of He atoms balance each other and hence, newly produced He atoms and already existing clusters are close to the kinetic equilibrium [46],

$$P_{He} \propto DC^c N_b^c \quad (1.11)$$

Where P_{He} is the He production rate.

- 3) Growth stage: The nucleation rate and the He concentration decreases after the nucleation stage. The growth stage is characterized by a strong reduction in nucleation

rate as compared to C_{He} . The growing bubbles absorb newly produced He atoms and hence, the size of the bubbles r_b increases but their density N_b saturates.

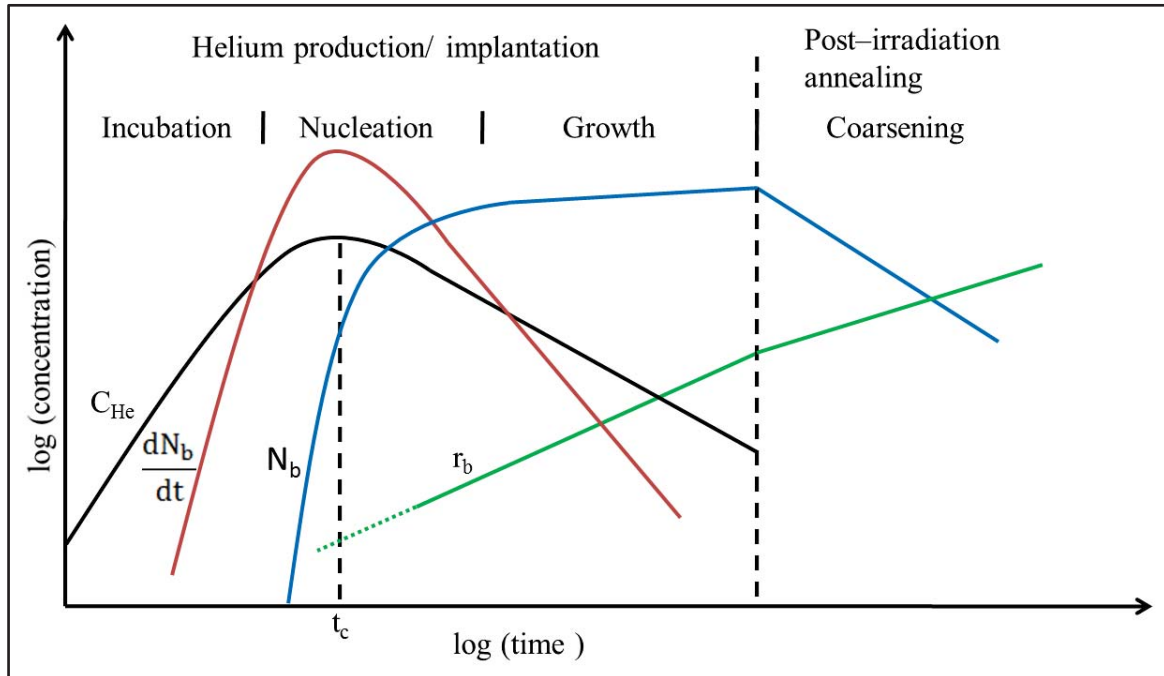


Figure 1.6 Schematic representation of the time-dependence of different quantities characterizing bubble nucleation during helium production/implantation and bubble coarsening during annealing. Here, C_{He} is the time-dependent concentration of helium atoms in the material, dN_b/dt is the nucleation rate, N_b is the density and r_b is the average size of the nucleated bubbles. Logarithmic representation is used to approximate the power-law behaviour of some individual curves to straight lines [46]. This figure is reused with permission from ref [46] (Copyright: Elsevier (2003)).

Trinkaus [48] estimated the density of bubbles by considering two extreme cases for temperature T and He production rate P_{He} ,

- 1) Low T, high P_{He} : Homogeneous nucleation with spontaneous He precipitation without a thermodynamic barrier can occur during this regime. Since temperature is low, even small He-vacancy clusters are stable and grow. By considering the nucleation via diatomic nuclei consisting of two He atoms, an approximate value of N_b is given by,

$$N_b \approx 5 \left(\frac{P_{He}}{4\pi r_b D_{He} \Omega} \right)^{1/2} \quad (1.12)$$

- 2) High T, low P_{He} : Heterogeneous nucleation controlled by a thermodynamic barrier which depends strongly upon He concentration and nucleation site. A critical He

concentration C_{He}^{Cr} and He-vacancy clusters having a critical size are required for the nucleation; smaller He-vacancy clusters are unstable and decay, the larger ones grow. In this case, N_b is given by,

$$N_b \approx \frac{P_{He}}{2\pi r_b C_{He}^{Cr} D_{He}^{\text{eff}}} \quad (1.13)$$

Since the nucleation occurs via the dissociation of nuclei having a size below a critical size, the high temperature He bubble nucleation process is He re-solution or dissociation controlled.

1.9.1.2. Irradiation at high displacement damage and high implanted He concentration

When a high amount of He is introduced into materials associated with high displacement damage, He atoms are resolved from already nucleated small bubbles by displacement cascade and results in the secondary nucleation of bubbles. At higher doses, a linear increase in bubble density with dose at constant bubble size between the temperature ranges $0.2T_m < T < 0.5T_m$ given by [46],

$$N_b \propto \left(\frac{P_{He}}{D}\right)^{3/7} \left(\frac{P_{He}}{kK}\right)^{1/7} kKt \quad (1.14)$$

And the bubble size R is given by [46],

$$R \propto \left(\frac{DP}{k^2 K^2}\right)^{1/7} \quad (1.15)$$

Where k is the resolution parameter, K is the displacement rate. Below $0.2T_m$, He diffuses by the displacement mechanism, primary and secondary nucleation becomes indistinguishable and the size of the bubble nuclei does not exceed the size of atomic scale. As the irradiation temperature increases above $0.5T_m$, the displacement damage induced resolution of He atoms becomes inefficient since the He atoms resolved from smaller bubbles are re-absorbed by the bubbles of increasing size. At this high temperature, dissociation of He atoms from the bubble nuclei is the dominant mechanism.

1.9.1.3. Homogeneous and heterogeneous nucleation of bubbles

Helium bubble nucleation in materials can happen either via homogenous or heterogeneous nucleation [46]. The homogeneous nucleation occurs within a perfect crystal lattice due to the diffusion and clustering of helium atoms and vacancies. On the other hand, the crystalline defects or inhomogeneities in the matrix such as dislocations, grain boundaries

and precipitate-matrix interfaces can trap mobile helium atoms and act as potential sites for heterogeneous bubble nucleation. The irradiation or post-irradiation annealing temperature plays a major role in deciding the dominant nucleation mechanism. At low temperatures, thermal dissociation of helium atoms from the traps is negligible, and the dominant nucleation mode is determined by the relation between the partial sink strengths of the already grown bubble nuclei according to homogeneous nucleation and of pre-existing deep traps. Homogenous nucleation will be dominant if the sink strength of an already existing bubble nucleus is larger than the sink strength of other pre-existing traps. The sink strength of any trap is given by the product of the size and concentration of that particular trap-type. If the sink strength of pre-existing traps dominates than that of bubble nuclei, for the given pre-existing sink parameters, homogenous nucleation will be dominant at low temperature and/or high He production rates, and vice versa. But at high temperatures, the relation between partial sink strengths of possible nucleation sites does not provide a sufficient criterion for homogenous vs. heterogeneous nucleation since thermal dissociation of He atoms from the traps also must be accounted. Here, the effects of dislocation cores, interfaces and grain boundaries on the thermodynamics of critical bubble nuclei are important. By assuming that the bubble nucleation occurs at a certain minimum critical nucleus size, a classical model suggested by Trinkaus et al. [46] showed that the heterogeneous bubble nucleation at the interfaces and grain boundaries would occur at a lower critical He concentration than homogenous nucleation.

1.9.2. He bubble coarsening mechanisms up on post-irradiation annealing

When the material already implanted with He at some elevated temperature and brought back to room temperature, and further annealed at a higher temperature, He bubbles that are already nucleated during implantation tend to coarsen. The post-irradiation annealing at constant He content increases the size of the bubbles but reduce their density. Two major mechanisms that govern the bubble coarsening during annealing are 1) bubble migration and coalescence (MC) and 2) Ostwald ripening (OR) [46]. The dominant mechanism among the above two is determined by the concentration of implanted He (C_{He}), annealing temperature (T) and annealing time (t).

In bubble migration and coalescence, the bubble migration is due to the random rearrangements of bubble surface by diffusion of matrix atoms. The bubble migration is surface diffusion-controlled, and the total volume of the bubble population is conserved. The number density of bubbles changes with annealing time t is given by [49],

$$N_b \approx 0.1\Omega^{-7/6} \left(\frac{v_{He} C_{He}}{D_s t} \right)^{1/2} \quad (1.16)$$

Where Ω and v_{He} are the atomic volumes of metal and He, D_s is the surface self-diffusion coefficient.

In Ostwald ripening mechanism, He atoms are thermally dissociated from smaller bubbles and re-absorbed by larger bubbles. Ostwald ripening of He bubbles occurs by the dissociation and re-absorption of He atoms as well as vacancies. Hence, the Ostwald ripening process may be He atom or vacancy dissociation controlled and depends on which of the dissociation energy is smaller. As the internal pressure of the bubble increases, the vacancy dissociation from the bubble becomes difficult as compared to the He dissociation [50]. For He-dissociation controlled Ostwald ripening where the total volume is conserved, the bubble concentration is given by [49],

$$N_b \approx \frac{kT C_{He}}{4\gamma v_{He} D_{He} C'_{He} t e^{(\mu_{He}/kT)}} \quad (1.17)$$

Where γ is the surface free energy, D_{He} is the He diffusivity in the matrix, C'_{He} is the He concentration in the solution for the He density at which the He chemical potential μ_{He} vanishes and $C'_{He} e^{(\mu_{He}/kT)}$ is the actual He concentration in the matrix.

1.9.3. Equilibrium pressure and mechanical stability limit of bubbles

The pressure or density of the bubble depends on the conditions at its evolution stage such as temperature, He production and displacement rates, accumulated He concentration and irradiation dose and the bubble size. The pressure inside the bubble can be estimated by considering two limiting cases given by [46],

- 1) The mechanical stability limit at which the yielding of the matrix occurs by spontaneous plastic deformation. The upper bound limit of the pressure for mechanical stability limit is given by,

$$\frac{Q}{r t J} \quad (1.18)$$

Where μ is the shear modulus of the matrix. This pressure limit holds good at higher He/dpa ratio where He dominates the bubble evolution since the vacancies and self-interstitial atoms annihilate at the existing bubbles.

- 2) Thermodynamic equilibrium condition is given by,

$$P = \frac{2\gamma}{r} \quad (1.19)$$

Where γ is the surface free energy. This condition holds good around and above the stage-V ($T > 0.4T_m$) where the thermal equilibrium vacancy concentration is sufficient to establish thermal equilibrium of bubbles.

1.10. Hydrogen trapping in materials

The interaction of hydrogen with lattice imperfections is a serious concern since it leads to the failure of materials via hydrogen-embrittlement and corrosion. Lattice imperfections such as vacancies and their clusters, voids, dislocations, solute atoms, grain boundaries, precipitates, inclusions and particle-matrix interfaces act as traps for hydrogen atoms and hence, lead to the accumulation of hydrogen in materials [51, 52]. In metals, vacancies are the strongest traps for hydrogen with a binding energy of around 0.5 eV [51, 53]. In a defect-free α -Fe lattice, hydrogen prefers to occupy a tetrahedral site over an octahedral site [51, 53]. Theoretical calculations show higher formation energy of ~ 2.61 eV for substitutional hydrogen atoms in the α -Fe lattice as compared to both the tetrahedral (~ 0.21 eV) and octahedral (~ 0.34 eV) positions [51]. Hence, the substitutional site is an unstable position for hydrogen atoms. Hayward et al. [53] reported that when trapped in vacancies, hydrogen prefers octahedral sites over the tetrahedral or the substitutional site. It has been reported by several groups that the trapping of hydrogen in vacancies occurs such a way that hydrogen will occupy a position that is slightly off centred (0.2 - 0.5 Å) from the octahedral site towards the vacancy [51, 54-56]. It has also been reported that up to six hydrogen atoms can be trapped at a monovacancy, and the binding energy of hydrogen-vacancy complexes decreases with increase in number of hydrogen atoms [53]. The solute elements such as Y, Sc, Mg and Cd trap hydrogen atoms with binding energy larger than 0.10 eV [51]. Among the common alloying elements in steel, elements such as C, Ti and Nb trap hydrogen with a binding energy of around 0.1 eV, whereas the elements such as Cr, Mo, Mn, Si do not bind hydrogen [51]. The interaction of hydrogen and its isotopes with helium associated defects is also relevant from the fusion reactor point of view. In α -Fe, three different types of traps are observed for deuterium with binding enthalpies 0.46 eV, 0.81 eV and 0.75 eV corresponding to the monovacancies, small vacancy clusters and small helium bubbles [55, 57]. Similar trapping sites were also observed in Ni implanted with deuterium and helium [58, 59]. The exact mechanism of migration of hydrogen-vacancy complexes and their agglomeration to hydrogen bubbles is still lacking clarity. It has been reported that the

dissociation barrier of a hydrogen-vacancy pair that contain only one hydrogen atom and vacancy is around 0.64 eV whereas, its migration barrier is around 0.76 eV [53]. Hence, it cannot migrate as a pair; instead, it dissociates and migrates separately. A low migration barrier of ~0.25 eV is reported for higher-order complexes of the type H_mV_3 [53]. This shows that H_mV_3 complexes can migrate as a single unit without dissociation.

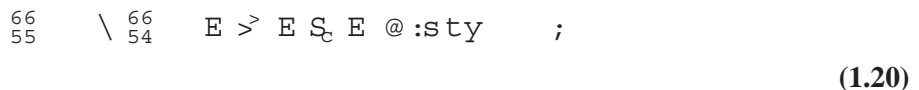
1.11. Experimental investigation of irradiation-induced microstructural changes

Study of defects induced by hydrogen and helium irradiation and their influence on microstructure of materials have been carried out using experimental techniques such as Transmission Electron Microscopy (TEM) [59-62], Thermal Desorption Spectroscopy (TDS) [63-65], ion-beam analysis [52, 66, 67], Scanning Electron Microscopy (SEM) [68, 69], Grazing-Incidence Small-Angle X-ray scattering (GISAXS) [70], Scanning Transmission Electron Microscope-based Electron Energy Loss Spectroscopy (STEM-EELS) [71, 72], and Positron Annihilation Spectroscopy (PAS) [73-76]. Valuable information on the nature, size, location and distribution of irradiation-induced defects such as voids, bubbles and dislocations has been provided by TEM [60, 77, 78]. Migration of helium bubbles along the grain boundary dislocations has been observed in helium implanted Fe9Cr alloys using an *in situ* TEM [79]. An enhanced swelling due to synergistic effect of displacement damage, hydrogen and helium ions have been reported in RAFM steels using TEM [80]. Radiation-induced amorphization of $M_{23}C_6$ precipitates and Laves phase and re-solution of TaC precipitates are also reported in RAFM steels using TEM [81]. Knowledge of various hydrogen and helium traps present in materials along with their binding energies has been obtained by using TDS studies [63, 64]. Techniques such as Secondary Ion Mass Spectrometry (SIMS) and Nuclear Reaction Analysis (NRA) have been used to study the depth distribution of implanted hydrogen or helium in materials, and variation of the implanted profile due to thermal migration or desorption [67, 82]. Strong trapping of hydrogen isotopes in helium associated defects has been reported in an *in situ* NRA study [66]. Non-destructive determination of size and depth distribution of helium nano-bubbles with high statistical precision has been performed using GISAXS [70]. In STEM-EELS, the measurement of energy shift of 1s-2p transition of helium enables to quantify the atomic density and pressure of helium associated with the bubbles [71]. Irradiation-induced changes in surface morphologies such as blistering and exfoliation have been studied using SEM [68, 69]. Other surface-sensitive techniques such as GIXRD and Nanoindentation have also been used to study the irradiation-induced microstructural changes in the near-surface region of

materials [83, 84]. Radiation-induced segregation of alloying elements at surfaces and grain boundaries, and their consequent depletion from the matrix is studied using techniques such as Atom Probe Tomography (APT), Auger Electron Spectroscopy (AES), Scanning Transmission Electron Microscopy equipped with Energy Dispersive x-ray Spectrometry (STEM-EDS) [33, 85, 86] etc.

1.12. Positron Annihilation Spectroscopy (PAS)

Positron Annihilation Spectroscopy (PAS) is a versatile and highly sensitive non-destructive technique for defect studies in materials. The uniqueness of electron-positron annihilation makes PAS a highly sensitive technique to probe open-volume defects with resolvable size from mono-vacancies to nano-voids, with concentration down to a few ppm. Positrons are sensitive to open volume defects such as vacancies, vacancy clusters, voids, dislocations, grain boundaries, precipitate-matrix interfaces etc. In conventional PAS techniques, positrons are generated from the spontaneous β^+ -decay of some radioactive isotopes (^{22}Na , ^{64}Cu , ^{58}Co , etc.). Among the radioactive positron sources, ^{22}Na is widely used because of its longer half lifetime ($T_{1/2} \sim 2.6$ years), high positron yield (90.4%) and the availability of prompt γ -ray for lifetime measurements. Radioactive decay reaction of ^{22}Na isotope is given by,



Positrons are emitted from the ^{22}Na source due to spontaneous β^+ -decay. The prompt γ -ray having energy of 1.27 MeV is emitted simultaneously along with the positron. $\bar{\nu}_e$ is the electron-neutrino emitted during the radioactive decay.

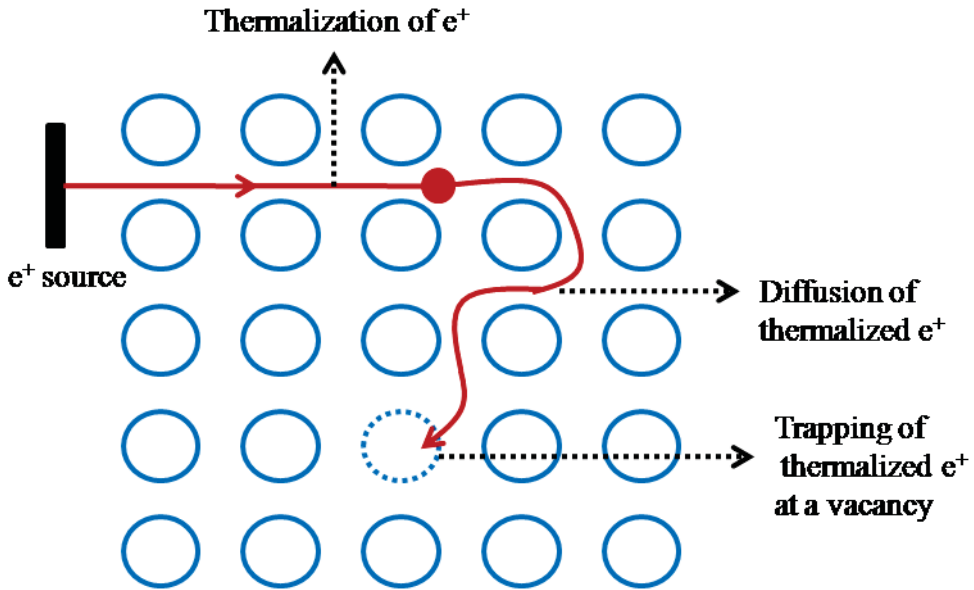


Figure 1.7 Schematic representation of thermalization and diffusion of positrons in solids followed by trapping at a vacancy site.

Fig 1.7 shows typical interactions of positrons in a solid [87]. High energy positrons implanted into the material thermalize within 10^{-12} s, and then start diffusing in the lattice. Since positrons experience repulsion from positively charged nuclei of the atoms, they get trapped at a vacancy during diffusion. The diffusion length of thermalized positrons is ~ 100 nm in metals and alloys. Positron trapped at the vacancy will annihilate with an electron from the nearby atom, and this results in the emission of two 511 keV annihilation gamma photons. There are three major PAS techniques, Positron Annihilation Lifetime Spectroscopy (PALS), Doppler Broadening (DB) and Angular Correlation of Annihilation Radiation (ACAR) spectroscopy [87]. Basic principles of the techniques are illustrated in figure 1.8.

Positron Annihilation Lifetime Spectroscopy (PALS)

The time difference measured between the prompt 1.27 MeV γ -photon and one of the 511 keV annihilation photons gives positron lifetime (τ). Positron lifetime depends upon the local electron density at the annihilation site. The positron annihilation rate (λ), the reciprocal of positron annihilation lifetime is given by [87],

$$\lambda = \frac{1}{\tau} = \pi r_0^2 c \int n_+(r) n_-(r) \gamma_c dr \quad (1.21)$$

Where $n_+(r)$ and $n_-(r)$ are the positron and electron densities, r_0 is the classical electron radius, c is the speed of light and r is the position vector, γ_c is the correlation function that describes the increase in electron density due to the Coulomb attraction between a positron and an electron. As the local electron density at the site of annihilation decreases, the positron

lifetime increases and vice versa. The reduced electron density at the open-volume defects such as vacancies and their agglomerates increases the positron lifetime as compared to the defect-free state. PALS is a quantitative analysis technique, where the positron lifetime depends on the size of the open-volume defect, and its intensity is proportional to their relative concentration.

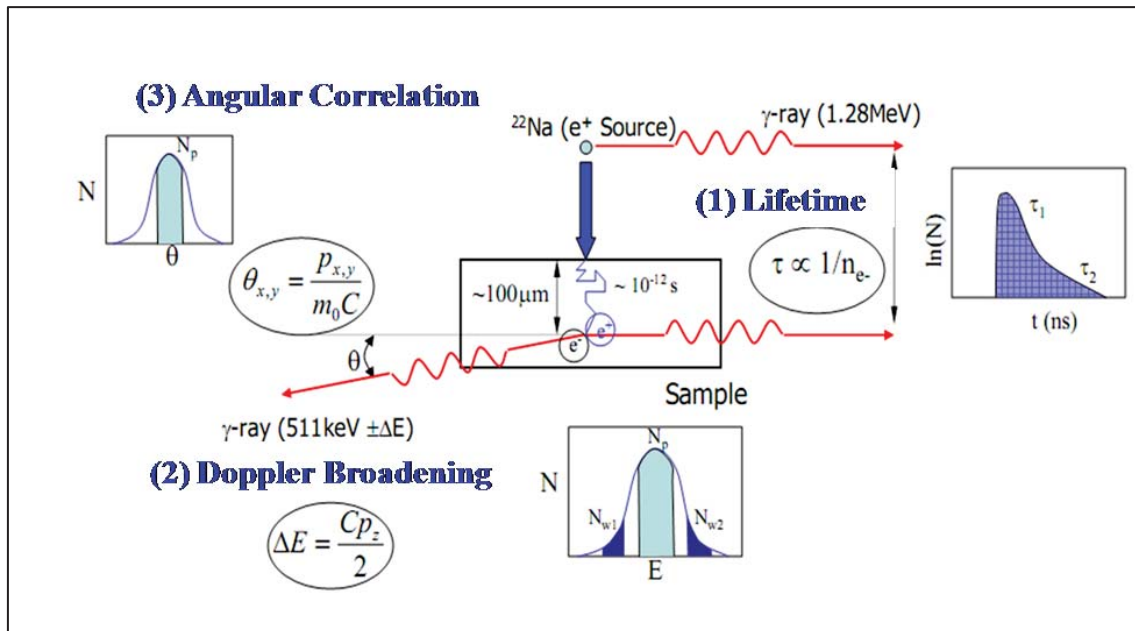


Figure 1.8 Schematic of major positron annihilation spectroscopic techniques.

When positrons are implanted into a sample containing k different defect types, the time-dependent decay spectrum $D(t)$ of positrons in the sample is given by,

$$D(t) = \sum_{i=1}^{k+1} I_i e^{-t/\tau_i} \quad (1.22)$$

Where k different types of defects contribute $k+1$ components in the PALS spectra with individual lifetimes τ_i and intensities I_i . For a defect-free material, where there are no positron traps present, the above equation will reduce to,

$$D(t) = e^{-t/\tau_b} \quad (1.23)$$

Where τ_b is the positron lifetime in the defect-free bulk of the sample. The positron lifetime spectrum $N(t)$ is the absolute value of time derivative of the positron decay spectrum $D(t)$ given by,

$$N(t) = \sum_{g=5}^{i>5} \frac{I_g}{R_g} \cdot e^{-\frac{t}{\tau_g}}$$
(1.24)

Doppler Broadening Spectroscopy (DBS)

In laboratory frame of reference, the momentum component of electron-positron pair in the direction of propagation of annihilation γ -rays introduces Doppler broadening to the photon energy. Since the positron reaches thermal energies before annihilation, the major contribution to Doppler broadening comes only from the electrons. Due to this broadening, the energy of annihilation photons will be $511 \pm \Delta E$ eV. This broadening is measured using energy dispersive detectors such as High Purity Germanium (HPGe) detectors. The shift (ΔE) in the energy is given by [87],

$$\Delta E = c \cdot L \cdot \frac{x}{t}$$
(1.25)

Where x is the component of electron momentum along the direction of propagation of annihilation γ -ray and c is the velocity of light. From the Doppler-broadened annihilation spectra, two line-shape parameters, namely shape (S-parameter) and the wing (W-parameter) parameters, are deduced.

The regions under the spectrum using which the line-shape parameters have been defined are shown in figure 1.8. The S-parameter is defined as the ratio of counts under the central low-momentum part of the spectrum (N_p) to the total counts under the whole spectrum (N_{total}) after background subtraction.

$$S = \frac{N_p}{N_{total}}$$
(1.26)

Similarly, the W-parameter has been defined as the ratio of counts under the wing regions (N_{w1} and N_{w2}) to the total counts under the whole spectrum (N_{total}) after background subtraction.

$$W = \frac{N_{w1} + N_{w2}}{N_{total}}$$
(1.27)

Positrons may annihilate with either valence or core electrons. Since the momentum of valence electrons is less than the core electrons, the broadening of 511 keV γ -lines will be less if the positrons annihilate with valence electrons and vice versa. Hence, the contribution to the S-parameter comes from the valence electrons, and hence, it is also called valence-

annihilation parameter. On the other hand, since the contribution to W-parameter comes from the high momentum core electrons, it is called core-annihilation parameter. The presence of open-volume type defects increases the fraction of positrons annihilating with valence electrons. Consequently, the S-parameter increases with an increase in number or size of the open volume defects as compared to a defect-free sample. Since the core electrons are the identity of the elements, any change in the chemical environment of the annihilation site will reflect in the W-parameter.

Angular Correlation of Annihilation Radiation (ACAR)

Due to the electronic momentum component $p_{x,y}$ perpendicular to their direction of propagation, the annihilation γ -rays deviate from their collinearity. This angular shift $\theta_{x,y}$, is related to the perpendicular momentum component $p_{x,y}$ by the relation [87],

$$\theta_{x,y} = \frac{p_{x,y}}{m_0 c} \quad (1.28)$$

Where m_0 is the rest mass of the electron. In ACAR measurements, $\theta_{x,y}$ is measured simultaneously in both x and y directions by coincidence measurements using position-sensitive γ -detectors. ACAR is mainly used to carry out electronic structure investigations. Like DBS, when positrons annihilate with the valence electrons, the angular deviations will be smaller and vice versa for core electron annihilation. The availability of Anger cameras has enabled the ease of measurement of two-dimensional angular correlation spectra.

1.13. Study of irradiation effects in materials using PAS

Positron annihilation spectroscopy has been widely used to carry out irradiation damage studies in metals [38, 74, 88-90], alloys [91-95], semiconductors [96-101], glasses [102-106] and polymers [107-113]. While the conventional positron annihilation techniques provide information from the first few hundreds of microns from the surface, positron beam-based techniques enable depth-profiling of irradiation-induced defects from the surface to a few hundred nanometers. PAS techniques have been widely used to study the irradiation-induced microstructural changes in nuclear structural materials. Positron beam technique can be coupled to the irradiation chamber of an accelerator to carry out *in situ* monitoring of defect evolution during irradiation or to study the defect configurations immediately after irradiation under controlled temperature and atmosphere [114-116].

Formation and agglomeration of irradiation-induced vacancy-type defects, the effect of impurities such as carbon to stabilize those defects and various annealing stages in metals

have been systematically studied using PAS [38]. Nature of the defects and the possible defect annealing mechanisms during different stages of annealing in neutron-irradiated metals has been studied using PAS [117, 118]. A brief review of PAS studies on the accumulation of point defects and their complexes in irradiated metals has been given by Eldrup [119]. Complimentary nature of PAS and resistivity measurements have been efficiently utilized to study various defect-annealing mechanisms in metals by irradiating at low temperatures where vacancies are immobile, followed by high-temperature annealing [120]. Trapping of hydrogen by vacancies in Cu with a binding energy of ~0.4 eV and its de-trapping above 450 K has been reported using PAS [121]. It has been reported that the inherent inhomogeneities play a major role as compared to the irradiation-induced defects in the positron-annihilation characteristics of amorphous metals [122]. Trapping of positrons in He bubbles in metals such as Al [123], Ni [74], Cu [73], Pa [75], Fe [124], Mo [125], Nb [126], Cr [127] have been also studied extensively.

Irradiation-induced microstructural changes introduced in reactor core-structural materials due to neutron irradiation at elevated core temperatures, gases and impurities produced by nuclear transmutation reactions etc. have been studied extensively using PAS techniques. PAS has contributed significantly to the microstructural evaluation of Reactor Pressure Vessel (RPV) steels [128-133]. In RPV steels, defects introduced by neutron irradiation leads to embrittlement and premature failure of the vessel. The role of irradiation-induced precipitates, solute nano-clusters, vacancy clusters, voids and dislocation loops in hardening the RPV steels have been studied using PAS [130-132]. PAS is sensitive to irradiation-induced precipitates such as carbides, nitrides and Cu precipitates in RPV steels [133]. A PAS study showed the formation of irradiation-induced carbide precipitates in Cr-Mo-V-type RPV steels of VVER-type reactors, which may strengthen the matrix and leads to embrittlement [130]. Trapping of positrons in Cu-rich precipitates and Cu-vacancy complexes that causes irradiation-induced hardening in RPV steels containing Cu have been reported [129, 132]. Apart from Cu precipitation, PAS studies showed that in Cu free or low-Cu RPV steels, precipitation of alloying elements such as Mn and Ni at high irradiation doses lead to hardening [129].

Since FeCr alloy is a model alloy system for the steels, extensive irradiation damage studies have been carried out using PAS to understand the irradiation damage mechanism in binary FeCr system. Trapping of positrons in vacancies, vacancy clusters, dislocations, vacancies trapped by dislocations, vacancy-impurity complexes and precipitates have been observed in irradiated FeCr systems [134]. The influence of Cr in reducing the number of

surviving vacancies induced by neutron irradiation in FeCr alloys has been reported using PAS [135]. In addition to Cr, metal-carbides also play a crucial role in reducing the vacancy concentration and hence, to lower void swelling in FeCr alloys as revealed by another PAS study [136].

The advent of positron beam techniques enabled non-destructive depth profiling of open-volume defects in materials. Since ion-irradiation induces inhomogeneous distribution of defects, depth profiling provides information about various damaged layers present in near-surface regions of the material. Irradiation-induced microstructural changes in steels and their model alloys have been studied at fission, fusion or spallation relevant irradiation conditions using positron beam techniques [40, 91, 137, 138]. Variable Low-Energy Positron Beam (VLEPB) based Doppler broadening spectroscopy has been used as an efficient technique to address the void swelling in reactor steels [40, 41]. The depth distribution of helium-vacancy complexes and the evolution of helium bubbles with temperature and irradiation dose also have been investigated using positron beam technique [139-141]. The depth profiling measurements using positron beam identifies different regions in the irradiated materials such as 1) surface region, 2) track region where ions slow down mainly by electronic energy loss, 3) Bragg peak region where the incident ions interact with the lattice atoms via nuclear collisions and finally stop within the lattice, and 4) the non-implanted region in according to the distribution of defects [139].

1.14. Motivation for present work

Low-activation materials with desirable high-temperature mechanical properties and good resistance against irradiation damage are one of the prime requirements of fusion reactor first-wall materials. As compared to other low-activation materials, the matured fabrication technologies and availability of literature data make RAFM steels a most promising candidate for DEMO fusion power plants. Unavailability of high flux neutron irradiation facilities makes ion beam irradiation as an efficient tool to simulate the neutron-induced damage of fusion first-wall materials with well-controlled irradiation conditions. Due to their strong trapping at vacancy-type defects, positrons have been widely used to probe irradiation-induced microstructural changes in these materials.

Neutron irradiation introduces large amount of hydrogen and helium associated with high displacement damage into the first-wall material of fusion reactors. Hydrogen and helium are having detrimental effects on the first-wall structural materials. Low migration energy of hydrogen and helium enable their rapid migration and trapping at vacancies or

vacancy clusters thereby stabilizing them against vacancy-interstitial recombination. Trapping of helium at vacancy-type defects lead to the formation of helium bubbles, which further leads to void swelling, loss of ductility and premature failure of the first-wall material. Even though the role of hydrogen in cavity/void formation is low, the synergistic effect of hydrogen and helium is significant in first-wall materials. Interaction of hydrogen with helium-vacancy complexes and its influence in promoting helium bubble growth is still not well understood. Aim of this thesis work is to study the irradiation effects in INRAFM steel by simulating irradiation conditions that resemble fusion first-wall using ion beams. Study of defects and defect-complexes induced by helium and hydrogen ion irradiation and their thermal evolution is one of the major focuses of the thesis. Investigation of thermal stability of vacancy-type defects in INRAFM steel and the influence of helium at fusion relevant He/dpa ratio in stabilizing the vacancy-type defects is another important intention of this thesis.

Chapter 2

Experimental Methods

2.1. Introduction

This chapter discusses the irradiation procedures and characterization techniques that are used to study the irradiation-induced changes in INRAFM steel. Helium and hydrogen irradiations were carried out using 150 keV gaseous ion implanter, whereas the Fe ion irradiation was performed using a 1.7 MV tandemron accelerator at Materials Science Group, IGCAR, Kalpakkam. Depth profiling of irradiation-induced defects was carried out using positron annihilation Doppler broadening measurements based on a variable low-energy positron beam. Helium depth profiling was carried out using Secondary Ion Mass Spectrometry (SIMS), and the helium bubble size was measured using Transmission Electron Microscopy (TEM). Irradiation-induced changes in the nano-hardness and micro-strain were studied using Nanoindentation and Grazing Incidence X-ray Diffraction (GIXRD). The details of accelerators, characterization and data analysis methods used in the thesis work are present in this chapter.

2.2. Sample preparation

INRAFM samples of dimensions 12 mm×12 mm×0.7 mm were cut from a rectangular bar using Electric Discharge Machine (EDM). These samples were mechanically polished using SiC papers having grit size up to P4000. The samples were normalized at 1253 K for 30 mins and tempered at 1033 K for 1 h in a dynamic vacuum of 1×10^{-6} mbar. The range and depth-wise distribution of ions and vacancies were calculated using SRIM-2013 code [142]. From the ion and vacancy distribution profiles, concentration of helium and hydrogen ions in atoms parts per million (appm) and displacement damage in dpa has been calculated using the following relations,

$$\text{Concentration} = \frac{(\phi/\text{FWHM})}{N} \times 10^6 \text{ (appm)} \quad (2.1)$$

$$\text{Displacement damage} = \frac{\phi \times \text{vacancies}}{N} \text{ (dpa)} \quad (2.2)$$

Where ϕ is the ion fluence in ions/cm² and N is the atomic density in atoms/cm³. Full width at half maximum (FWHM) of ion distribution peak and the number of vacancies per ion are obtained from SRIM calculation [142]. For the calculation of dpa, the peak value of vacancy

distribution obtained from SRIM calculation is used, and hence the dpa given in this study corresponds to peak displacement damage. A vacuum annealing station consisting of a diffusion pump based set up, and a cylindrical furnace is used for all thermal treatments. The samples were inserted into a quartz tube, one end of which is connected to the diffusion pump and the other end is inserted into the furnace. All the annealing treatments were done in a dynamic vacuum of 1×10^{-6} mbar.

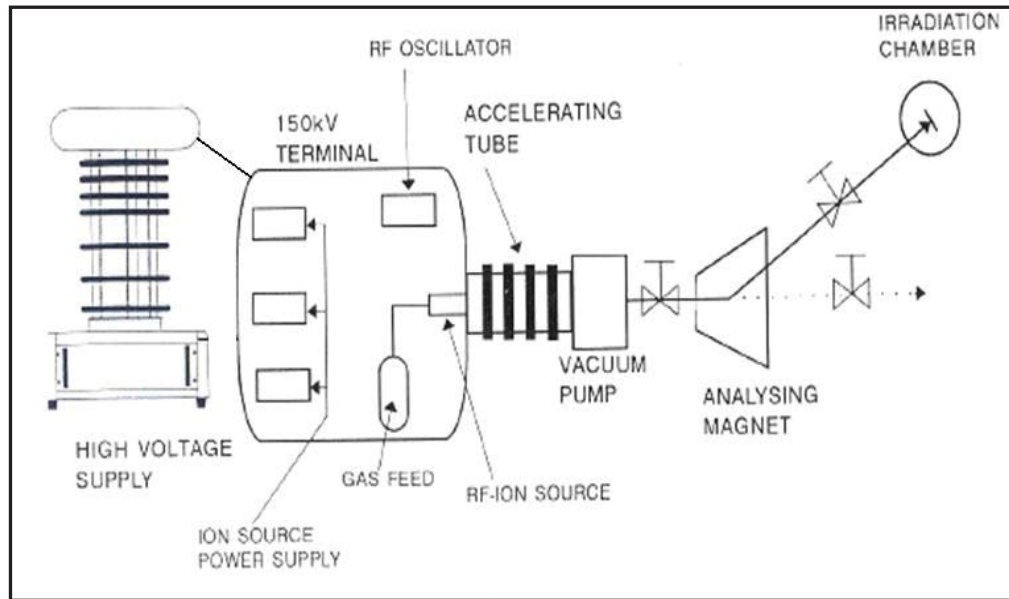


Figure 2.1 Schematic of the 150 keV ion accelerator used for He and H irradiations showing all major components.

2.3. Helium and hydrogen ion irradiations

Helium and hydrogen ion irradiations were performed using a 150 keV ion accelerator using a gaseous RF plasma source which generates gaseous ions. A schematic of the ion accelerator is shown in figure 2.1. The helium or hydrogen gases were filled in the gas-bottle at a pressure of approximately 2 mbar. The gas is then fed to a quartz tube through a fine needle valve where a radio frequency (RF) potential of 100 MHz frequency at a power of 100 W is applied to generate plasma. The gas pressure inside the tube was maintained at 10^{-3} to 10^{-2} mbar. The ions produced inside the plasma are extracted by applying an extraction voltage of 5 kV. The positive ion beam is then accelerated from a positive high voltage terminal to the target kept at ground potential. The high voltage is generated using a solid-state power supply. The high voltage is tunable from 30 to 150 keV. The final energy E of the ions depends on the extraction voltage V_i of the ion source, the charge e of the ions, and the acceleration voltage V_T applied at the high voltage terminal and is given by the relation,

$$E = eV_g E_x \quad (2.3)$$

The accelerated ions are mass analyzed by using a 45° electromagnet. The beam passes through an electrostatic quadrupole lens and a beam scanner to the target chamber for experiment. The machine is mainly used for implantation of ions of gaseous elements like H^+ , He^+ , N^+ , Ar^+ , etc. The entire beamline is maintained at a vacuum better than 10^{-6} mbar. The beam current and irradiation dose are calculated using a current integrator. If Q is the total charge collected by the current integrator, A is the area of irradiation or the cross-sectional area of the ion beam and q is the charge state of ions, then the total number of implanted ions can be calculated using the relation,

$$I = \frac{Q}{A} \quad (2.4)$$

Irradiations were performed with a circular beam having a diameter of around 12 mm.

2.4. Fe ion irradiation

Fe ion irradiations were performed using 1.7 MV tandemron accelerator (HVEE, Netherlands) at Materials Science Group, IGCAR. A schematic of the accelerator is shown in figure 2.2. The accelerator consists of a beam injection system, accelerator tank, electrostatic quadrupole lens, switching magnet followed by different irradiation and experimental beamlines. The beam injection system consists of an ion source followed by an injector magnet. The ion source consists of a high brightness duoplasmatron source for the production of H^+ and He^+ ions or a SNICS (Source of Negative Ions by Caesium Sputtering) source for the production of negative ions. The positive ions produced by the duoplasmatron ion source are converted into negative charges by charge exchange reaction with the lithium vapour. The negative ions from the ion source are mass analyzed and injected into the accelerating column using a 90° injector magnet having a resolution of $(M/\Delta M) \sim 190$.

The accelerator tank consists of a low-energy (L.E) end, stripper canal and a high-energy (H. E) end. The negative ions injected into the low-energy end with an initial energy E_i . These negative ions get accelerated towards the high voltage terminal located at the center of accelerator tank by applying a terminal voltage of V_T . At the high voltage terminal, the negative ions are converted into positive ions by passing through a stripping canal where the N_2 gas is fed. At the stripping canal, the negative ions get stripped and positive ions having various charge states are formed.

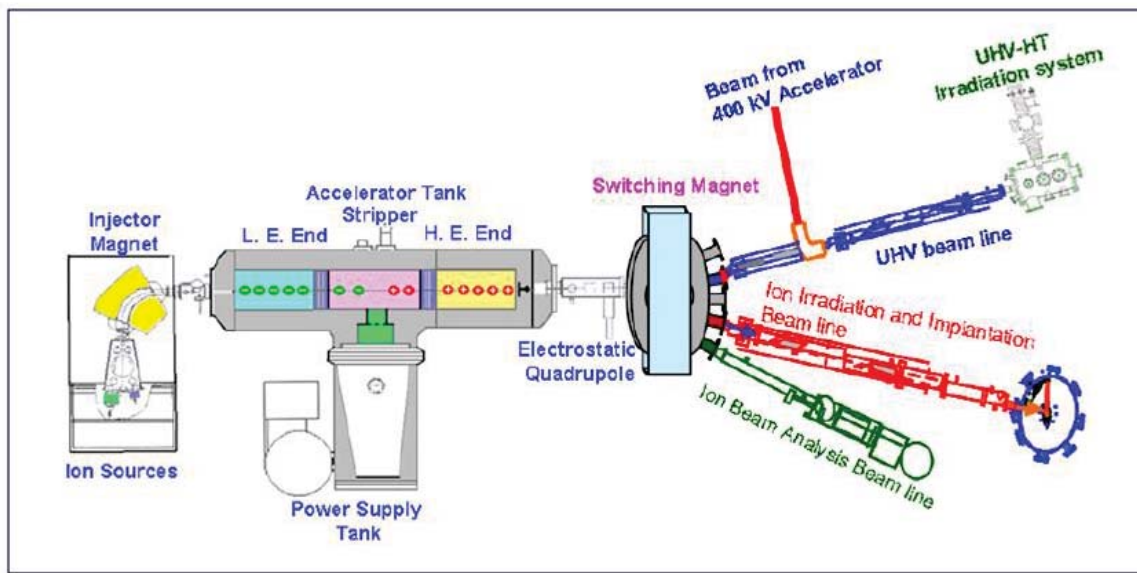


Figure 2.2 Schematic of 1.7 MV tandemron accelerator (M/S HVEE, Netherlands) at IGCAR, Kalpakkam.

These positive ions get further accelerated in the high energy end. Hence, by utilizing the principle of charge-stripping, a single high voltage terminal is used for accelerating the ions two times. The high voltage required for acceleration is achieved by using a Cockcroft-Walton type capacitive-coupled parallel fed solid-state power supply. The final accelerating voltage varies from 100 kV - 1.7 MV with a voltage stability of ± 100 V. The total energy (E) gained by the ions of any charge state (q) can be obtained by,

$$E = L_g E_0 : E \propto s; \quad x \quad (2.5)$$

The maximum energy achievable is decided by the charge state of the ions at the terminal after stripping. The entire accelerating structure consists of the accelerating tubes, high voltage terminal, and power supply is enclosed in a pressure vessel filled with SF₆ gas at 6 kg/cm² for achieving high voltage insulation. A turbo-molecular pump has been installed at the high voltage terminal in order to maintain a vacuum of 10⁻⁶ mbar in the accelerating tubes and to ensure the recirculation of stripper gas. The accelerated ions from the high energy end are focussed using electrostatic quadrupole lens. The high energy switching magnet has been used to select the charge state of ions and switches the beam to experimental ports located at $\pm 10^\circ$ and $\pm 30^\circ$ angular positions. There are three beamlines currently installed in the accelerator. An implantation beamline with beam sweeping system, neutral trap, beam profile monitor and retractable slits for beam collimation has been installed at the -10° port of the switching magnet. A second beamline at -30° port for ion beam analysis and the third beamline at $+10^\circ$ port of the switching magnet for UHV high-temperature dual beam

implantation. The accelerator has been controlled using PC based automation through optical fibre cables.

2.5. Variable low-energy positron beam based Doppler broadening spectroscopy

The study of depth-wise distribution of irradiation-induced open volume defects in the samples was carried out using variable low-energy positron beam based Doppler broadening spectroscopy. The working principle of variable low-energy positron beam set up is illustrated in figure 2.3. The positron beam set up consists of a 50 mCi strong ^{22}Na radioactive source which emits positrons by spontaneous radioactive decay. The positrons emitted from the ^{22}Na source are having a broad energy distribution up to 540 keV, as shown in figure 2.4 (a). A W(100) thin-film moderator has been used to slow down the fast positrons. Typical interactions of positrons with a 2 μm thick W(100) thin-film moderator is shown in figure 2.4 (b) [87]. Majority of the positrons falling on the W(100) moderator film is transmitted without any moderation.

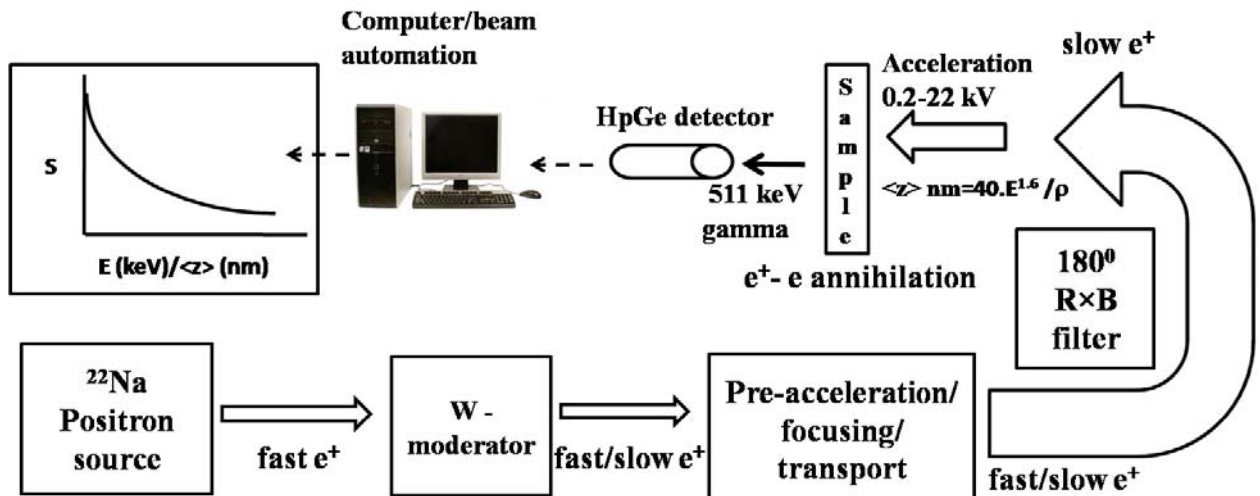


Figure 2.3 Illustration of the working principle of variable low-energy positron beam based Doppler broadening set up.

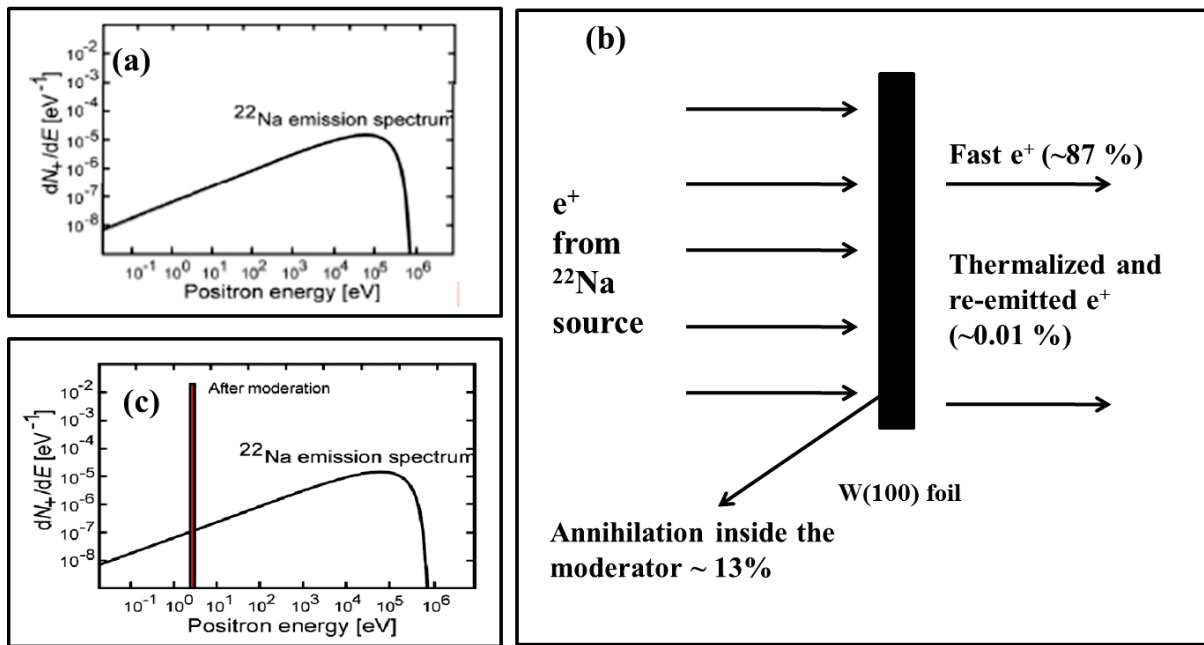


Figure 2.4 a) ^{22}Na e^+ emission spectrum b) interaction of e^+ with a $2\ \mu\text{m}$ thick W(100) thin-film moderator and (c) emission spectrum of moderated e^+ from a W(100) moderator. The figures were reused with permission from ref [87] (Copyright: Springer (1999)).

A fraction of the positrons undergo thermalization and annihilate inside the moderator. Another fraction of the positrons thermalize and reach the surface during diffusion. Majority of these thermalized positrons reaching the surface get trapped in surface states and form positronium. Due to the negative positron work function of W(100), a very small per cent ($\sim 0.01\ %$) of these thermalized positrons get re-emitted with an energy equal to the work function of moderator (2.6 eV). A $1\mu\text{m}$ thick W(100) moderator has been used in the current set up. The energy spectrum of positrons emitted from the moderator is shown in figure 2.4 (c). The moderated positrons are then accelerated to 240 eV and focused using a combination of asymmetric einzel lens and two-tube lens. The positrons are then transported using a solenoid magnetic field of 70 gausses. The slow-positrons are extracted from the fast positrons by using an $R \times B$ filter having a U-shaped solenoid bend. The extracted slow-positrons are then accelerated towards the sample by applying a negative high voltage at the sample side. The accelerating voltage can be varied from 0.2-22 kV. The complete details of the beam design have been given elsewhere [143]. An HPGe detector having an energy resolution of 1.45 keV at the 662 keV gamma line of ^{137}Cs is used for Doppler broadening measurements. The beam automation was carried out using a Programmable System on Chip (PSoC) and LabVIEW programme [144]. A photograph of the experimental set up is shown in figure 2.5.

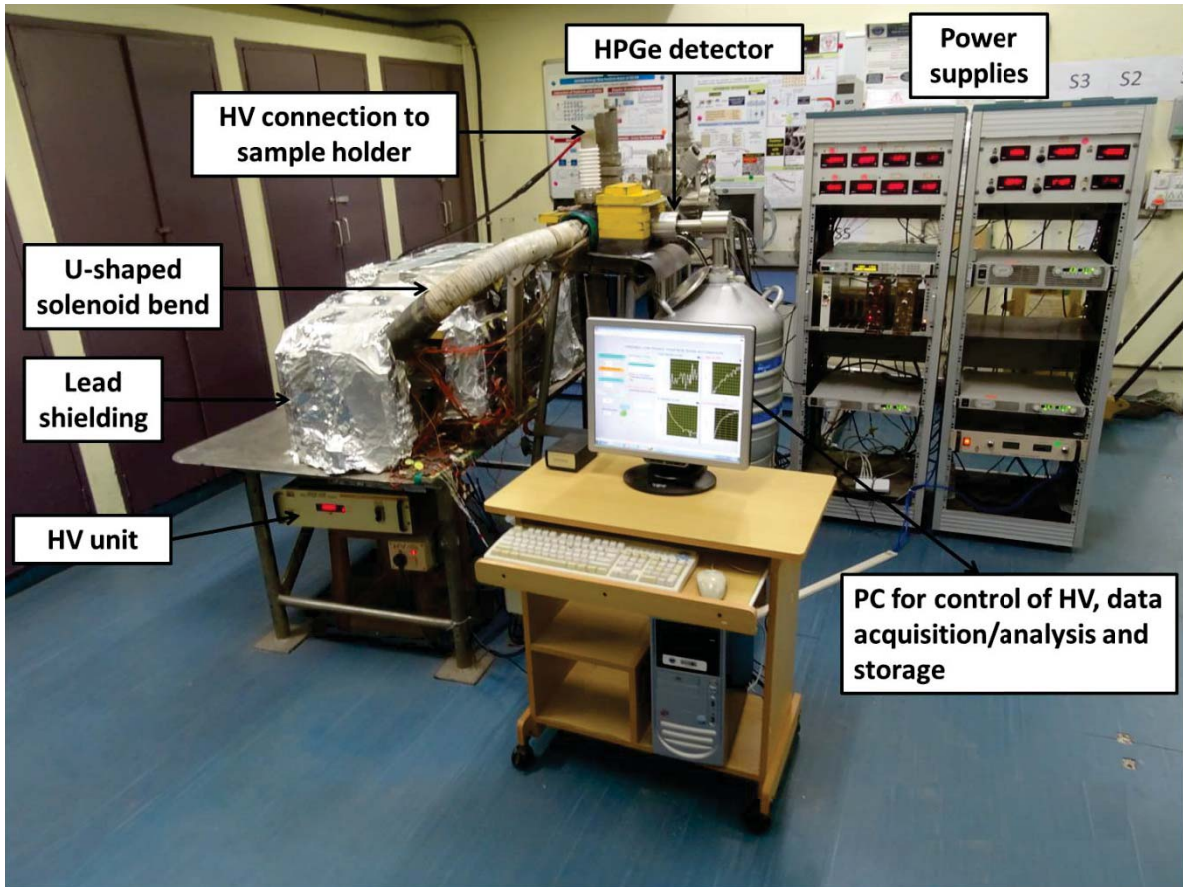


Figure 2.5 Photograph of the variable low-energy positron beam based Doppler broadening spectroscopic technique at IGCAR, kalpakkam [143].

From the Doppler broadened positron annihilation spectra, the defect sensitive S (shape parameter) and W-parameters (wing parameter) are defined [87]. The S-parameter is defined as the ratio of counts in the central energy region (511 ± 1 keV) to the total counts under the spectrum (511 ± 10 keV). The W-parameter is the ratio of counts under the wing area (506-508 keV and 514-516 keV) to the total counts under the spectrum (511 ± 10 keV).

The implantation profile of positrons at any energy E is generally represented by the Makhovian profile [87] given by,

$$P(Z, E) = \frac{mZ^{m-1}}{Z_0^m} \exp \left[- \left(\frac{Z}{Z_0} \right)^m \right] \quad (2.6)$$

Where,

$$Z_0 = \frac{AE^r}{\rho \Gamma \left(1 + \frac{1}{m} \right)} \quad (2.7)$$

and m , r , A are the material-dependent empirical parameters. ρ is the mass density of the material and Γ is the gamma function. $A = 4.0 \text{ } \mu\text{gcm}^{-2}\text{keV}^{-r}$, $m=2$, and $r=1.6$ are the widely used values of the empirical parameters. The mean-implantation depth ($\langle Z \rangle$) of positrons into the material is given by the relation:

$$\langle Z \rangle = \frac{AE^r}{\rho} \quad (2.8)$$

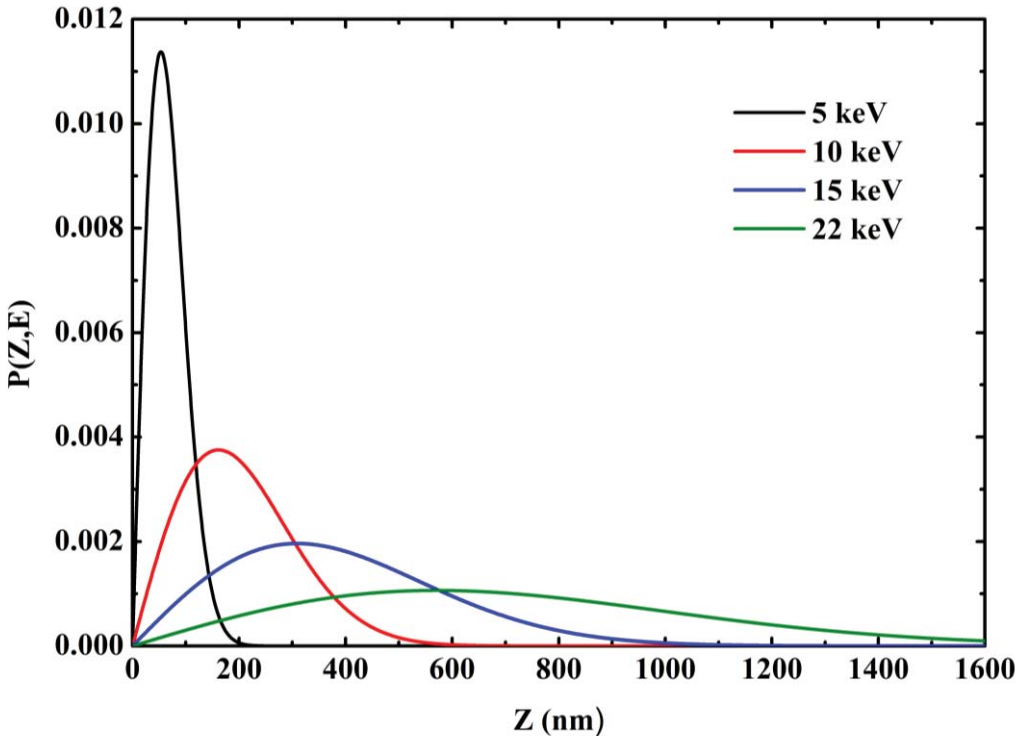


Figure 2.6 Implantation profile (Makhovian) of positrons into INRAFM steel at various energies.

Figure 2.6 shows the Makhovian profile of positrons into INRAFM steel. The positrons enter into the solids with definite kinetic energy which dissipates within a few picoseconds time and reaches thermal energy of diffusion. The implantation profile provides the depth-distribution of positrons prior to thermalization. The implantation profile is sharp at low positron energies. As the positron energy increases, the broadening in the implantation profile increases. Once the positrons get thermalized, their diffusion in the crystal lattice can be described using the time-dependent diffusion equation [87],

$$\frac{\partial^2 \rho}{\partial z^2} + \frac{2}{D} \frac{\partial \rho}{\partial z} - \frac{\rho}{\tau_{dd}} = 0 \quad (2.9)$$

Where, $n(r, t)$ is the positron density at the position r and time t , D is the positron diffusion constant, v_d is the positron drift velocity, and λ_{eff} is the effective positron annihilation rate. The thermalized positrons get trapped in the defects during their diffusion. Since the positron beam measurements are probing the direction perpendicular to the sample surface, the equation 2.9 is reduced to a one-dimensional problem.

In the case of depth-dependent Doppler experiments, the diffusion of positrons after thermalization can be represented by a time-independent one-dimensional diffusion equation given by [87],

$$D \frac{d^2}{dZ^2} n(Z) - \frac{d}{dZ} [v_d n(Z)] - \lambda_{\text{eff}} n(Z) + P(Z, E) = 0 \quad (2.10)$$

$P(Z, E)$ is the positron implantation profile as a function of incident energy. Equation 2.10 has to be solved numerically in order to determine the depth profile of S and W-parameters. The VEPFIT programme [145] has been used to fit the annihilation parameters as the function of positron energy. The VEPFIT assumes that the sample is having a layered structure with a definite S-parameter and positron diffusion length for each layer. The measured S-parameter at any positron energy E can be written as,

$$S(E) = f_s(E)S_s + \sum_{i=1}^N f_i(E)S_i \quad (2.11)$$

Where f_s and f_i are the fractions of positrons annihilating in the surface and i^{th} layer, whereas S_s and S_i are the S-parameters of the surface and i^{th} layer.

For all the irradiated samples used in this study, the experimental S-parameter has been modelled as follows,

$$S(E) = f_s(E)S_s + f_{d1}(E)S_{d1} + f_{d2}(E)S_{d2} + \dots + f_{\text{bulk}}S_{\text{bulk}} \quad (2.12)$$

Where, the defected region is divided into multiple layers ($d1, d2, \dots$ etc) according to the features observed in the S vs. E curves, f_{d1}, f_{d2}, \dots etc are the fractions of positrons annihilating in each defected layer and S_{d1}, S_{d2}, \dots etc are the S-parameters of the corresponding layers. And $f_{\text{bulk}}, S_{\text{bulk}}$ are the fraction and S-parameter values of the unirradiated bulk layer.

S-W correlation plots

Since both S and W parameters are sensitive to the concentration and nature of the defects, the information on the nature of defects can be deduced by defining another

parameter called R-parameter. By assuming a two-state (bulk and defect states) trapping model, the S and W-parameters can be written as [87],

$$S = (1 - \eta_d)S_b + \eta_d S_d \quad (2.13)$$

$$W = (1 - \eta_d)W_b + \eta_d W_d \quad (2.14)$$

Where, η_d is the fraction of positrons trapped at the defect state, S_b , S_d and W_b , W_d are the S and W-parameters of the bulk and defect state. The above equations can be rearranged as,

$$S - S_b = \eta_d(S_d - S_b) \quad (2.15)$$

$$W - W_b = \eta_d(W_d - W_b) \quad (2.16)$$

The R-parameter can be defined as,

$$|R| = \frac{S - S_b}{W - W_b} = \frac{S_d - S_b}{W_d - W_b} \quad (2.17)$$

Since η_d is the only term in equations (2.13) & (2.14) that depends on the concentration of the defects, hence the elimination of η_d from equation (2.17) makes R-parameter independent of the concentration of the defects. As shown in the S-W correlation plot in figure 2.7, the slope of the straight line through the (W_b, S_b) and (W_d, S_d) gives the R-parameter. All the (W, S) co-ordinates lie along the straight line shows similar kind of defects. Hence, even though the line shape parameters provide qualitative information, the presence of different types of defects present in the sample can be identified by using an S-W correlation plot.

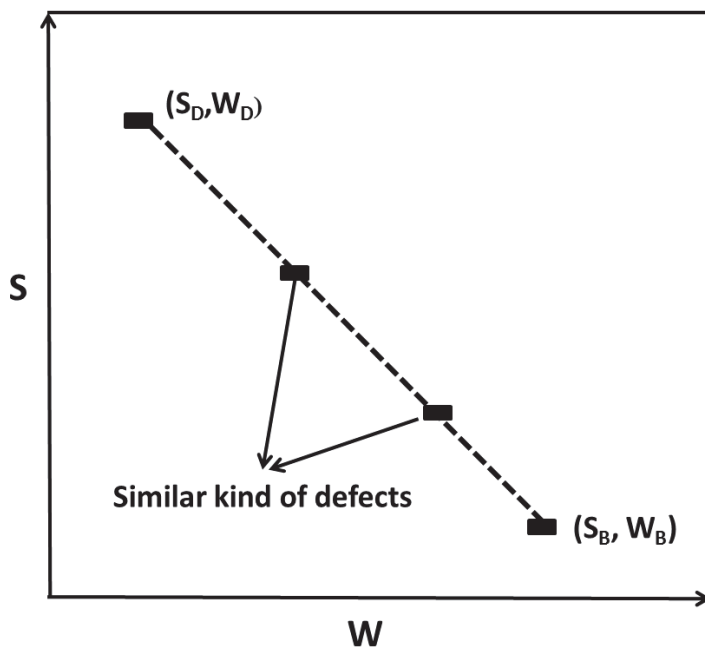


Figure 2.7 Typical S-W correlation plot of a sample containing similar kind of defects.

2.6. Secondary Ion Mass Spectrometry (SIMS)

Depth profiling of implanted helium in INRAFM steel was measured using Secondary Ion Mass Spectrometry (SIMS). SIMS is a highly sensitive technique for the surface composition analysis having elemental detection limit ranging from parts per million (ppm) to parts per billion (ppb) atomic concentrations. SIMS employs sputtering of the sample surface using primary ion beams such as Cs^+ , O^{2+} , O^- , Ar^+ , and Ga^+ having an energy of the order of a few keV. The sputtered secondary species from the sample surface consists of neutral or charged atoms and clusters having energies up to a few hundred eV. The secondary ions are extracted by applying an electric potential and analyzed using a mass analyzer to obtain the composition of the material. An unirradiated INRAFM sample is used as the reference sample for trace element analysis.

SIMS measurements were carried out using M/S CAMECA make IMS 7f instrument with 5 nA of 5.5 keV Cs^+ as the primary ions to sputter the sample surface. The primary ion beam was rastered over a square area of width 200 μm , and secondary ions were collected from a circular area of 62 μm diameter centered at the middle of the sputtered area. The secondary ions selected by the double-focusing mass analyzer were detected using the electron multiplier. The intensity vs. sputtering time profile was converted into depth profile by measuring the depth of the crater created by sputtering. The crater depth was measured using a DEKTAK 6M stylus profilometer.

The sensitivity of the SIMS to a particular secondary ion species (M) depends on the sputter yield and ionization probability. The secondary ion yield of the species M can be measured in terms of the secondary ion current (I_{MS}) given by [146],

$$I_{MS} = I_p S_M R_M \theta_M n \quad (2.18)$$

Where I_p is the primary particle flux, S_M , R_M and θ_M are the sputter yield, ionization probability and the fractional coverage of species M, and n is the transmission and detection efficiency of the analyser system.

2.7. Transmission Electron Microscopy (TEM)

Transmission Electron Microscopy (TEM) study was carried out on helium implanted INRAFM steel using M/S FEI Technai G2 F30 HRTEM operated at 300 kV. The ability of TEM to image various imperfections such as dislocations, grain boundaries, nanometer-sized voids, bubbles, precipitates etc. makes it a highly versatile technique to study the irradiation-induced microstructural changes in the materials. The cross-sectional samples required for the TEM study was prepared using Focused Ion Beam (FIB) technique attached to the Field Emission Gun-Scanning Electron Microscope (FEG-SEM), M/S FEI-Helios Nanolab 600i. The operating voltage of ion column ranges from 500 V to 30 kV, and the beam current varied from 1 pA to 65 nA. Final cleaning of the sample was carried out at a maximum voltage of 2 kV with an ion beam current of 6 pA. Helium bubbles were studied using underfocus and overfocus imaging conditions [83].

2.8. Grazing Incidence X-ray Diffraction (GIXRD)

The characterization of surfaces or thin films using conventional symmetrical Bragg Brentano ($\theta/2\theta$) XRD geometry produces strong signals from the substrate, which dominates the weak signals from the thin film. The Grazing Incidence X-ray Diffraction (GIXRD) has been used to study the surfaces and thin-film layers due to the limited penetration of the X-rays into the material at a low angle of incidence near to the critical angle. In this geometry, the incident angle of the X-ray beam is fixed at a small angle slightly exceeding the critical angle of total internal reflection, and the angle between the incident beam and the diffracted beam is varied [147]. The incident X-ray travels through the near-surface area or thin film for a long distance and produces the diffraction pattern. The angle (γ) between the incident beam and the sample surface is very small and equal to a few degrees or even less. In GIXRD measurements, the angle α is kept constant, and the detector is moved along the 2θ circle. The angle between the scattered beam and the sample surface is ($2\theta - \gamma$). In the GIXRD

configuration, reflections with distinct Bragg angles θ_{hkl} are caused by lattice planes that are neither parallel with the substrate surface nor with each other.

The distance travelled by the X-rays with an angle of incidence α in a layer of thickness t is given by [147],

$$l = t/\sin\alpha \quad (2.19)$$

For any material with attenuation coefficient μ , the primary criteria for choosing α is that

$$l \approx \frac{1}{\mu} \quad (2.20)$$

or,

$$\alpha \approx \sin^{-1}(\mu t) \quad (2.21)$$

Above relation should hold between α and μt for the effective measurement of the layer having thickness t .

The GIXRD measurements were carried out on the irradiated INRAFM samples using M/S Bruker D8 Discover instrument consisting of 6 kW Cu K α ($\lambda=1.540598$ Å) rotating anode with parallel beam geometry using a Soller slit and 2 mm collimator. The measurements were carried out using 5 kW anode power. The GIXRD data was analyzed using the Williamson-Hall plot method; the irradiation-induced changes in the micro-strain and coherent domain size was studied.

2.9. Nanoindentation

The mechanical properties of the materials at nano-scale dimensions have been studied using nanoindentation technique. Nanoindentation studies were performed on irradiated INRAFM steel samples to study the variation of nanohardness due to the presence of irradiation-induced defects. The nanoindentation measurements were carried out using a compact platform Ultra Nanoindentation Tester (M/S Anton Paar, Switzerland) equipped with a Berkovich three-sided pyramidal diamond tip with an end radius of 30 nm. The variation of nanohardness as a function of depth was studied using sinus mode based on the principle of Oliver and Pharr model [148]. The two most common mechanical properties of materials measured using the indentation techniques are the hardness (H) and elastic modulus (E). Figure 2.8 (a) shows a typical load (P) vs. displacement (h) curve in the nanoindentation experiments using a Berkovich tip. As the load increases, both the elastic and plastic deformation occurs, which results in the formation of permanent hardness impression on the

sample. During the indenter unloading, only the elastic portion of the displacement is recovered, which facilitates the modelling of the contact process using the elastic nature of the unloading curve. The important quantities that can be measured from the load vs. displacement curves are the maximum load (P_{\max}), the maximum displacement (h_{\max}), the elastic unloading stiffness (or contact stiffness) $S=dP/dh$ and the final displacement after complete unloading (h_f). A typical deformation pattern of the elastic-plastic material during and after indentation is shown in figure 2.8 (b). The nanoindentation hardness is defined as the ratio of the indentation load to the projected contact area (A) of indentation. i.e.

$$H = \frac{P_{\max}}{A} \quad (2.22)$$

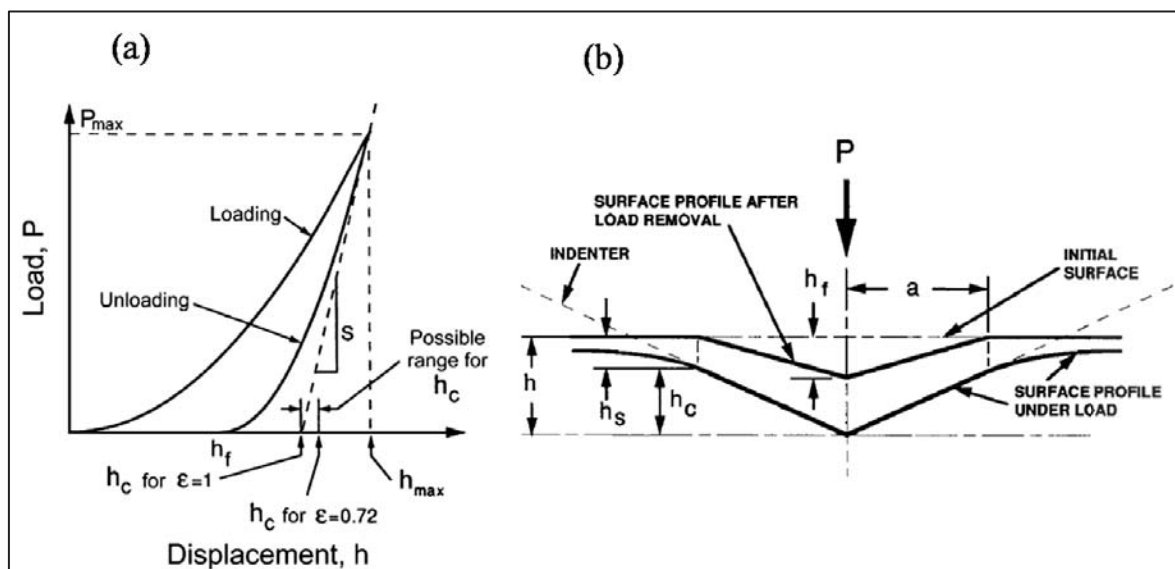


Figure 2.8 Schematic illustration of a) indentation load vs. displacement curve and b) the deformation pattern of the elastic-plastic sample during and after indentation. The figures were adopted from ref [149] with permission (Copyright: Elsevier(2002)).

The loading curve can be described by a power-law relation [150],

$$P = \alpha (h - h_f)^m \quad (2.23)$$

Where α and m are empirically determined fitting parameters.

For an indenter with known geometry, the projected contact area is a function of the contact depth (h_c). The area function of a perfect Berkovich indenter is given by,

$$A_c = 24.56h_c^2 \quad (2.25)$$

The contact depth can be estimated from the load-displacement curve using the relation

$$h_a L \propto v^{\frac{k}{k-1}} \quad (2.26)$$

where ε is the constant that depends on the indenter geometry. For the Berkovich indenter $\varepsilon=0.75$.

2.10. Summary

This chapter discussed brief details of experimental techniques used to carry out irradiation damage studies in INRAFM steel. In this thesis, variable low-energy positron beam based Doppler broadening spectroscopy is used as a major characterization technique to carry out irradiation damage studies. SIMS was used for the depth profiling of implanted helium ions in the sample. Irradiation effects in the near-surface region were studied using GIXRD and nanoindentation. TEM study was performed on FIB prepared sample of helium implanted INRAFM steel to study the formation of helium bubbles.

Chapter 3

Nucleation and growth of helium-vacancy complexes in RAFM steel

3.1. Introduction

Neutron irradiation introduces helium into core structural materials of a nuclear reactor via (n, α) transmutation reaction, which leads to changes in the microstructural as well as mechanical properties of the material [151]. In fusion reactors, in addition to the (n, α) reactions induced by 14.1 MeV fusion neutrons, helium is directly introduced into the plasma-facing materials of first-wall by the deuterium-tritium fusion reaction. Being an inert atom, helium doesn't undergo any chemical reaction with the constituent elements. Helium atoms will interact with pre-existing defects in the material such as dislocations, grain boundaries, precipitate-matrix interface, and voids as well as with the irradiation-induced defects [46, 65, 79, 152-154]. Helium atoms stabilize the vacancies and vacancy clusters against the vacancy-interstitial recombination, thereby promoting the growth of cavities. This enhanced growth of cavities assisted by helium can promote void swelling and premature deterioration of mechanical properties of the nuclear core structural materials [40, 41, 155].

The deterioration of the desired mechanical properties of materials due to helium bubble growth occurs mainly at a temperature of around $0.45T_m$, where T_m is the melting point [46]. Helium bubbles are nucleated inside the grains as well as at the crystalline defects such as dislocations, grain boundaries, sub-grains, precipitate-matrix interface etc. in materials [60, 83, 152, 153, 156]. Helium bubble formation on individual dislocations as well as on the nodal points of dislocation networks has been reported in metals [152]. A post-implantation annealing study shows the growth of helium bubbles associated with significant desorption of helium at 873 K in FeCr model alloys [157]. An increase in nanohardness is reported in EUROFER-97 steel due to the formation of nano-bubbles induced by room temperature helium implantation [83]. The inherent trapping sites in RAFM steels such as dislocations, lath boundaries, and grain boundaries act as nucleation and growth centres for helium bubbles [158]. A slow positron beam study combined with nanohardness measurements showed a heterogeneous distribution of defects within the damaged region and a peak hardness at 473 K in helium implanted CLAM steel [139]. Various stages of annealing in helium-implanted EUROFER-97 steel corresponding to the release of helium from over-pressurized He_mV_n clusters and vacancy annealing (<600 K), dissociation of smaller clusters

and the formation of larger He_mV_n clusters with $m < n$ (600 to 1200 K) and helium release from bubbles (> 1200 K) have been reported using thermal desorption spectroscopy [141]. Another thermal desorption study on a reduced activation ferritic steel observed peaks corresponding to the desorption of helium from the sample surface (at 373 K), de-trapping of helium from He-vacancy pairs (at 723 K) and dislocations (at 823 K), α to γ phase transformation (at 1173 K) and desorption by bubble migration (at 1373 K) [159]. The size and number density of bubbles evolved during the production of helium by implantation, or nuclear transmutation are dependent on the parameters such as irradiation temperature, He production rate, displacement rate and accumulated He concentration or dose [46]. The presence of external tensile stress during implantation also enhances the helium bubble growth [160]. Though helium behaviour in steels has been studied for the past couple of decades, the surface proximity effect on the release and clustering of helium is still not well understood. The present chapter discusses the effect of helium dose and post-implantation annealing temperature on the formation and clustering of helium associated defects in INRAFM steel occurring at near-surface regions.

3.2. Experimental

3.2.1. Helium ion irradiation

Two sets of normalized and tempered INRAFM steel samples were prepared and one set of samples was irradiated with 130 keV He ions to a fluence of 5×10^{14} ions/cm² (low-dose) and another to a fluence of 1×10^{16} ions/cm² (high-dose). The irradiations were carried out at room temperature using a beam current of 1 μ A. The pressure inside the irradiation chamber was maintained at 1×10^{-6} mbar. Figure 3.1 shows the range and distribution profile of He ions and vacancies in INRAFM steel using SRIM 2013 code [142]. The SRIM calculations were performed using full-cascade mode using a total of 10^5 helium ions. As seen in figure 3.1, helium distribution peak occurs around 410 nm, whereas the vacancy distribution peak occurs around 360 nm. The peak displacement damage calculated for high-dose and low-dose samples are 0.45 dpa and 0.02 dpa, respectively. The total helium concentration accumulated in high-dose and low-sample samples are 5600 appm and 280 appm, respectively.

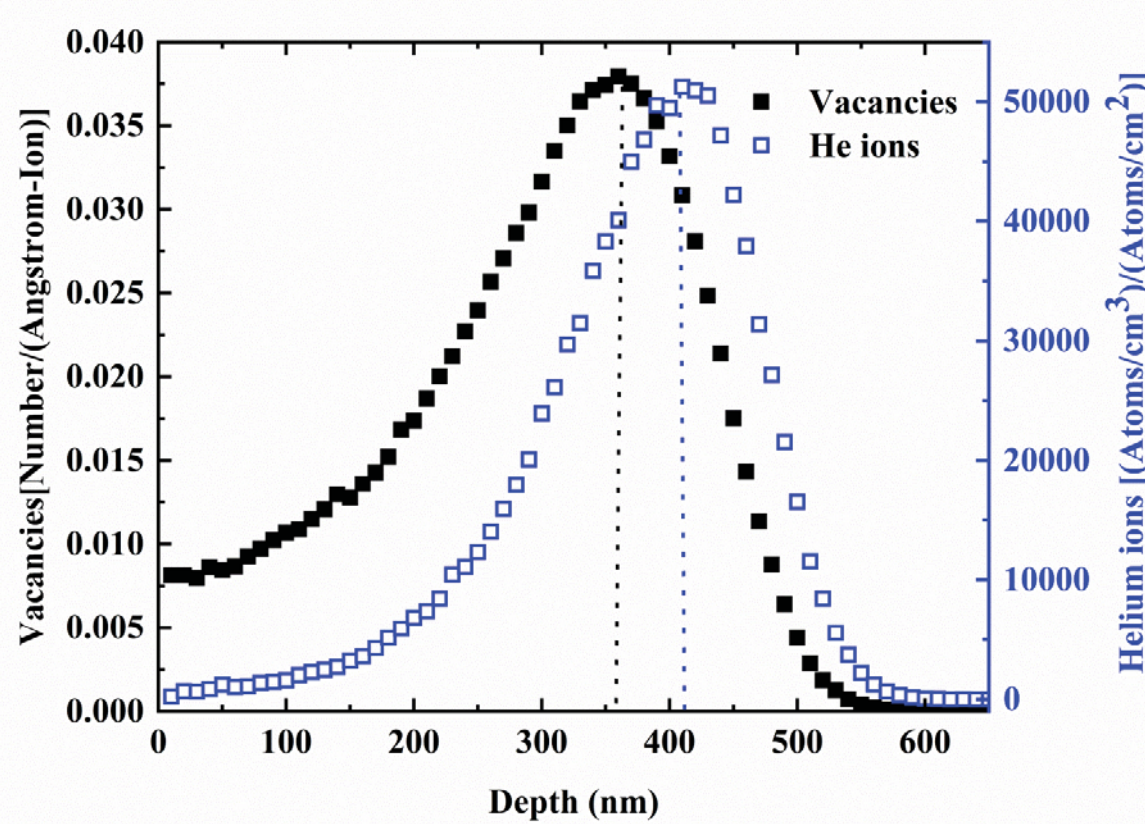


Figure 3.1 Helium ion and vacancy distribution profiles of 130 keV helium ions into INRAFM steel calculated using SRIM 2013 code. Vacancy and helium distribution peaks are shown using dotted lines.

3.2.2. Secondary Ion Mass Spectrometry

The depth profiling of He ions in high-dose samples was obtained by using Secondary Ion Mass Spectrometry (SIMS). The irradiated samples were isochronally annealed from RT to 973 K, and the He depth profiling was carried out at selected temperatures. An unirradiated INRAFM sample was used as a reference for trace element analysis.

3.2.3. Positron annihilation studies

Irradiated samples were isochronally annealed from room temperature up to 973 K, in steps of 100 K and characterized by positron annihilation Doppler broadening spectroscopy at each annealing step. An unirradiated sample was also annealed along with the irradiated samples and used as a reference sample. Positron beam measurements were carried out by tuning the energy of positrons from 0.2 to 22 keV in steps of 0.5 keV. The Doppler-broadened spectrum was taken at each energy step by collecting approximately 10^6 counts using a HPGe detector having an energy resolution of 1.4 keV for ^{137}Cs gamma rays. The S and W-parameters were deduced from the Doppler broadened spectrum. The S-parameter vs. positron beam energy plots were analyzed using VEPFIT programme [145].

3.2.4. Transmission Electron Microscopy

TEM studies were performed on the high-dose sample annealed at 773 K. Thin sample required for the TEM measurement was prepared using Focussed Ion Beam (FIB) technique. Helium bubbles were identified using overfocus and underfocus imaging conditions [83].

3.3. Results and discussion

3.3.1. Secondary Ion Mass Spectrometry study

Figure 3.2 shows the depth profiling of He in irradiated INRAFM steel samples using SIMS. He ions are distributed up to 500 nm from the surface of the sample. The peaks were fitted with a Gaussian profile in order to deduce the centroid of the peak. As-irradiated sample shows He distribution with peak intensity at 315 ± 0.4 nm. The as-irradiated sample was cumulatively annealed up to 973 K in steps of 100 K with a holding time of 1 h at each annealing step. SIMS studies at selected temperatures (573, 773 and 973 K) were performed, and a systematic reduction in the peak intensity of He distribution is observed as the annealing temperature is increased up to 973 K. The observed reduction in peak intensity is due to the release of He from the matrix due to high-temperature annealing. He release from ferritic steels at high temperatures was studied using thermal desorption spectroscopy and reported previously [141, 159]. Significant He desorption is observed in 9Cr-ferritic steels at temperatures around 723 and 823 K due to helium bubble growth and dislocation annealing, respectively [159]. Another major desorption peak observed between 1023 to 1273 K due to α to γ phase transition in 9Cr-ferritic steels [159]. A study on EUROFER-97 steel that was normalized and tempered at temperatures similar to the current study had attributed the He desorption peaks up to 600 K to the release of He from over-pressurized He_mV_n clusters. Another peak between 600 to 1200 K is due to the growth of larger clusters and the peak due to transition from α to γ phase occurs around 1200 K [141].

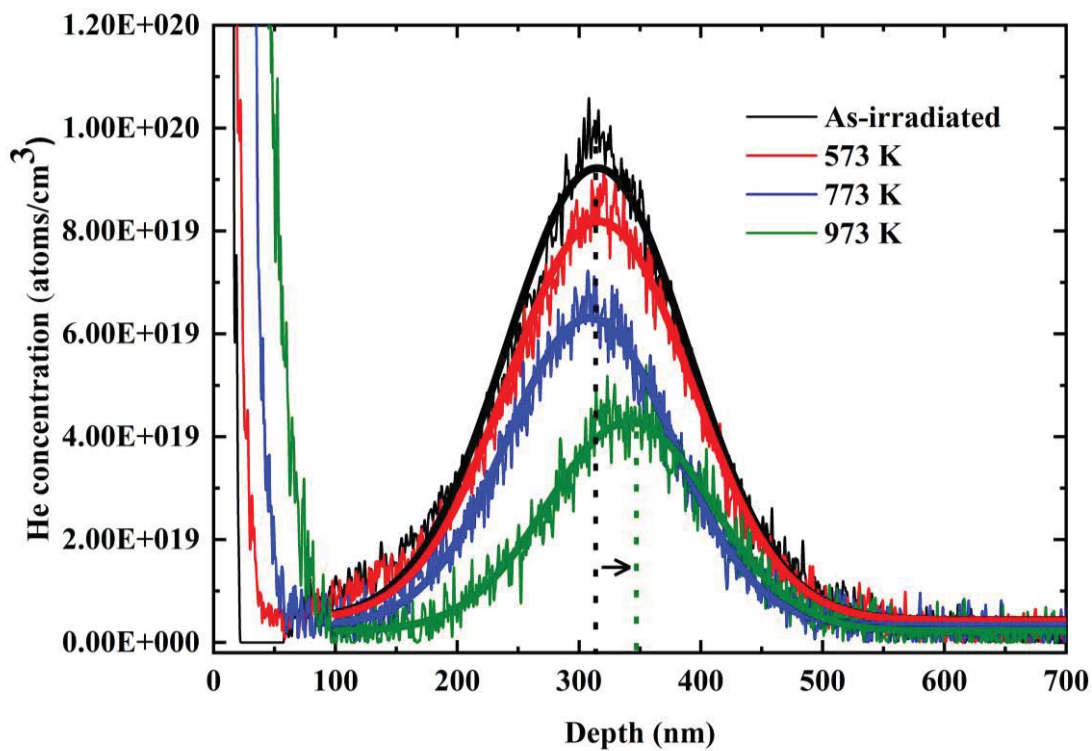


Figure 3.2 Distribution of He ions into the irradiated INRAFM steel samples measured using SIMS. Peak of He distribution in the as-irradiated and 973 K samples are shown using dotted lines.

Hence, in the current study, the reduction in He peak intensity observed at 573 K is due to the release of He from over-pressurized He_mV_n complexes, and the reduction in peak intensity from 773 to 973 K is due to the dissociation of He-vacancy complexes associated with the growth of larger clusters or He bubbles. Since the samples were already tempered at 1023 K, the contribution of dislocation annealing to the reduction in He peak intensity at 973 K may be less significant. At high temperatures, He bubbles migrate towards both directions from the peak intensity region. The free surface acts as a sink for bubbles, and those bubbles migrate towards the surface may de-trap He easily as compared to those migrating towards the interior. Hence at 973 K, the peak position shifted to 342 ± 0.7 nm, which may be due to the de-trapping of He from bubbles present in the near-surface regions.

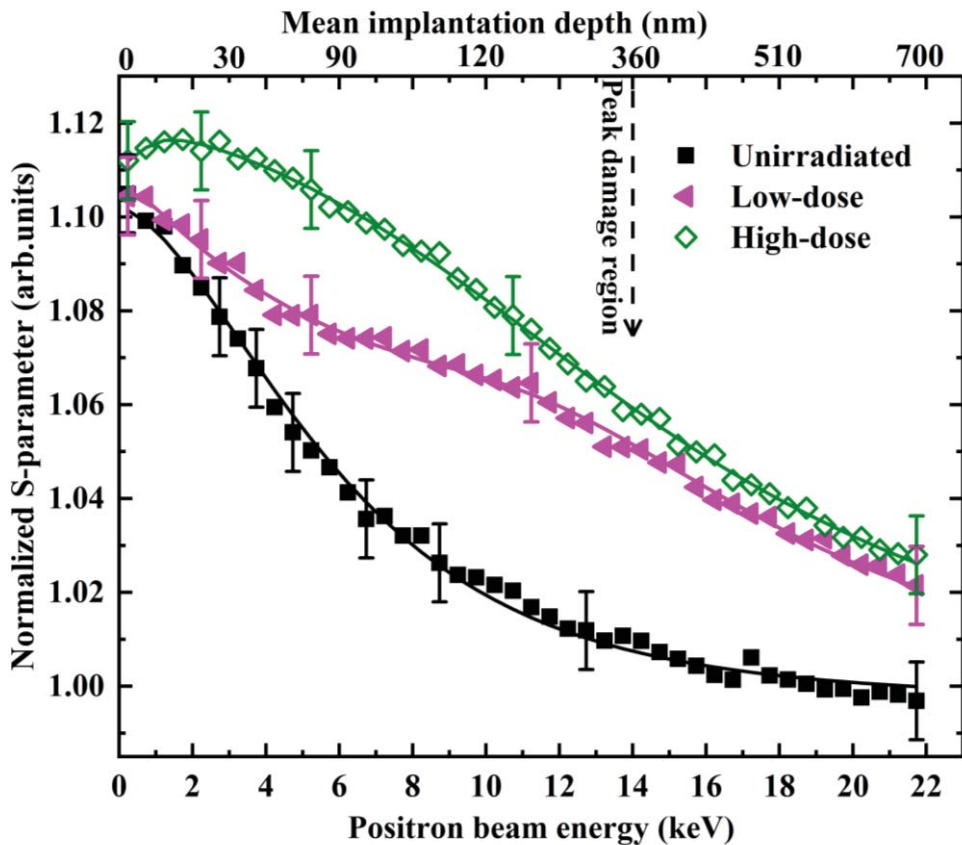


Figure 3.3 Normalized S-parameter vs. positron beam energy plots of as-irradiated and unirradiated reference samples. S-parameter values were normalized with respect to the unirradiated bulk value. The data points were fitted using VEPFIT programme. Positron mean implantation depth is shown on the top x-axis. The peak damage region is indicated on top axis.

3.3.2. Positron annihilation studies

3.3.2.1. As-irradiated samples

The normalized S-parameter vs. positron beam energy plots of unirradiated and as-irradiated samples are shown in figure 3.3. All S-parameter values were normalized with respect to the bulk S-parameter of the unirradiated sample. The mean implantation depth of positrons is shown along the top x-axis. The peak damage region as predicted by SRIM calculation is shown using an arrow. The unirradiated sample shows a higher S-parameter at the surface due to the presence of surface positron traps, which decreases with increase in positron energy and almost saturates at higher positron energies, where the bulk value is attained. Both as-irradiated samples show a higher S-parameter as compared to the unirradiated sample due to the presence of irradiation-induced defects. The defected region of both irradiated samples extends even beyond the range of He ions predicted by SRIM calculation. This is because the SRIM calculation does not take the temperature into account

and neglect the diffusion and clustering of point defects. This may alter the exact location and width of the peak damage region from the SRIM calculation. He implanted sample will be rich in vacancy-type defects such as vacancies, vacancy clusters and He-vacancy complexes, which are usually represented by He_mV_n , where m and n are the number of He atoms and vacancies present in the complex. As-irradiated samples show a higher S-parameter as compared to the unirradiated sample due to the presence of these irradiation-induced vacancy-type defects and He_mV_n complexes with low m/n ratio. The high-dose sample shows higher S-parameter as compared to the low-dose sample due to the higher concentration of vacancy-type defects present in the former. The difference in S-parameter between the irradiated samples is high at near-surface regions, as compared to the deeper regions. Also, the high-dose sample shows a broad peak in S-parameter around 30 nm depth region. Due to their low migration energy, mono-vacancies in α -Fe matrix are mobile at room temperature, leading to the formation of three-dimensional vacancy clusters [161]. The enhanced migration of vacancies towards the surface and their clustering at near-surface regions is the reason behind the near-surface peak (~ 30 nm) and the higher S-parameter shown by the high-dose sample in the near-surface region.

S-W correlation plots of unirradiated and as-irradiated sample are shown in figure 3.4. The linear nature of the S-W plot of unirradiated sample shows the presence of a single kind of defect in the sample. Since the RAFM steels are having a dislocation rich microstructure, the positron trapping sites present in the unirradiated sample is most probably associated with dislocations [162]. Both irradiated samples deviate from the linear nature as exhibited by unirradiated sample, due to the presence of irradiation-induced defects. The S-W curve of low-dose sample shows two slopes corresponding to near-surface and peak-damage regions. This is an evidence for the presence of defect-complexes having different nature present in the near-surface and peak-damage regions. The high-dose sample shows three linear regions in the S-W correlation plots. In the as-irradiated samples, the presence of different defected regions may be due to the depth-wise variation of m/n ratio associated with He_mV_n complexes. The near-surface regions may be rich in He_mV_n complexes with high vacancy content, while m/n ratio increases at deeper depth regions. This is evident from the SRIM profile (figure 3.1) where He distribution peak occurs deeper (~ 410 nm) as compared to the vacancy peak (~ 360 nm).

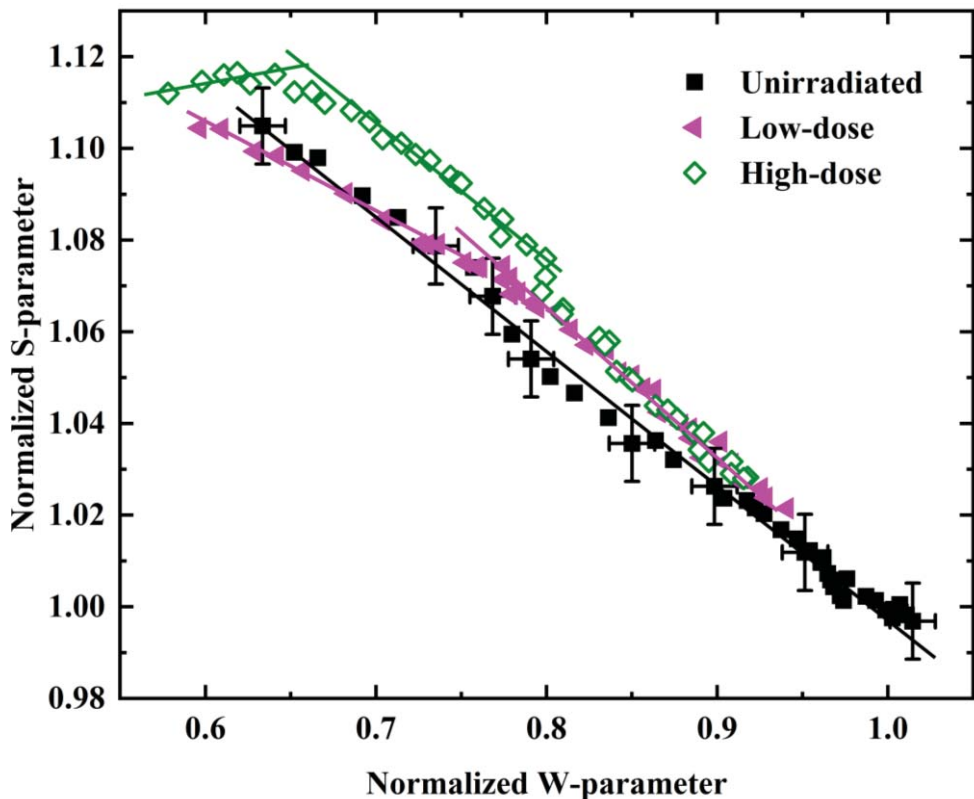


Figure 3.4 S-W correlation plot of the as-irradiated samples. The S and W parameters were normalized with respect to the unirradiated bulk values. The unirradiated sample exhibits linear behaviour throughout the measurement depths, whereas the irradiated samples deviate from the linear trend indicating the presence of higher defect species.

3.3.2.2. Isochronal annealing study: Low-dose sample

The normalized S-parameter vs. positron beam energy plots of the low-dose sample along with the unirradiated sample are shown in figure 3.5. The unirradiated sample is annealed up to 973 K is also shown for comparison. As can be seen, both unirradiated sample and 973 K annealed sample exhibit almost comparable S-parameter values and variation. This clearly establishes that the microstructure existing at unirradiated state is unaffected by thermal annealing even up to 973 K. As-irradiated low-dose sample shows a broad shoulder that extends from 140 to 430 nm in the irradiated region, which encloses the vacancy distribution peak (at 360 nm) predicted by SRIM. As annealing temperature increases, the S-parameter shows a systematic reduction till 573 K. The S-parameter stood stable from 573 to 773 K and increases with further annealing from 773 to 973 K. Since the maximum damage region pertains to a depth range around 360 nm, the average of S and W-parameters in the interval 360 ± 150 nm (or 210 to 510 nm) have been calculated in order to depict the changes occurring in this depth range. The average values are used since the VEPFIT analysis of W-

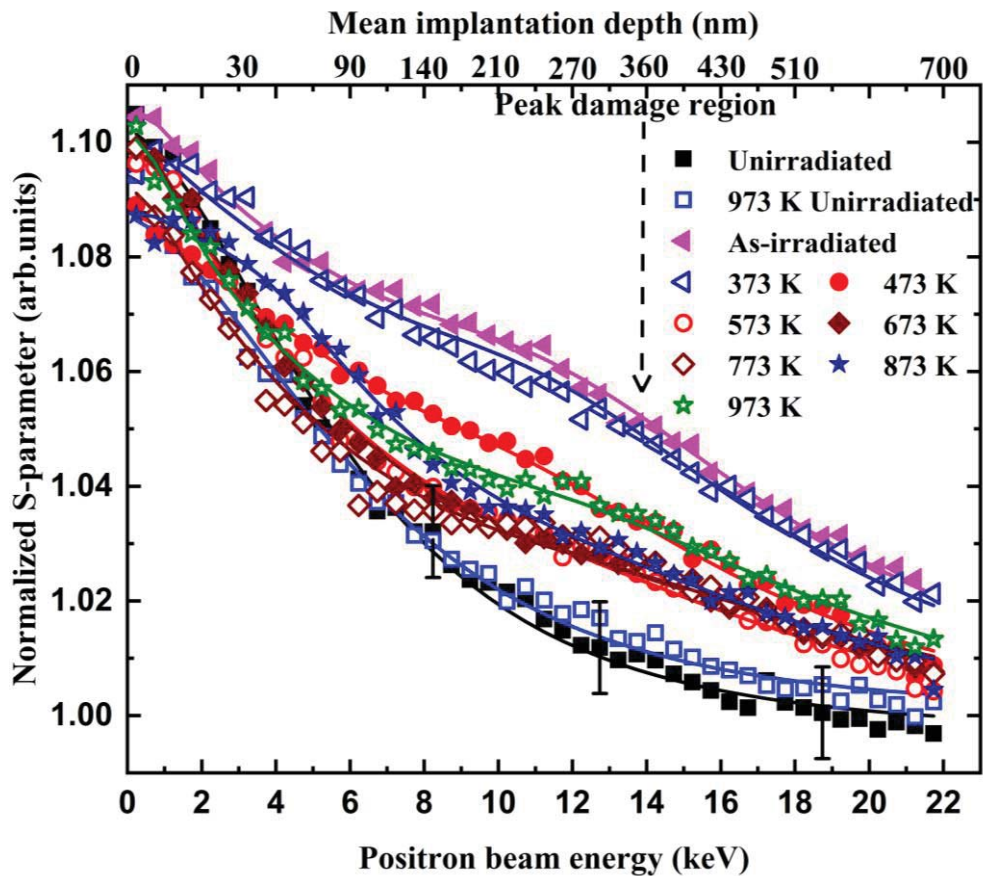


Figure 3.5 Normalized S-parameter vs. positron beam energy plots of the low-dose samples. Positron mean implantation depth is shown along the top x-axis. The data points were fitted using VEPFIT programme.

parameter is difficult as compared to S-parameter fitting. The average of normalized S and W-parameters are plotted against the annealing temperature and shown in figure 3.6. The S_{avg} vs. temperature plot has been divided into three regions, a decrease in S_{avg} from RT to 573 K due to defect annealing, a stable S_{avg} region from 573 to 873 K due to bubble nucleation and an increase in S_{avg} at 973 K due to He bubble growth. Due to the low interstitial migration energy (~ 0.06 eV) of He atoms in ferritic matrix, those He atoms occupying the interstitial positions or released from over-pressurized He_mV_n complexes can migrate faster even at low temperatures [163]. During migration, these He atoms may get trapped in vacancies or vacancy clusters present in the matrix and form stable He_mV_n complexes [139, 141]. Due to this He filling into vacancies and vacancy clusters, as shown in figure 3.6, the average S-parameter (S_{avg}) decreases from the as-irradiated state to 573 K. A He-vacancy complex of the type He_mV_n has higher core electron annihilation probability as compared to a vacancy cluster of the type V_n [74]. Since the increase in He concentration inside a vacancy or vacancy cluster increases the core electron annihilation probability, the gradual increase of

average W-parameter (W_{avg}) in this temperature region also confirms the increase in He/vacancy ratio of the clusters via the formation of He_mV_n complexes. Hence, the decrease in S_{avg} associated with an increase in W_{avg} shows that sample annealed at 573 K mainly consists of smaller He-vacancy complexes of the type He_mV_n .

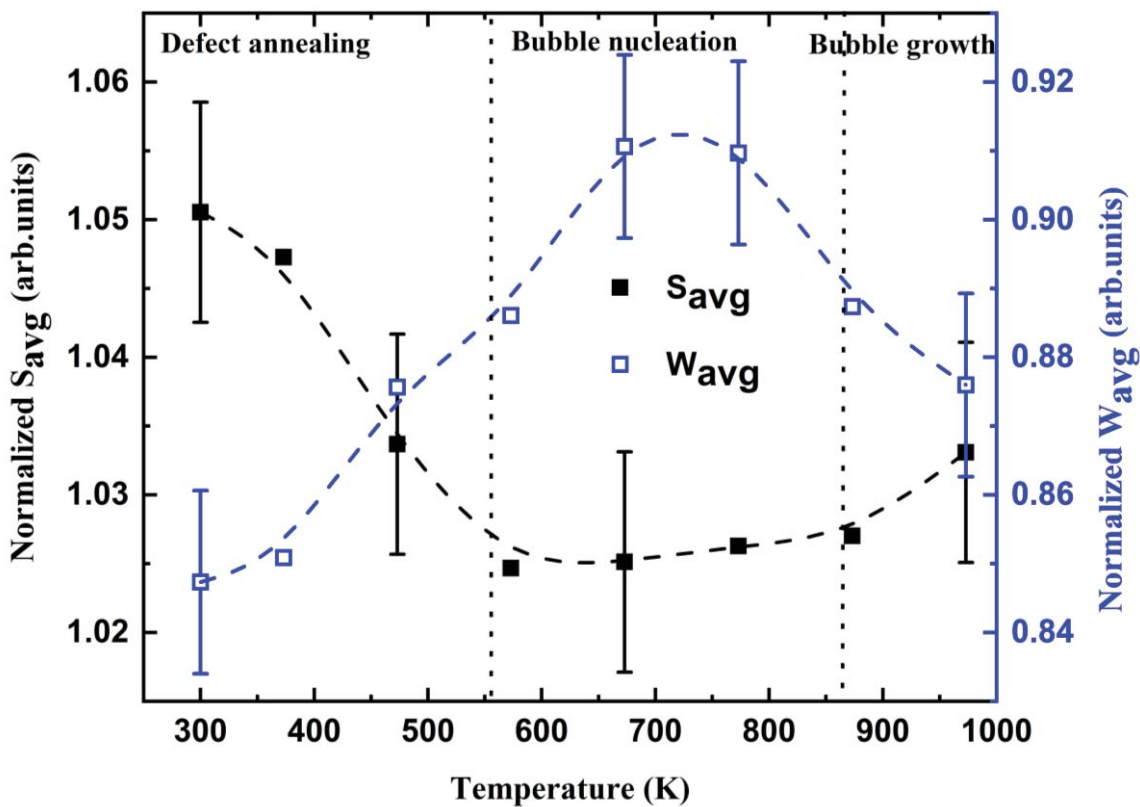


Figure 3.6 The average of normalized S and W parameters from the region 360 ± 150 nm of low-dose sample is plotted against the annealing temperature. The dashed lines through the data points are just a guide to the eye.

The He_mV_n complexes formed at 573 K can migrate due to high-temperature annealing and coalescence with adjacent complexes. Hence, the size of the He_mV_n complexes increases, whereas the number density decreases. This increase in size associated with a decrease in number density keeps the S_{avg} stable from 573 to 873 K. The W_{avg} stood stable from 673 to 773 K, which may be an indication of a stable m/n ratio in this temperature range. The annealing stage 573 to 873 K represents the bubble nucleation stage where the nucleation of embryos having a critical size and critical m/n ratio takes place. The increase in S_{avg} beyond 873 K is due to the growth of larger He_mV_n complexes with high vacancy content (low m/n ratio) or He bubbles. The He bubble growth mechanisms are of two types 1) migration and coalescence and 2) Ostwald ripening [46]. In migration and coalescence, the He_mV_n embryos migrate and coalesce with the nearby embryos, thereby decreasing their

number and increasing the size. But in the Ostwald ripening process, those embryos having a critical size can grow further by absorbing the vacancies released by the dissolution of embryos having size less than the critical size. The availability of thermal vacancies at a temperature above $0.45T_m$ also aids the bubble growth. The decrease in W_{avg} in this region is due to the decrease in core electron annihilation fraction due to the decrease in m/n ratio associated with the bubble growth.

3.3.2.3. Isochronal annealing study: High-dose sample

The normalized S-parameter vs. positron beam energy plots of high-dose sample are shown in figure 3.7. The S-parameter variations shown by the as-irradiated sample is discussed previously. An overall reduction in S-parameter with respect to the annealing temperature is observed from RT to 573 K. Then, a stable S-parameter curve is observed from 573 to 673 K followed by an increase in S-parameter at 773 K.

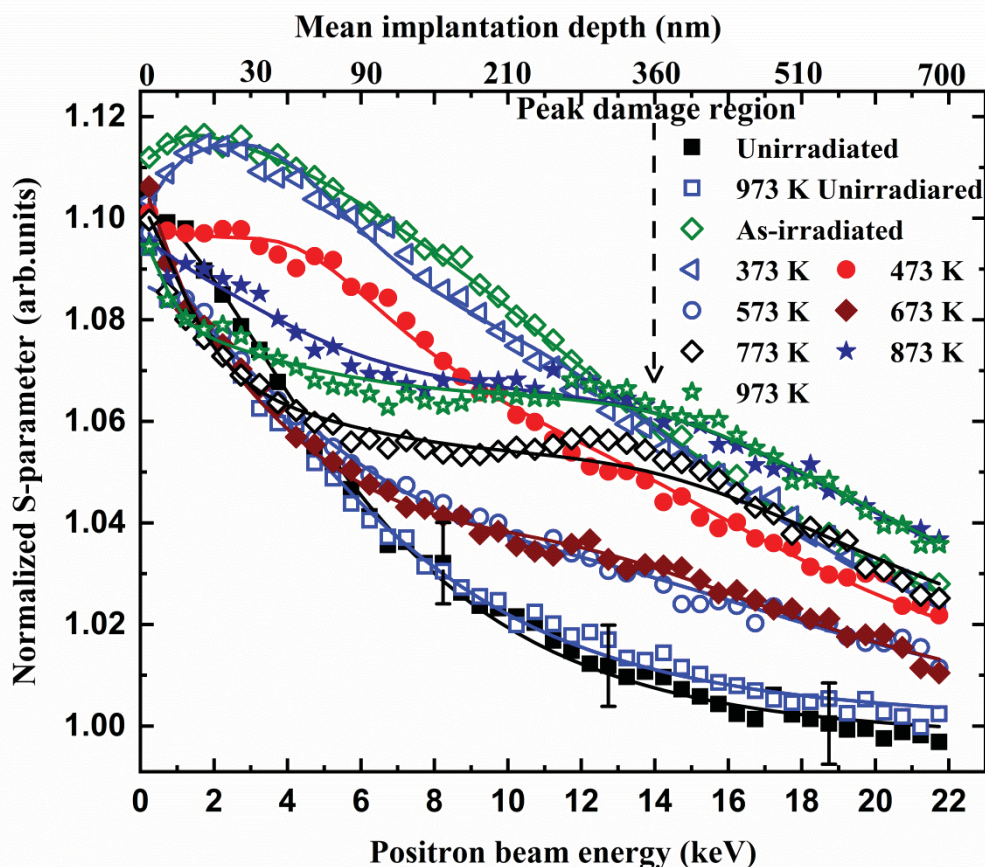


Figure 3.7 Normalized S-parameter vs. positron beam energy plots of the high-dose samples. Positron mean implantation depth is shown along the top x-axis. The data points were fitted using VEPFIT programme.

The near-surface S-parameter peak (at ~30 nm) observed in as-irradiated state completely disappears after annealing at 573 K. It has been reported that the vacancy clusters formed during low-temperature irradiation in α -Fe dissociate between the temperatures 500 to 600 K [161]. Hence, as the annealing temperature increases to 573 K, the bare vacancy clusters present in the near-surface region dissociate and/or redistributed in the inner layers with available helium towards forming He_mV_n complexes. The stable S-parameter region from 573 to 673 K represents the bubble nucleation stage and the increase in S-parameter at 773 K is due to the growth of helium bubbles.

Figure 3.8 shows the variation of average of normalized S-parameter (S_{avg}) and W-parameter (W_{avg}) around a depth region of 360 ± 150 nm as a function of temperature. The S_{avg} decreases with increase in annealing temperature from RT to 573 K, after which it remains stable up to 673 K. Beyond 673 K, the S_{avg} sharply increases up to 873 K. On the other hand, W_{avg} increases from RT to 673 K and decreases with further annealing from 673 to 873 K. The S_{avg} of the high-dose sample shows similar trend as in low-dose sample till 573 K, which shows that the same defect annealing mechanism is acting in both samples. The stable S_{avg} region corresponding to bubble nucleation is observed for a shorter temperature range (573 to 673 K) as compared to the low-dose sample (573 to 773 K). The W_{avg} shows a maximum at 673 K, which shows that clusters with higher m/n ratio are formed at 673 K. Further increase in S_{avg} associated with a decrease in W_{avg} from 673 to 873 K indicates the bubble growth. The early bubble growth in high-dose sample shows the dependency of irradiation dose on helium bubble evolution with temperature. The dependence of irradiation dose on the size and concentration of helium bubbles in metals is reported previously [74]. The S_{avg} and W_{avg} stood stable (within error bars) from 873 to 973 K due to the saturation in bubble growth.

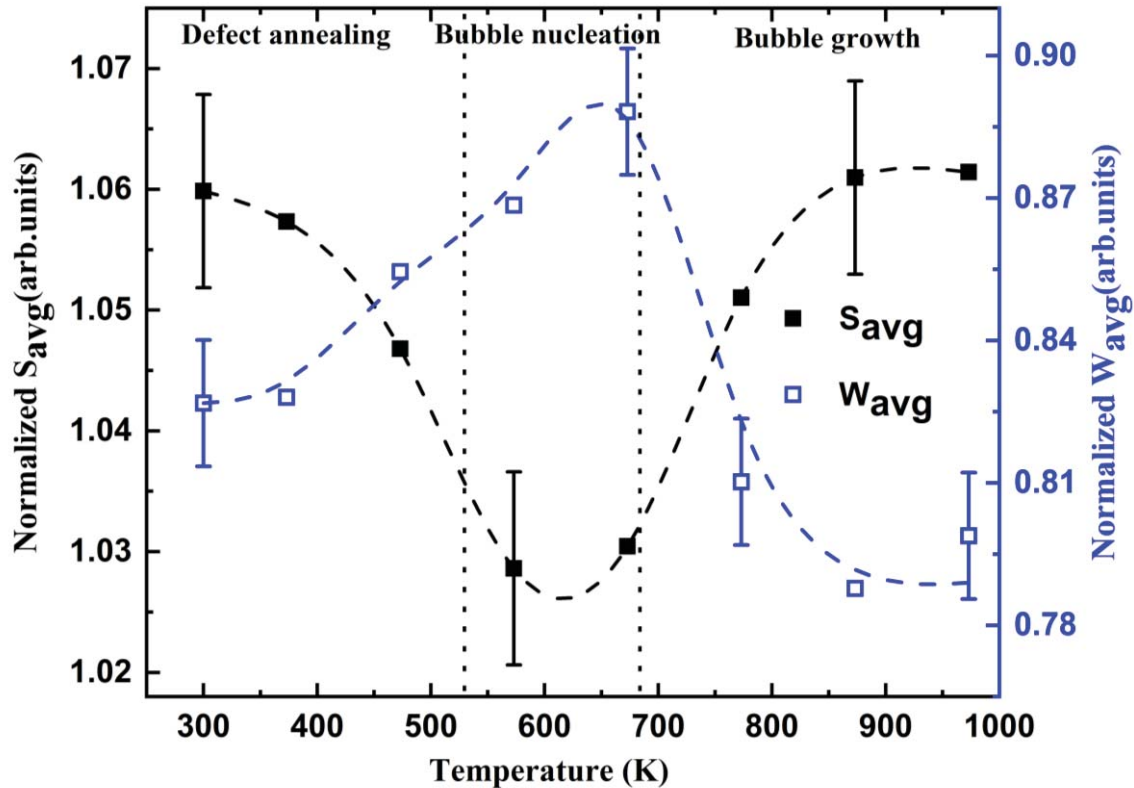


Figure 3.8 The average S and W parameters from the depth region 360 ± 150 nm of high-dose sample is plotted as a function of annealing temperature. S and W parameters were normalized with respect to the unirradiated bulk values. The dashed lines through the data points are just an aid to the eye.

3.3.2.4. Comparison between both the doses-VEPFIT analysis

The normalized S -parameter vs. positron beam energy plots were fitted using VEPFIT programme [145], and the results are shown in figure 3.9. The positron diffusion length and S -parameter of the unirradiated sample were deduced by giving a single layer fit. The unirradiated sample has a normalized S -parameter of 1.000 ± 0.008 and a diffusion length of 109 ± 3 nm. In the case of irradiated samples, various multiple layer fitting was attempted on experimental data, but three layer fitting had yielded lowest variance with meaningful physical parameters. Hence, a three-layer fit consisting of a surface layer, defected layer, and an unirradiated bulk is used for the irradiated samples. The S -parameter and positron diffusion length of the unirradiated bulk layer of the irradiated samples were fixed at 1 and 109 nm, respectively. The low-dose sample in as-irradiated state shows a narrow surface layer having a width of 38 ± 2 nm and a defected layer having an upper boundary at 503 ± 7 nm. The high-dose sample in the as-irradiated state shows a surface layer of width 72 ± 5 nm and a defected layer having an upper boundary at 502 ± 7 nm. The presence of surface layers in both samples is due to the clustering of vacancies at near-surface regions as well as due to

the presence of surface defects induced by irradiation. Since the surface layer doesn't show any systematic variations in the S-parameter or width of the layer with respect to the annealing temperature, it is excluded from further discussion.

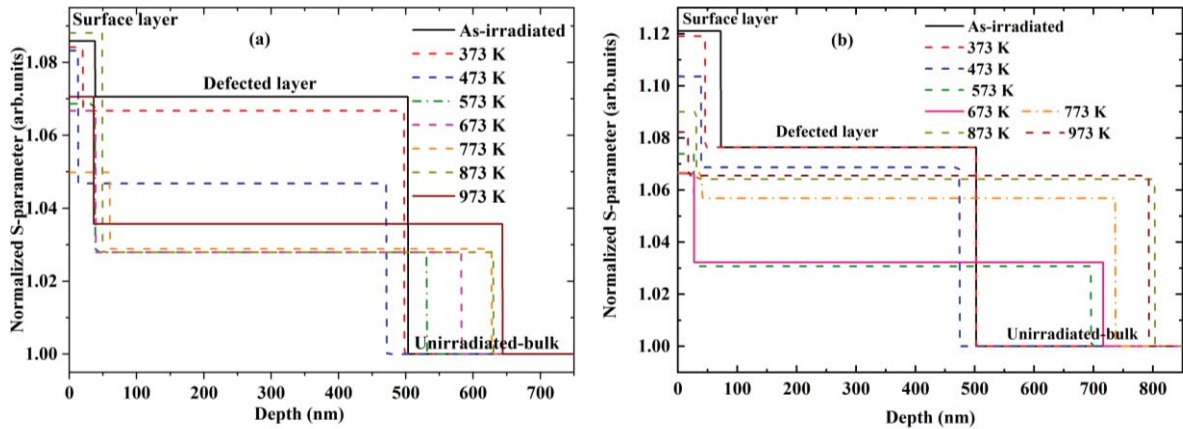


Figure 3.9 Normalized S-parameter vs. depth profile of (a) low-dose and (b) high-dose samples obtained from the VEPFIT analysis. Three-layer fit consists of a surface layer, defected layer, and an unirradiated bulk was used in the VEPFIT modelling.

Among irradiated samples, the VEPFIT analysis gives a higher positron diffusion length (83 nm) in the defected layer of low-dose sample, which is higher as compared to the positron diffusion length in high-dose sample (66 nm). This is due to the presence of lower concentration of irradiation-induced vacancy-type defects in low-dose sample as compared to high-dose sample. The VEPFIT deduced S-parameter and width of the defected layer of both doses (from figure 3.9) have been plotted against the temperature and shown in figure 3.10 and 3.11. The S-parameter variations with respect to temperature are similar to the variations of S_{avg} shown in figure 3.6 and 3.8.

As shown in figure 3.10, the S-parameter values shown by the defected layer of both samples follow a similar trend till 573 K, irrespective of the helium concentration and damage present in the samples. Hence, in helium-implanted samples, irrespective of the irradiation dose, similar defect annealing mechanism is acting during this temperature range. Both the doses show similar S-parameter from 473 to 673 K. As discussed earlier, the bubble nucleation stage was characterized by a stable S-parameter region from 573 to 673 K. This shows that during the bubble nucleation stage from 573 to 673 K; the He_mV_n embryos attain a critical size or critical m/n ratio irrespective of the dose. The similar and stable S-parameter observed between 573 to 673 K shows the presence of stable He_mV_n complexes in this temperature range. The thermal stability of a He_mV_n cluster depends on its m/n ratio. It has been reported that in α -Fe, the most stable configuration of He_mV_n complexes is having an

m/n ratio close to 1-1.5 [44, 163, 164]. This is because, When the m/n ratio is ~ 1 , the helium atoms occupy the vacant lattice sites and is coherent with the bcc- Fe matrix [164]. A rapid increase in S-parameter at 773 K in the high-dose sample arises due to the increase in average bubble size due to the helium bubble growth. The low-dose sample shows a delayed bubble growth, which occurs at 973 K.

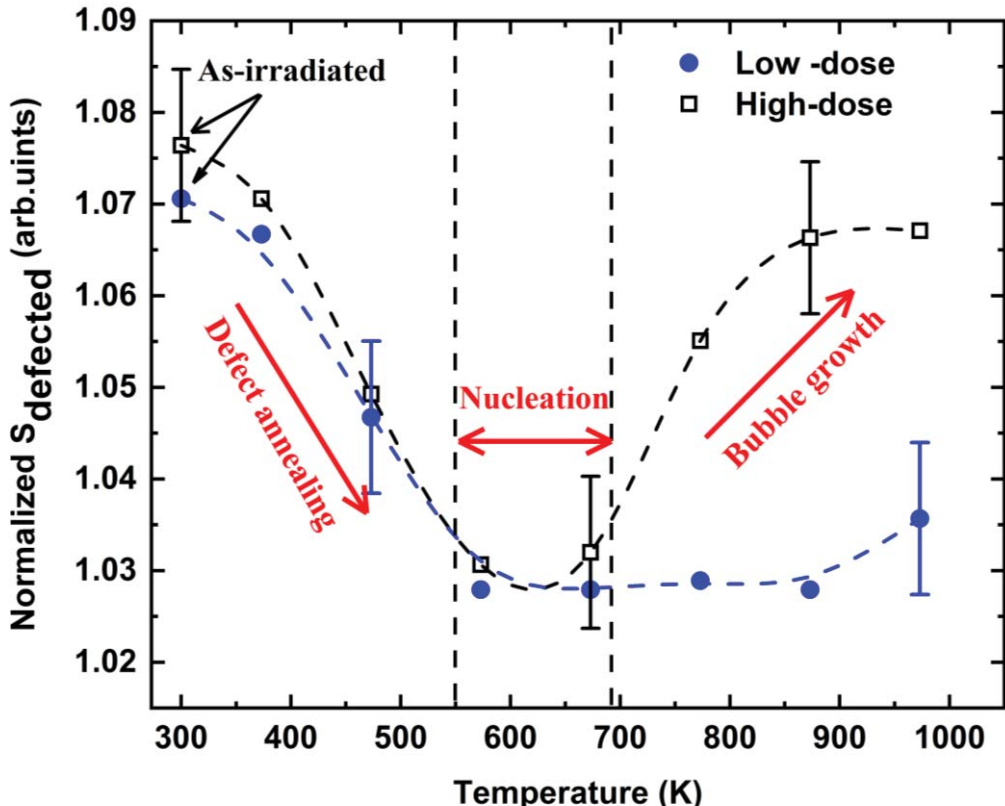


Figure 3.10 Normalized S-parameter of defected layer (deduced from VEPFIT analysis) for both doses as a function of annealing temperature is plotted for comparison.

As shown in figure 3.11, the width of defected layer of both samples increases with increase in temperature. A wider defected layer is observed in high-dose sample from 373 to 973 K as compared to low-dose sample. The irradiation profile predicted by SRIM (figure 3.1) shows that the helium concentration profile extends even beyond the vacancy distribution range. These helium atoms at the end of ion range are predominantly trapped in single vacancies as He-V pair. In α -Fe, as compared to the vacancy migration energy (0.65 eV), lower migration energies (0.28 to 0.33 eV) have been reported for smaller He_mV_n complexes [44]. Hence, the initial increase in irradiated layer width with temperature (figure 3.11) is mainly due to the migration of these bound helium atoms or vacancies towards both directions. A theoretical study done by Borodin et al. [165] shows that smaller He_mV_n

complexes with $n < 5$ and $n > m$ are mobile even at 573 K. The diffusion coefficient of these smaller complexes ($\sim 10^4 \text{ nm}^2 \text{ s}^{-1}$) is just 1-2 orders of magnitude lesser than that of mono-vacancies ($\sim 10^6 \text{ nm}^2 \text{ s}^{-1}$) at 573 K. Also, it has been reported that, at 573 K, He_mV_n complexes of the type He_2V_3 can migrate to a distance greater than 100 nm during its lifetime [166]. Another study by Luklinska et al. [62] also reported that the migration of smaller complexes of the type He_1V_2 at the early stages of helium bubble formation in ferritic steels can take place. Hence, the migration of the smaller He_mV_n complexes along with rapid migration of helium atoms which de-trapped from the He_mV_n complexes having high m/n ratio leads to the increase in irradiated layer width of high-dose sample till 873 K. A similar trend is observed in the low-dose sample also, but the variation of width with temperature is less which is due to the presence of lower concentration of migrating species. From 873 to 973 K, the observed variation in the broadening of irradiated layer (within the error bar) is less, which is due to the decreased migration of larger bubbles.

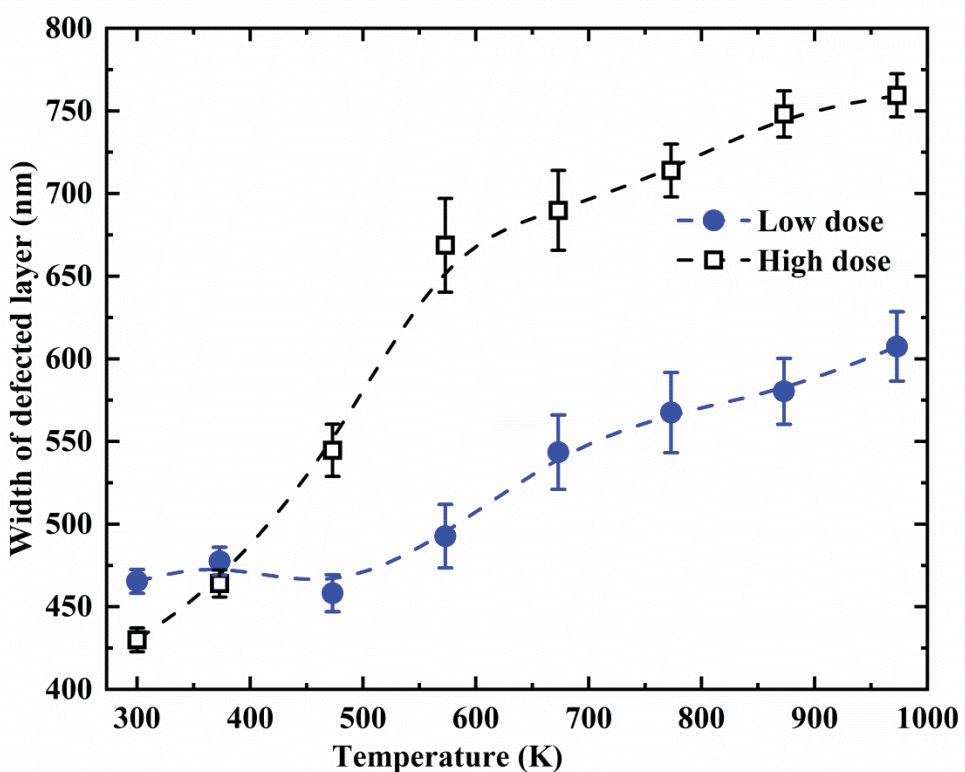


Figure 3.11 Variation of width of the irradiated layer (deduced from VEPFIT analysis) of both doses as a function of the annealing temperature.

3.3.2.5. S-W correlation plot

The S-W correlation plots using average of normalized S and W-parameters from the region 360 ± 150 for both doses are shown in figure 3.12. The S-W plot of low-dose sample shows a linear nature and does not show distinct regions of bubble evolution. This is because

of the lesser number of He_mV_n embryos that nucleated and grown due to the availability of lesser number of helium atoms and vacancies. High-dose sample (figure 3.8) shows stages corresponding to defect annealing, bubble nucleation, and bubble growth. Since each kind of defect is characterized by a single (S, W) couple, the S-W plot can be used to identify the nature of defects presented in the samples during different annealing stages. In high-dose sample, the defect annealing stage is characterized by the linear nature of S-W correlation plot from the as-irradiated to 573 K. The decrease in S_{avg} associated with an increase in W_{avg} in the defect annealing stage is due to the annealing of vacancies and gradual filling of helium into the vacancies or vacancy clusters. In the as-irradiated sample, vacancies and vacancy clusters having different sizes and He_mV_n complexes of different m/n ratio are present. At 573K, only He_mV_n complexes having similar m/n ratio are present in the sample. Hence, the defect annealing stage in the S-W correlation plot represents the transformation from mixed m/n ratio to a single m/n ratio. The defect annealing stage is followed by a bubble nucleation stage from 573 to 673 K, where the nucleation of He_mV_n embryos takes place. The annealing stage from 673 to 973 K falls in the bubble growth region, where growth of larger helium bubbles occurs.

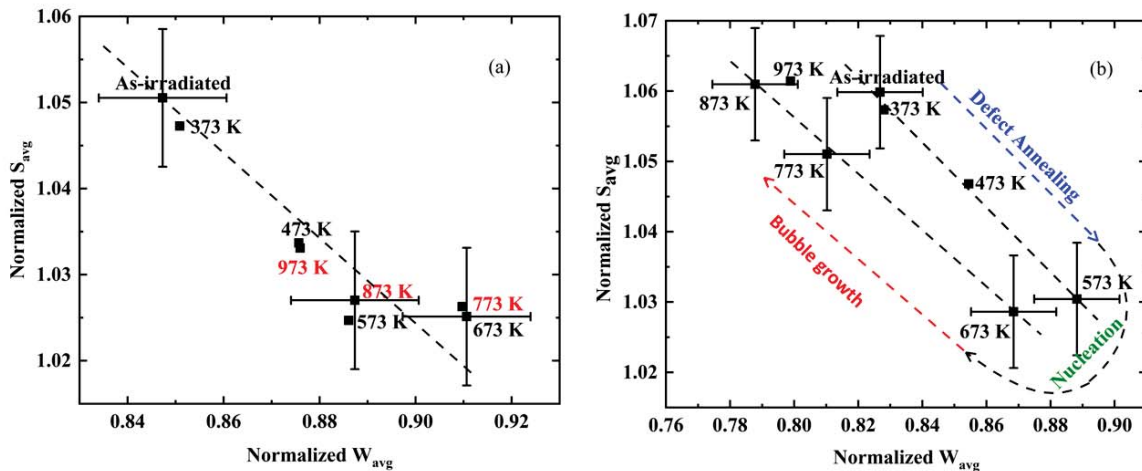


Figure 3.12 S-W correlation plots of (a) low-dose and (b) high-dose sample using average of normalized S and W-parameters from the region 360 ± 150 nm.

3.3.3. Transmission Electron Microscopy study

TEM study was carried out on the high-dose sample annealed at 773 K, and the result is shown in figure 3.13. The image was taken from a depth of around 1 μm from the surface. Helium bubbles having an average size of the order of 1.4 nm is observed in the TEM image. In the underfocus image, He bubbles appeared as white dots surrounded by a dark fringe,

whereas in overfocus image, it appeared as dark dots surrounded by a bright fringe. The images show a dense distribution of bubbles in the matrix.

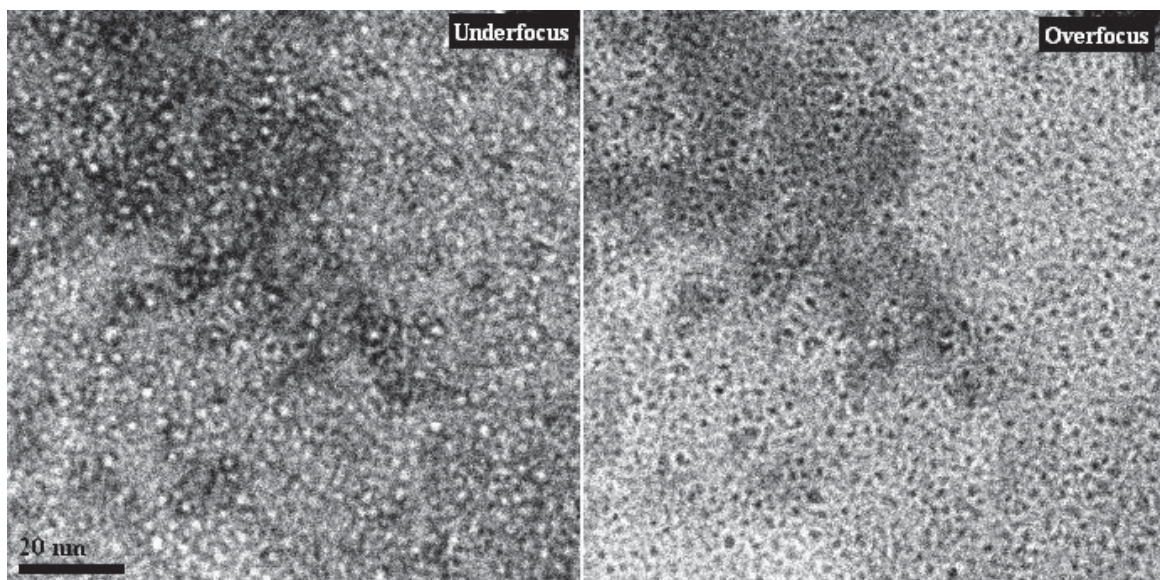


Figure 3.13 TEM images of the high-dose sample annealed at 773 K. Helium bubbles having an average size of around 1.4 nm are observed. The bubbles appear as white dots surrounded by a dark fringe in underfocus, and dark dots surrounded by a bright fringe in overfocus condition.

3.4. Summary

Effect of irradiation dose on the nucleation and growth of helium bubbles under isochronal annealing in Indian Reduced Activation Ferritic/Martensitic steel was studied. SIMS study showed a reduction in accumulated helium concentration with respect to annealing temperature due to thermal de-trapping of helium atoms from He_mV_n complexes. Depth distribution of irradiation-induced defects and different stages of helium bubble formation were studied using positron beam based Doppler broadening spectroscopy. Isochronal annealing study showed three different S-parameter stages corresponding to defect annealing, bubble nucleation, and bubble growth in both samples. Both low-dose and high-dose samples showed a defect annealing stage from as-irradiated state to 573 K due to the annealing of irradiation-induced vacancy-type defects. A stable minimum S-parameter is observed in both samples during bubble nucleation stage. During the bubble nucleation stage, irrespective of the irradiation dose, both the samples show the formation of smaller He_mV_n complexes with similar m/n ratio. An increase in S-parameter associated with helium bubble growth is observed in high-dose sample at 773 K whereas at 973 K in low-dose sample. Both doses showed a sharp increase in width of the defected layer at higher temperatures due to the

migration of smaller He_mV_n complexes as predicted by previous theoretical models. TEM studies on high-dose sample showed a dense distribution of bubbles having an average size $\sim 1.4 \text{ nm}$ in the matrix at 773 K.

Chapter 4

Effect of sequential irradiation of hydrogen and helium in RAFM steel

4.1. Introduction

Along with high displacement damage introduced by 14 MeV neutrons, core structural materials in fusion reactors are also exposed to helium and hydrogen at the rate of 10-15 appm He/dpa and 40-50 appm H/dpa [16, 167]. Even though the detrimental effect of hydrogen on microstructural and mechanical properties of materials is low, the ability of hydrogen to aid helium bubble growth in core-structural materials is a major concern [80, 168-174]. The binding of hydrogen and its isotopes to helium-associated defects is very strong as compared to other defects such as vacancies, interstitials and dislocations [66, 175, 176]. The enhanced growth of helium bubbles and dislocation loops due to the synergistic effect of hydrogen and helium in reactor steels has been studied previously [80, 168, 170, 172, 174, 177]. Though hydrogen assisted helium bubble growth and material degradation are reported previously, nature of interaction between hydrogen and helium, exact role of hydrogen in promoting nucleation and growth of helium-vacancy complexes are still lacking clarity. A major concern while using simultaneous or sequential multiple ion beam irradiations to study the synergistic effect of hydrogen and helium is the production of excess vacancies by hydrogen irradiation itself. The enhancement in growth of helium bubbles or void swelling observed in multiple ion beam irradiation studies could be attributed to these excess vacancies. The potential of positron annihilation spectroscopy to probe open-volume defects with high sensitivity enables the non-destructive investigation of hydrogen and helium associated defects in materials. The presence of helium or hydrogen associated with a vacancy can change the fraction of positrons that annihilate with the valence and core electrons. Hence, the change in valence or core annihilation fraction of positrons due to the formation of H-vacancy or He-vacancy or H-He-vacancy complexes will be reflected in the positron annihilation line-shape parameters. In this chapter, individual ion beam irradiations have been performed with hydrogen and helium ions to study the formation and growth of hydrogen-vacancy and helium-vacancy complexes. Further, sequential ion beam irradiations have been performed using both hydrogen and helium ions to study the formation of H-He-vacancy complexes and their influence on the nucleation and growth of helium bubbles. This

work aims to study various stages of formation and restructuring of defect-complexes associated with hydrogen and helium, which influence the growth of helium bubbles.

4.2. Experimental

Four normalized and tempered INRAFM steel samples were prepared for irradiation. Irradiations were performed with 80 keV hydrogen ions to a dose of 1500 appm (1.8×10^{15} ions/cm²), and 130 keV helium ions to a dose of 450 appm (6.75×10^{14} ions/cm²). Out of four samples, one sample is irradiated with hydrogen, and a second sample is irradiated with helium ions. A third sample is irradiated with hydrogen ions first and then with helium ions (denoted as H+He). Then, the fourth sample is irradiated with helium ions first and then with hydrogen ions (denoted as He+H). All four irradiations were carried out at room temperature. The irradiations were done with the above doses so that the concentration of ions is approximately equal to the total accumulated H and He gases per year in fusion reactor first-wall and blanket materials.

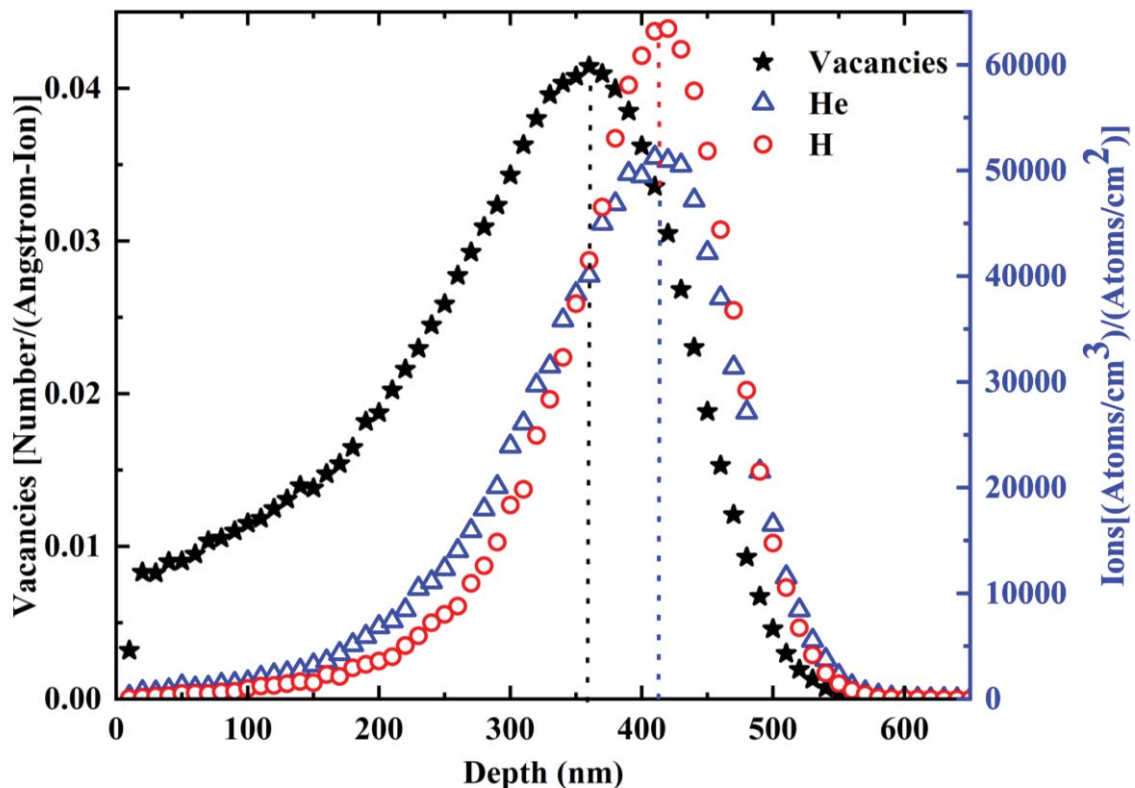


Figure 4.1 Distribution of total vacancies and ions into INRAFM steel calculated using SRIM 2013 code. Vacancy and ion peaks are shown using dotted lines.

Figure 4.1 shows the distribution of vacancies and ions into the material calculated using SRIM 2013 code [142]. The energies of individual ions have been chosen such that their peak distribution occurs at the same depth. Both He and H ions peaks have been around

410 nm, whereas the vacancy peak occurs around 360 nm. The individual peak damage induced by H and He ions is 0.007 dpa and 0.030 dpa respectively, and the total damage produced by the sequential irradiation is 0.037 dpa. An isochronal annealing study has been performed on the irradiated samples from RT to 973 K with 1 h holding time on each annealing step under a dynamic vacuum of 2×10^{-6} mbar. The irradiated samples were characterized using positron beam based Doppler broadening spectroscopy.

4.3. Results and discussion

4.3.1. Defect studies in as-irradiated samples

Figure 4.2 shows the normalized S-parameter vs. positron beam energy plots of unirradiated and as-irradiated samples. A higher S-parameter is observed in all irradiated samples due to the presence of irradiation-induced open-volume defects. Hydrogen irradiation induces defects such as vacancies (V), vacancy clusters (V_n), and H-vacancy complexes of the type $H_m V_n$ where m and n are the number of H atoms and vacancies associated with each defect-complex. The high S-parameter observed in H-irradiated sample as compared to unirradiated sample is due to the presence of vacancy-type defects and $H_m V_n$ complexes with high vacancy content. Similarly, in helium irradiated sample, irradiation-induced vacancy-type defects and $He_m V_n$ complexes with high vacancy content are responsible for high S-parameter as compared to the unirradiated sample. Among the single ion irradiated samples, He-irradiated sample shows a higher S-parameter as compared to the H-irradiated sample. This is because of the high displacement damage induced by He-irradiation (0.03 dpa) as compared to H-irradiation (0.007 dpa). The number and size of vacancy-type defects and defect-complexes present in He-irradiated sample is high as compared to the H-irradiated sample. The binding and migration energies of these defect-complexes depend on their configuration, size and number of H/He atoms or vacancies associated with each defect-complex [54, 163, 165, 169, 178, 179].

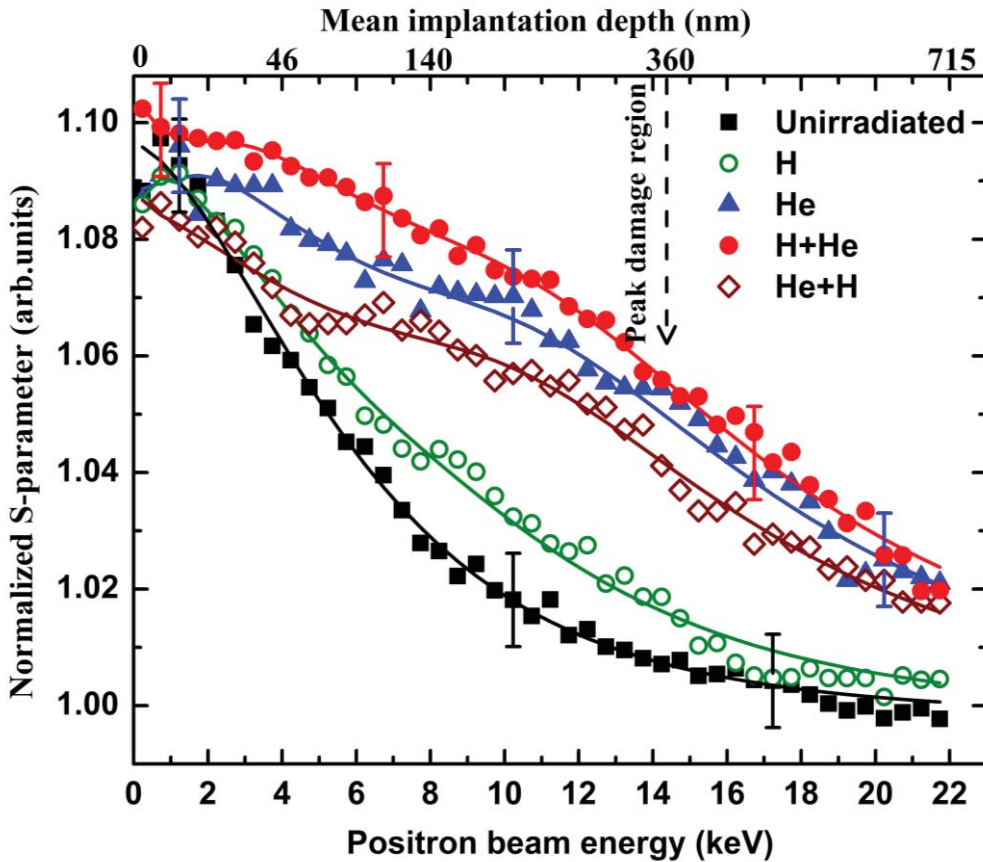


Figure 4.2 Normalized S -parameter vs. positron beam energy plots of the unirradiated and as-irradiated samples. The data points were fitted using VEPFIT programme. Typical error bars are shown at selected data points.

Both sequential irradiated samples contain an equal amount of displacement damage, irrespective of the sequence of irradiation. The change in irradiation sequence does not change the total number of vacancies produced. Hence, similar S -parameter values are expected in both sequential irradiated samples. Also, both the sequential irradiated samples are expected to show higher S -parameter values as compared to the single ion irradiated samples due to higher displacement damage present in the former. But the S -parameter of irradiated samples shows an overall trend as follows: $S_{H+He} > S_{He} > S_{He+H} > S_H$. The $H+He$ sample shows higher S -parameter as compared to all other samples due to higher displacement damage present in the former. But surprisingly, the $He+H$ sample shows S -parameter values lower than the $H+He$ and He samples. If the total accumulated dose or dpa are the only factors that decide S -parameter values, then both the $H+He$ and $He+H$ irradiated samples should show similar S -parameter values, and these S -parameter values should be higher as compared to the H and He irradiated samples. In the $He+H$ sample, the sample was initially irradiated with He ions which produce vacancy-type and He -vacancy complexes (of

the type He_mV_n) as defects. During subsequent irradiation with H ions, three major processes that can happen are i) production of additional vacancies and H-vacancy complexes, ii) the low migration energy (~ 0.01 eV) of H in α -Fe matrix [169] permits easy migration and trapping of H in vacancy-type defects that are already induced by He-irradiation and saturate them and iii) interaction of H with already existing He-vacancy complexes and form H-He-vacancy complexes. The first process increases the S-parameter, whereas the other two processes reduce the S-parameter in the He+H-irradiated sample as compared to the He-irradiated sample. Reduction in S-parameter due to reason (ii) is valid only if the number of vacancy-type defects that are produced by H-irradiation is less as compared to the number of He-induced vacancy-type defects that are saturated by H atoms. It has been reported that the formation of H-He-vacancy complexes can be due to the binding of H atoms to the walls of an already existing He-vacancy complex (of the type He_mV_n) via a mechanism similar to chemisorption [180] or the attraction of H atoms towards the He-vacancy complexes due to the stress field which exists around the He-vacancy complexes [175]. Hydrogen isotope like deuterium can bind to helium bubbles with higher binding energy (0.78 ± 0.08 eV) as compared to its binding to vacancies (0.53 ± 0.07 eV) [176]. A recent density functional theory calculation shows that in α -Fe, He_1V_1 complex is an efficient trap for H atoms as compared to a monovacancy [181]. The dissolution of H in He_1V_1 complex is exothermic in nature with dissolution energy of -0.40 eV [181]. Also, since H in metals always prefers to occupy low charge density regions [182], a low charge density isosurface provided by He-vacancy complexes is an energetically favourable site for H to occupy [181]. It has also been reported that a single He_1V_1 complex in α -Fe can trap up to eight H atoms [181]. The presence of H in H-He-vacancy complex increases the probability of positrons to annihilate with core electrons as compared to the He-vacancy complexes. This reduces the S-parameter of He+H sample as compared to the He-irradiated sample. In the case of H+He sample, vacancies produced by pre-irradiation with H can trap those H atoms and form H-vacancy complexes. Hence the vacancies produced by subsequent irradiation with He will not be saturated by hydrogen trapping. Also, since the H atoms interact with already existing He-vacancy complexes to form H-He-vacancy complexes [175, 180], the probability for the formation of H-He-vacancy complexes in H+He sample is low due to the absence of pre-existing He-vacancy complexes during H-irradiation.

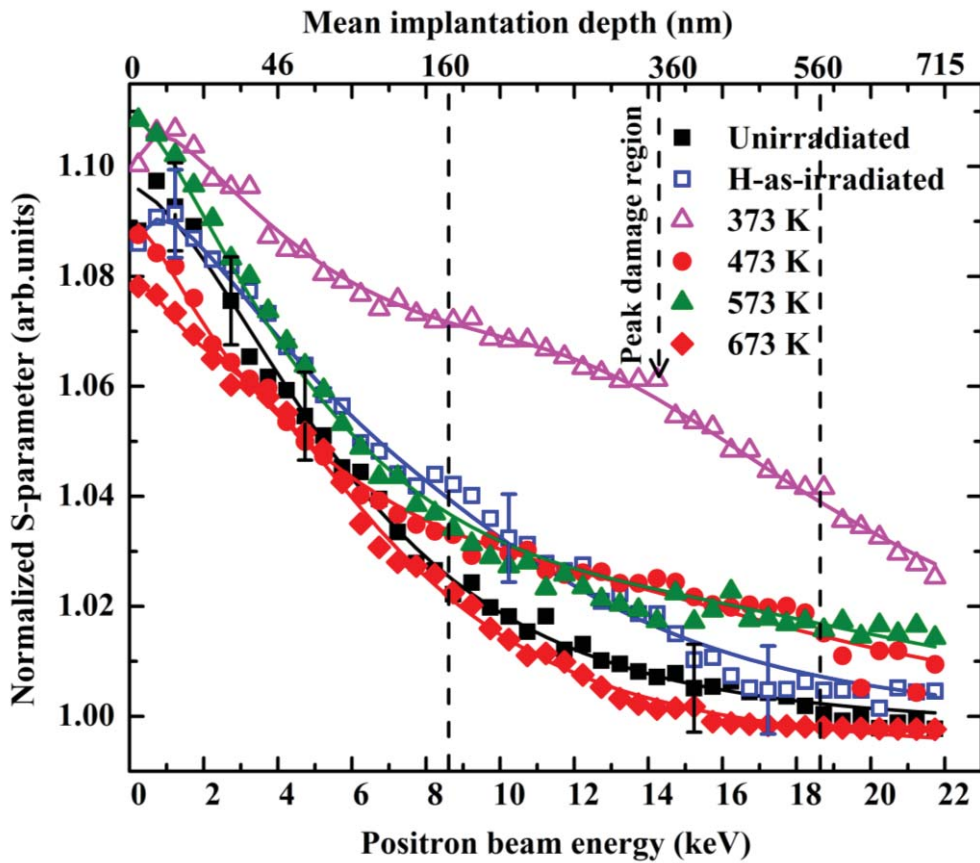


Figure 4.3 Variation of normalized S-parameter vs. positron beam energy curves of H-irradiated samples under isochronal annealing. The data points were fitted using VEPFIT programme.

4.3.2. Isochronal annealing studies

4.3.2.1. S-parameter vs. positron beam energy plots

Figure 4.3 shows the variation of S-parameter vs. positron beam energy curves of H-irradiated sample under isochronal annealing. The S-parameter increases at 373 K followed by a decrease with further annealing to 673 K. Since H-irradiation is associated with the injection of large number of H ions (1500 appm) associated with very low displacement damage (0.007 dpa); the as-irradiated sample contains H_mV_n complexes having high H/V ratio. Since the irradiation is performed at room temperature with low displacement damage, the defect-complexes are associated with mono-vacancies or smaller vacancy clusters. Since the de-trapping energy of H atoms from H_mV_n complexes in α -Fe matrix is low (<1 eV) [53, 76, 169, 183], the post-irradiation annealing at elevated temperatures leads to the release of H from those complexes [76]. The H-irradiated sample shows a sudden increase in S-parameter at 373 K due to the release of H from H_mV_n complexes having high H/V ratio. The release of H from H_mV_n complexes increases their trapping efficiency to positrons and hence, the S-parameter increases. Hence, as compared to the as-irradiated state, the H/V ratio associated

with the H_mV_n complexes decreases after annealing at 373 K. Further increase in annealing temperature decreases the S-parameter due to the release of H due to the dissociation of H_mV_n complexes and the annihilation of vacancies at the sinks. The complete defect recovery occurs in H-irradiated sample at 673 K. It has been observed that in the absence of H or He, the complete defect recovery of vacancy-type defects induced by irradiation in INRAFM steel occurs under isochronal annealing at 673 K [184]. Hence, the release of H from H_mV_n complexes causes the vacancies to anneal out at 673 K.

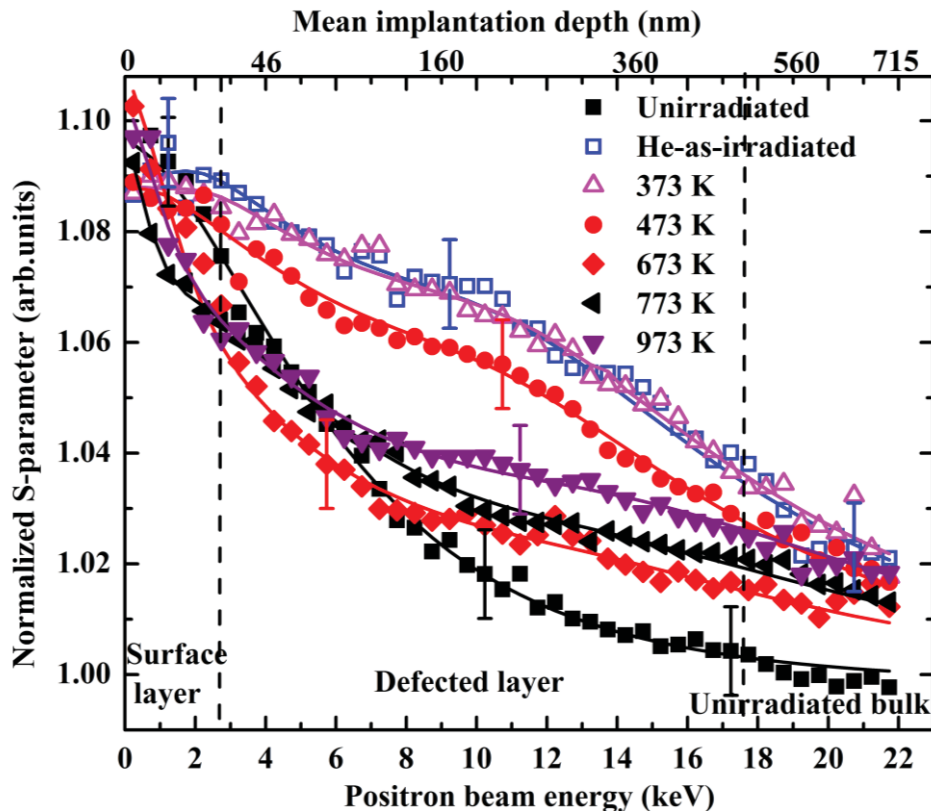


Figure 4.4 Variation of normalized S-parameter vs. positron beam energy curves of He-irradiated samples under isochronal annealing. The S-parameter values were normalized with respect to the unirradiated bulk value. Some of the plots were omitted from the figure for better visual clarity.

Figure 4.4 shows the variation of normalized S-parameter vs. positron beam energy plots of He-irradiated sample under isochronal annealing. The variations observed in S-parameter is similar to the results obtained in chapter 3. The sample doesn't show any variation in S-parameter at 373 K. An overall reduction in S-parameter is observed till 673 K, followed by an increase at 773 K in the near-surface regions (<10 keV). The decrease in S-parameter with annealing till 673 K is associated with the filling of He into vacancies or vacancy clusters, thereby forming H_mV_n complexes. At 773 K, the increase in S-parameter

in the near-surface region occurs due to the growth of larger He_mV_n complexes or bubbles. At high temperatures, He_mV_n complexes and those He atoms de-trapped from the complexes migrates towards the near-surface regions. This increase in concentration of He promotes the growth of bubbles in the near-surface regions. A nominal increase in S-parameter is observed in the regions where the positron energy is higher than 10 keV. At 973 K, an overall increase in S-parameter is observed due to the growth of He bubbles.

The results of the isochronal annealing study performed on the sequential irradiated samples are shown in figure 4.5. The S-parameter variations with respect to the annealing temperature shown by H+He sample (figure 4.5a) are almost similar to the He-irradiated sample. The S-parameter does not vary between as-irradiated state to 373 K. Then, the S-parameter decreases with increase in temperature till 673 K after which it increases from 773 to 973 K due to the growth of He bubbles. For the He+H sample (figure 4.5b), the initial increase in S-parameter at 373 K is due to the release of hydrogen from H-vacancy or H-He-vacancy complexes. The S-parameter then decreases with temperature from 373 to 673 K, and increases with further annealing from 773 to 973 K. The decrease in S-parameter with annealing till 673 K is due to the annealing of vacancies and vacancy clusters associated with the formation of H/He-vacancy defect-complexes, and increase in S-parameter observed from 773 to 973 K is due to the growth of helium bubbles.

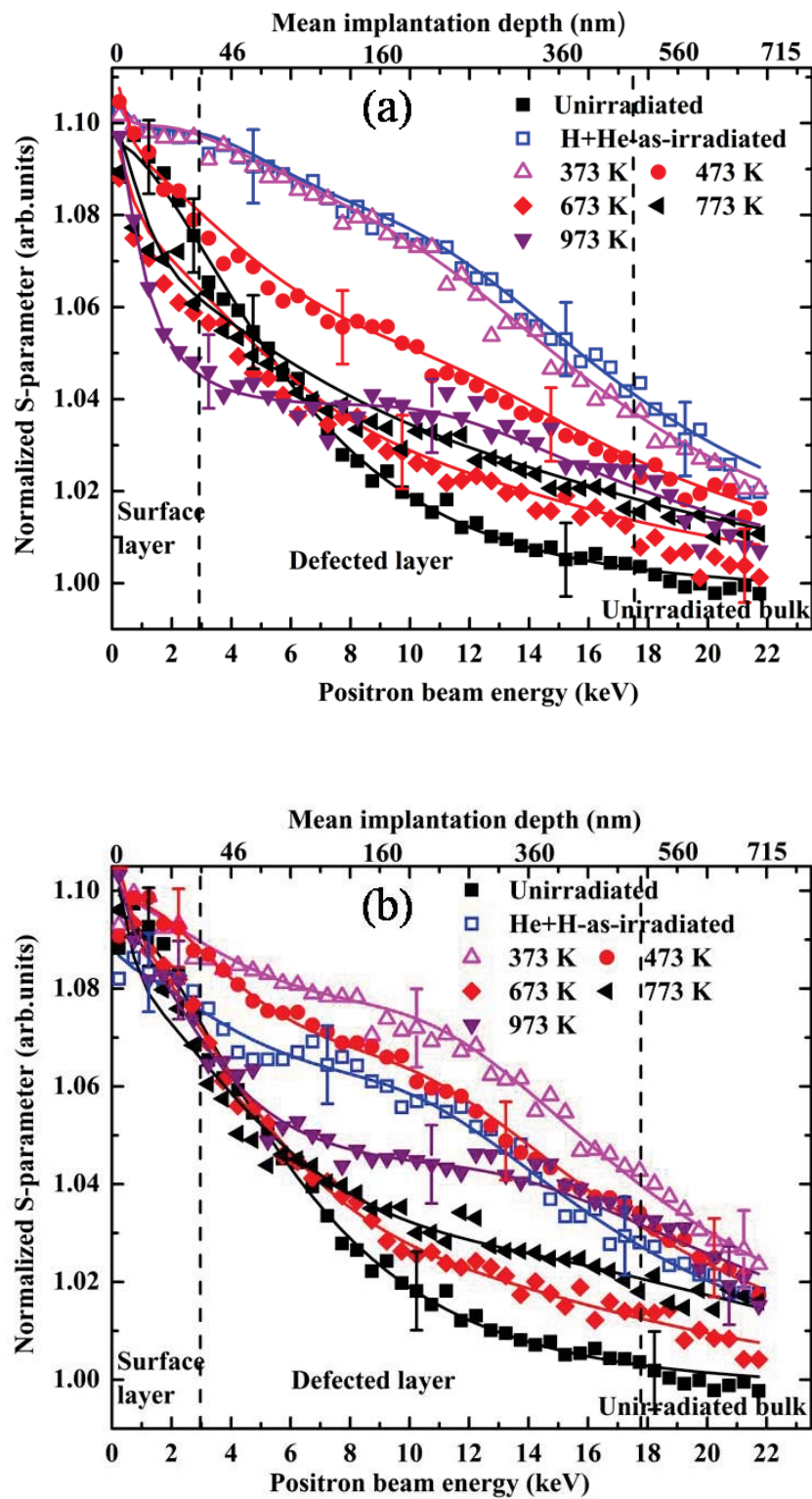


Figure 4.5 Variation of normalized S-parameter vs. positron beam energy curves of a) H+He-irradiated and b) He+H-irradiated samples under isochronal annealing. The S-parameter values were normalized with respect to the unirradiated bulk value.

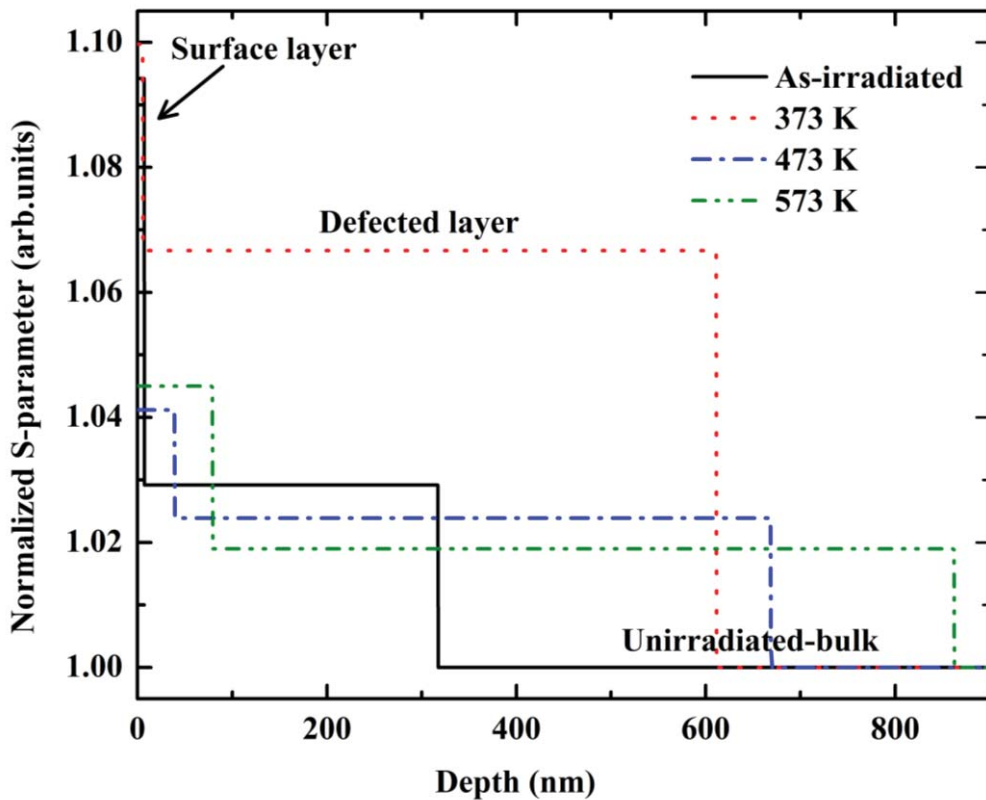


Figure 4.6 Normalized S-parameter vs. depth plot of H-irradiated sample deduced from VEPFIT analysis.

4.3.2.2. VEPFIT Analysis

The S-parameter vs. positron beam energy curves of all the as-irradiated and annealed samples were analyzed using VEPFIT programme [145]. Irradiated samples were fitted with three layers- a surface layer, defected layer and an unirradiated bulk layer. The S-parameter and diffusion length values obtained by giving a single layer fit to the unirradiated sample are fixed in the unirradiated bulk layer of the irradiated samples. The S vs. depth plots obtained using VEPFIT analysis are shown in figures 4.6 to 4.8. The H-irradiated sample shows a narrow surface layer of width 7 ± 3 nm and a defected layer that extend up to 317 ± 15 nm (figure 4.6). Since the narrow surface layer shown by the irradiated samples does not possess any physical significance; it is neglected for further discussion. Since the binding energy of H_mV_n complexes are low [169], thermal annealing at elevated temperatures leads to their dissociation. The low migration energies of H (~ 0.01 eV) [169] and vacancies (0.65 eV) [44] in α -Fe enable the fast migration of released H atoms and vacancies towards both directions from the defected layer. Also, some of the H_mV_n complexes are having low migration energy (H_mV_3 , migration energy ~ 0.25 eV) [53] and are able to migrate longer distances without dissociation. Those H atoms that migrate towards the surface may leave the material. Hence,

the rapid increase in upper boundary of defected layer observed from RT to 573 K is due to the migration of de-trapped hydrogen or vacancies or smaller $H_m V_n$ complexes.

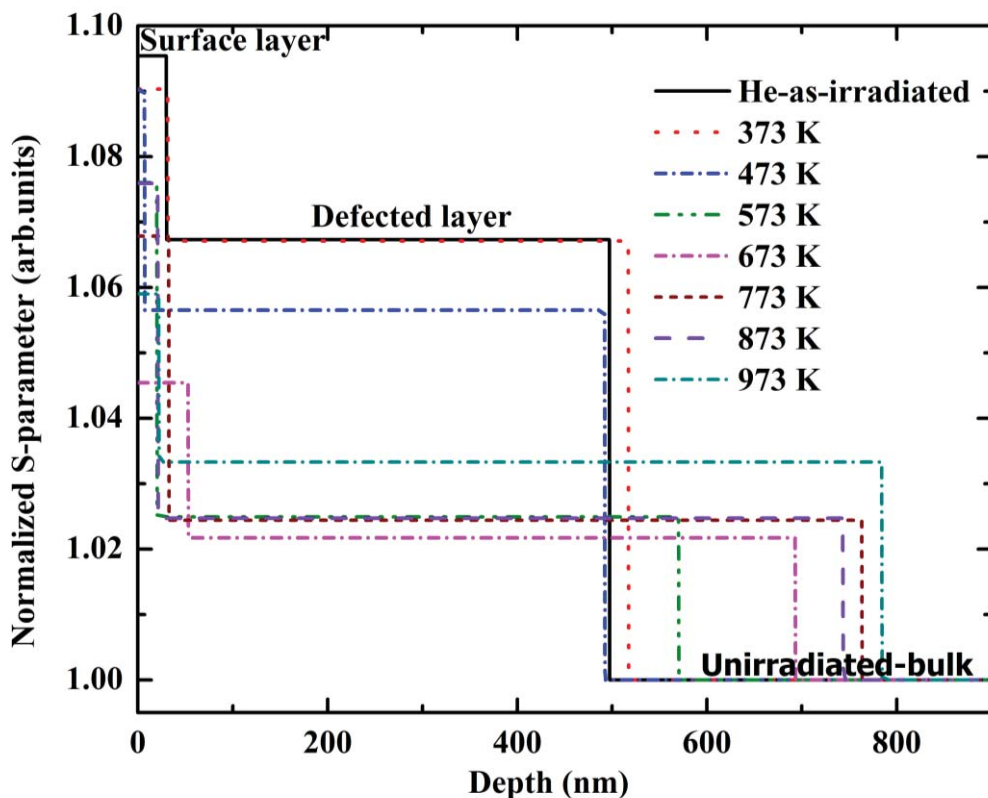


Figure 4.7 Normalized S-parameter vs. depth plot of He-irradiated sample deduced from VEPFIT analysis.

He-irradiated sample shows an almost stable upper boundary for the damaged layer from RT to 473 K (figure 4.7) followed by a fast increase with further annealing from 473 to 773 K. As discussed in chapter-3, the fast migration of vacancies, de-trapped He atoms and smaller $H_m V_n$ complexes increases the width of defected layer at higher temperatures. Then, the upper boundary of damaged layer remains almost stable from 773 to 973 K due to the decreased migration of larger helium bubbles. The sequentially irradiated samples (figure 4.8) are also showing a more or less similar trend like He-irradiated samples due to the migration of smaller defect-complexes or de-trapped H or He atoms or vacancies.

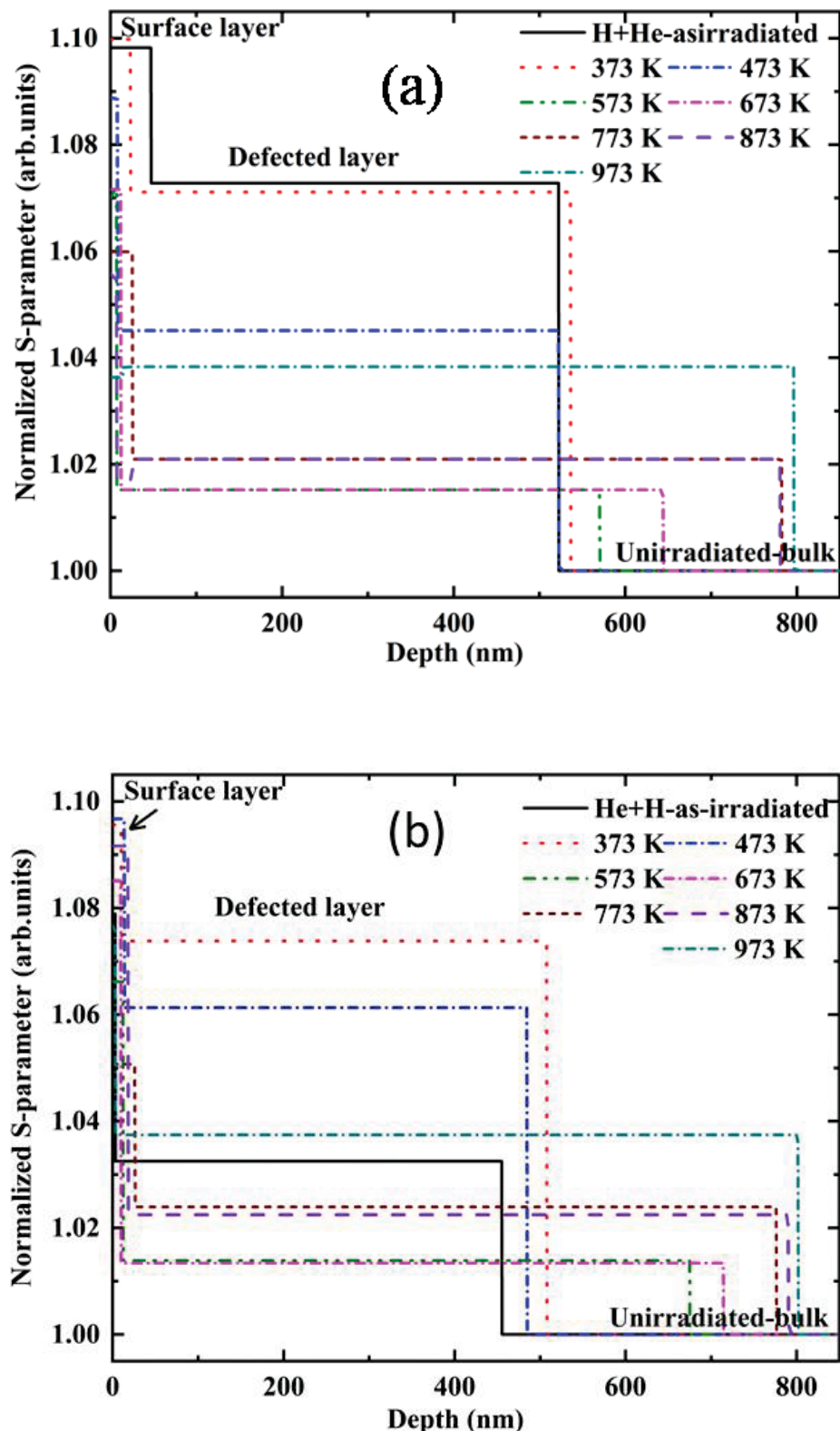


Figure 4.8 Normalized S-parameter vs. depth plot of a) H+He-irradiated and b) He+H-irradiated samples deduced from VEPFIT analysis.

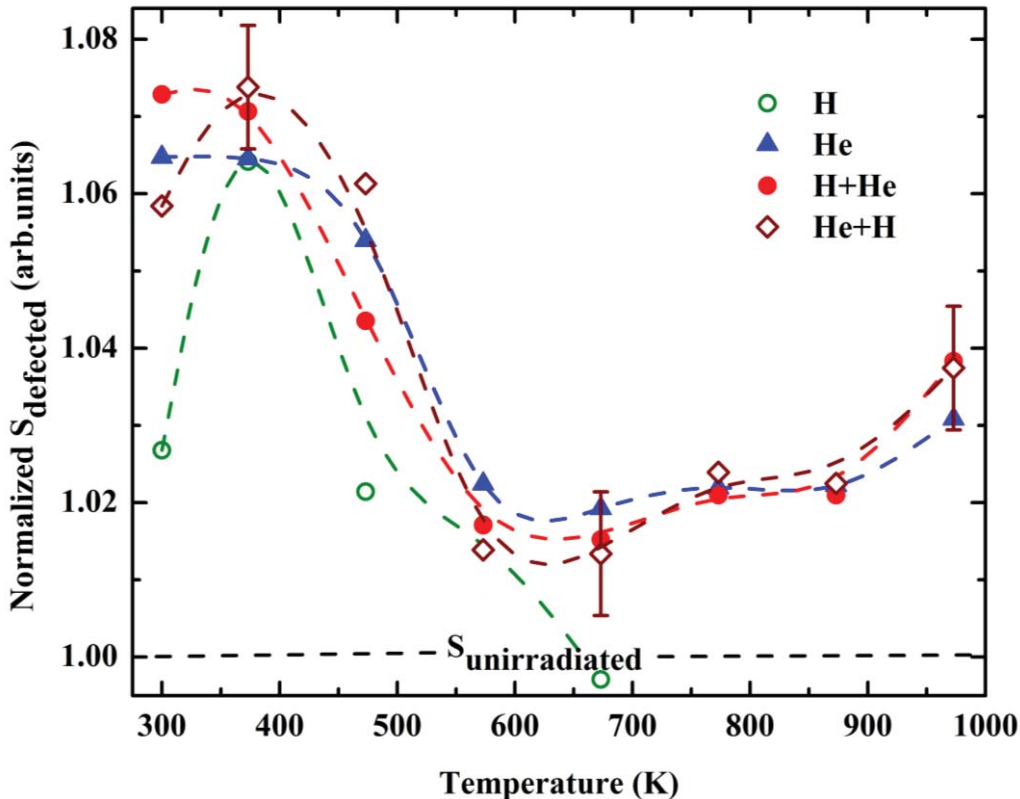


Figure 4.9 Variation of normalized S -parameter of defected region of irradiated samples deduced from VEPFIT analysis against the annealing temperature.

4.3.2.3. S_{defected} vs. Temperature plots

For better clarity of the results and to describe the changes occurring around the peak damage region, the S -parameter of the defected region obtained from VEPFIT analysis (Figures 4.6 to 4.8) is plotted as a function of annealing temperature and shown in figure 4.9. As discussed previously, H-irradiated sample shows an increase in S_{defected} from RT to 373 K, which is due to the release of H from H_mV_n complexes having high H/V ratio. Further annealing decreases the S_{defected} , and complete defect annealing occurs at 673 K. He-irradiated sample shows a decreasing trend in S_{defected} from RT to 573 K due to the annealing of vacancies and an increase in He/V ratio associated with the formation of smaller He_mV_n complexes. A stable minimum S_{defected} characterizes the bubble nucleation stage from 573 to 673 K, followed by an increase in S_{defected} from 773 to 973 K due to He bubble growth, as already observed in chapter 3.

The H+He sample also shows a trend similar to He-irradiated sample in the S_{defected} vs. temperature plot till 573 K. But from 473 to 573 K, the H+He sample shows a lower S_{defected} as compared to the He-irradiated sample. Though H+He sample has a low probability to form H-He-vacancy complexes in the as-irradiated state, the H atoms released from H_mV_n

complexes during annealing can migrate faster and interact with already existing He_mV_n complexes in the sample and form H-He-vacancy complexes. Due to this, S_{defected} of H+He sample is lower than He-irradiated sample from 473 to 673 K. In the case of He+H sample, S_{defected} shows an increasing trend similar to H-irradiated sample with annealing from RT to 373 K; which is due to the release of H from H-vacancy or H-He-vacancy complexes. Further annealing from 373 to 673 K decreases the S_{defected} similar to He-irradiated sample. A theoretical calculation by Hayward et al. [185] shown that the most tightly bound H atoms to a H-He-vacancy complex of the type $\text{H}_m\text{He}_n\text{V}_j$ is having binding energy less than 1 eV, whereas the weakly bound He atoms having binding energy more than 1.5 eV. Hence, as compared to He, dissociation of H from the defect-complexes can occur at early stages of annealing, which leads to an increase in S_{defected} at 373 K. From 573 to 673 K, H+He and He+H samples show a S_{defected} value lower than that of He-irradiated sample, which is due to the presence of H-He-vacancy complexes in the former. As the temperature increases above 673 K, the S_{defected} of both sequentially irradiated samples shows variations similar to He-irradiated sample. The S_{defected} variations that observed between different irradiated samples in figure 4.9 during the nucleation and growth stages of defect-complexes are less significant since the irradiations were performed at very low doses. In this study, at this irradiation conditions, even though the nature of defect-complexes present in the as-irradiated samples are different, the presence of H doesn't seem to influence the growth of He bubbles under isochronal annealing.

4.3.2.4. S-W correlation plot

The S-W correlation plots of unirradiated and irradiated samples are plotted using the average S and W-parameters around the peak damage region 360 ± 200 nm, and shown in figure 4.10. The region (160-560 nm) from which the average S-parameter has been calculated is shown using dotted lines in figure 4.3 to 4.6. Such a wide region has been chosen due to the migration of defects/defect-complexes towards both sides of the peak damage region at high temperatures. The lower boundary (160 nm) has been chosen to avoid the surface-proximity effects at low-positron-energies, and the upper boundary (560 nm) has been chosen to avoid the effect of unirradiated bulk at higher positron energies. Also, as the annealing temperature increases, almost a stable S-parameter is observed in this region due to the uniform distribution of defects. The S-W correlation plot of H-irradiated sample shows a linear nature from RT to 673 K. The H_mV_n complexes formed during irradiation are dissociated with annealing temperature, and no other higher order defects or defect-

complexes are formed. The samples containing helium shows two regions corresponding to the defect annealing stage, and nucleation and growth of larger He_mV_n clusters or bubbles. The defect annealing stage in helium containing samples was characterized by a linear region whereas the agglomeration of points at the middle of S-W plot is due to the nucleation and growth of helium bubbles.

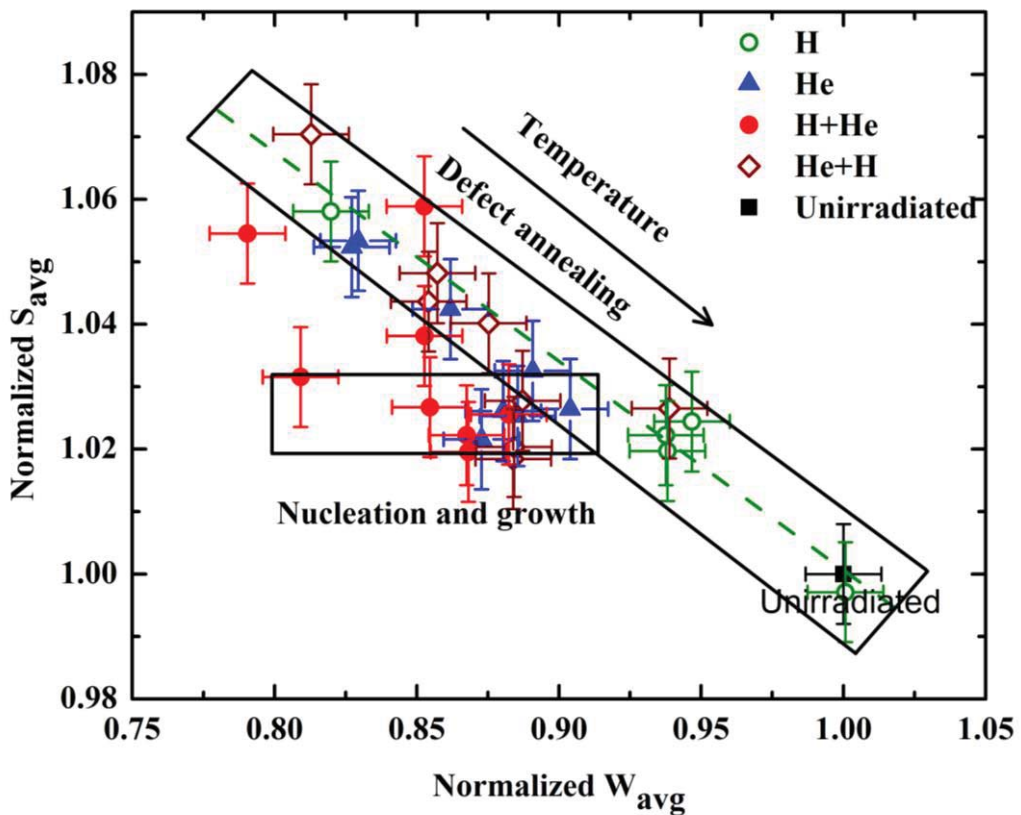


Figure 4.10 S-W correlation plot using the average of normalized S and W-parameters.

4.4. Conclusion

Formation and thermal evolution of defect-complexes induced by single and sequential irradiation of hydrogen and helium ions in INRAFM steel have been studied. Hydrogen irradiated sample showed an increase in S-parameter due to the release of hydrogen from H-vacancy complexes at 373 K, and a reduction in S-parameter with further annealing. Complete defect recovery occurred in hydrogen irradiated sample at 673 K. Helium irradiated sample showed distinct S-parameter stages corresponding to vacancy annealing, nucleation of He-vacancy embryos and growth of bubbles under isochronal annealing. In sequential irradiated samples, the sequence of irradiation influences the number of surviving vacancies or the nature of defect-complexes. A reduced S-parameter is observed

in the sequential irradiated samples from 573 to 673 K as compared to the helium irradiated sample due to the formation of H-He-V complexes. An increase in S-parameter due to helium bubble growth occurred at 773 K in all samples irradiated with helium. In this study, the presence of hydrogen or irradiation sequence does not seem to influence the growth of helium bubbles.

Chapter 5

Study of vacancy defects and their thermal stability in MeV Fe ion irradiated RAFM steel

5.1. Introduction

Irradiation effects in RAFM steels have been under extensive investigation to understand their tolerance to radiation damage as a fusion first-wall material [3, 21, 24, 186, 187]. Neutron irradiation degrades the desirable mechanical properties of core structural materials and shortens their service life [78, 188, 189]. Size and distribution of irradiation-induced defects such as dislocation loops and voids, irradiation-induced changes in the growth and volume fraction of precipitates such as MX and M₂₃C in RAFM steel have been influenced by the dose and dose rate of neutron irradiation [190]. In addition to that, neutron irradiation also promotes the segregation of alloying elements such as Cr along the grain boundaries in RAFM steel [191]. Since some of the precipitates presented in the Ferritic/Martensitic steels are having very crucial role in the high-temperature mechanical properties, their stability against irradiation-induced deformations is vital in the in-core applications of a nuclear reactor [37, 81, 192, 193].

Self-ion irradiation is an efficient alternative to study neutron-induced damage in reactor materials due to high amount of defect production within a short duration. But the self-ion irradiation produces a shallow defected region close to the sample surface as compared to neutron irradiation. This free surface acts as a sink for irradiation-induced defects and influences their depth-wise distribution at the near-surface regions [194, 195]. The substantial variation of atomic displacement rate along the ion path and the imbalances in depth distribution of point defects also influence the survival of irradiation-induced defects [195-197]. Hence, it is essential to understand the nature and distribution of defects along the projected ion range to evaluate the irradiation-induced microstructural changes using ion-irradiation techniques. The current chapter investigates i) the effect of irradiation dose on the nature and depth distribution of irradiation-induced defects and their recovery under isochronal annealing and ii) the influence of irradiation temperature and pre-injected helium at fusion relevant He/dpa ratio in the stability of vacancy-type defects and their evolution in INRAFM steel.

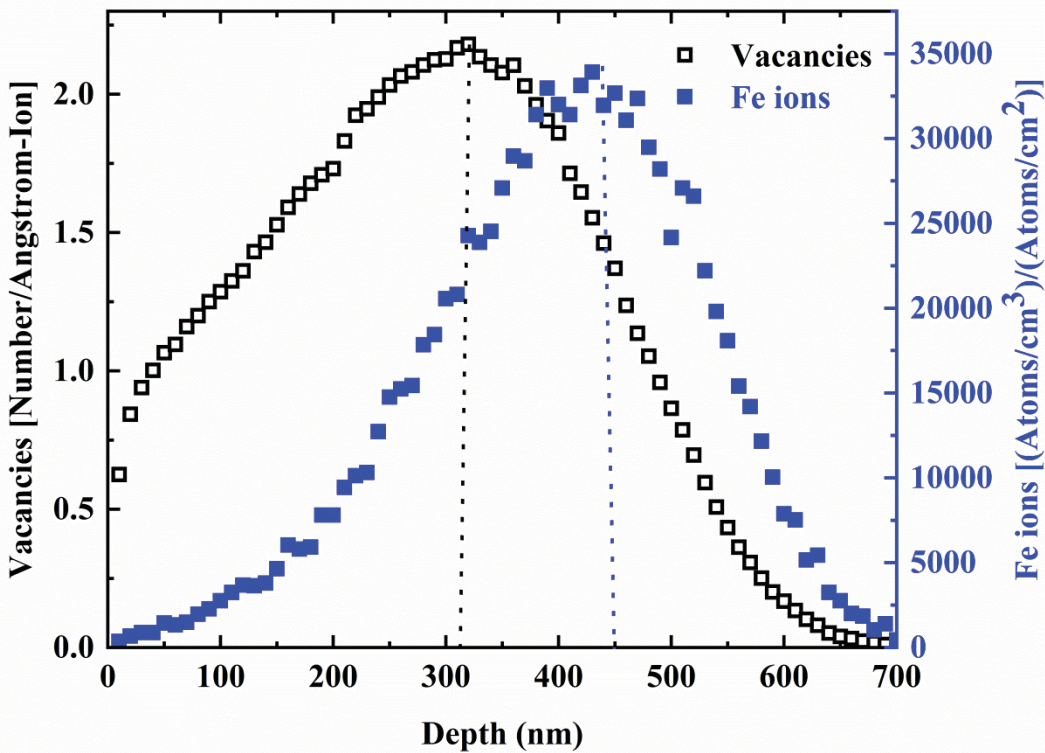


Figure 5.1 Vacancy and ion distribution profile of 1.1 MeV Fe ions into INRAFM steel calculated using SRIM 2013 code. Vacancy and ion peaks are shown using dotted lines.

5.2. Experimental

5.2.1. Irradiation procedure

The normalized and tempered samples were irradiated with 1.1 MeV Fe ions to doses 0.1, 1, 30, 70 and 100 dpa (peak doses) at room temperature. Figure 5.1 shows the Fe ion and vacancy distribution profiles calculated using SRIM 2013 code [142]. The Fe ion distribution peak occurs at around 450 nm, whereas the vacancy distribution peak occurs at 310 nm. The 0.1 dpa sample was irradiated with a beam current of 25 nA (at a displacement rate of $\sim 4 \times 10^{-4}$ dpa/sec) whereas all other samples were irradiated with a beam current of 250 nA (at a displacement rate of $\sim 4 \times 10^{-3}$ dpa/sec). During irradiation, the sample surface was scanned using ion beam to ensure a uniform irradiated surface. Hence, a lower damage rate was chosen for 0.1 dpa sample so as to increase the irradiation time thus ensuring better spatial uniformity. Since the defect production and recombination rates are strongly influenced by the ion beam current or displacement damage rate, separate isochronal annealing study was carried out on the 0.1 dpa sample. The irradiated samples (1 to 100 dpa) were characterized by using Grazing Incidence X-ray Diffraction (GIXRD), nanoindentation and positron beam based Doppler broadening spectroscopy.

In the second study, high-temperature irradiation experiments were carried out on INRAFM steel samples with and without pre-injected helium. Samples were irradiated at room temperature, 473, 673 and 773 K. One set of samples were irradiated at elevated temperatures with 1.1 MeV Fe ions to a dose of 70 dpa. Another set of samples were pre-injected with a uniform concentration of He ions to 700 appm and then irradiated with 1.1 MeV Fe ions to a dose of 70 dpa at elevated temperatures. The irradiation dose was chosen such that the He/dpa ratio (10 appm/dpa) at the peak damage region is equivalent to the fusion reactor first-wall irradiation conditions. Positron annihilation study has been carried out to understand the effect of pre-injected helium and irradiation temperature on the survival and growth of vacancy-type defects. More details on the high-temperature irradiation procedure and experimental details have been given in section 5.3.4.

5.2.2. Positron annihilation studies

The defect recovery under isochronal annealing in the samples irradiated at room temperature was carried out using positron beam based Doppler broadening spectroscopy. The samples were annealed from room temperature to 1073 K in steps of 100 K with a holding time of 1 h at each annealing step. Since the irradiation at 0.1 dpa was done with a low ion beam current, a separate annealing study was conducted on the 0.1 dpa samples. Among the high-dose samples, 1 and 100 dpa samples were also annealed at similar conditions and defect-recovery studies were carried out. Defect studies in high-temperature irradiated samples were also carried out using positron annihilation studies.

5.2.3. GIXRD studies

The GIXRD measurements were carried out on as-irradiated samples of doses from 1 to 100 dpa at an angle of incidence of 0.6°. Figure 5.2 shows the GIXRD spectra of unirradiated and irradiated INRAFM samples. The peaks were identified and indexed. The crystal structure remains stable, and no irradiation-induced phase changes were observed. Irradiation-induced changes in micro-strain and coherent domain size were studied using the Williamson-Hall plot method [147],

$$\beta_{2\theta} \cdot \frac{\cos\theta}{K_S \cdot \lambda} = \frac{1}{\langle D \rangle_V} + \varepsilon \cdot \frac{4\sin\theta}{K_S \cdot \lambda} \quad (5.1)$$

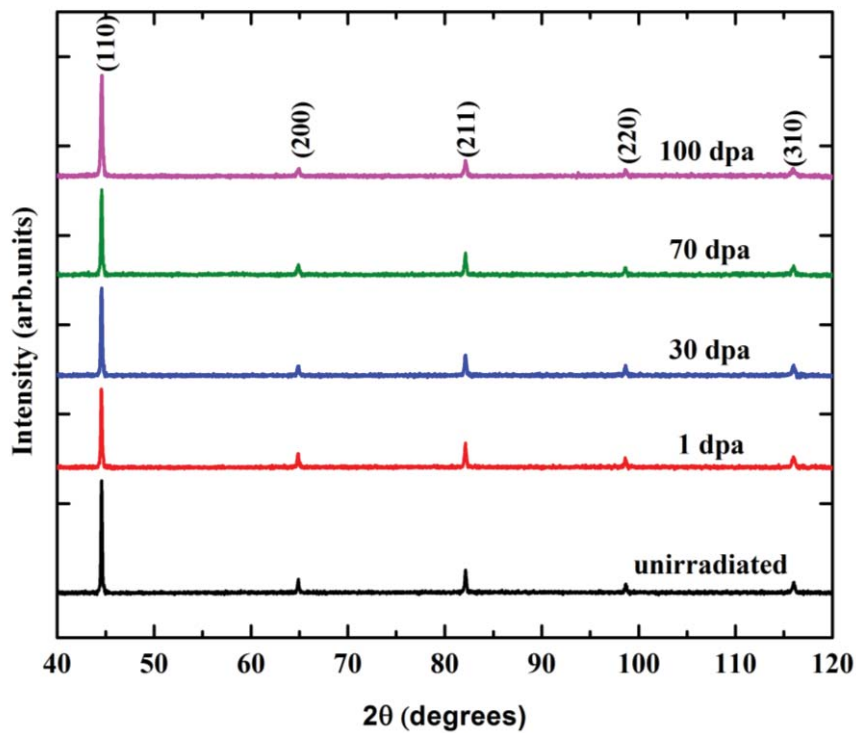


Figure 5.2 GIXRD spectra of unirradiated and irradiated INRAFM samples. The individual plots are up-shifted along the Y-axis for clarity. The peaks were identified and indexed.

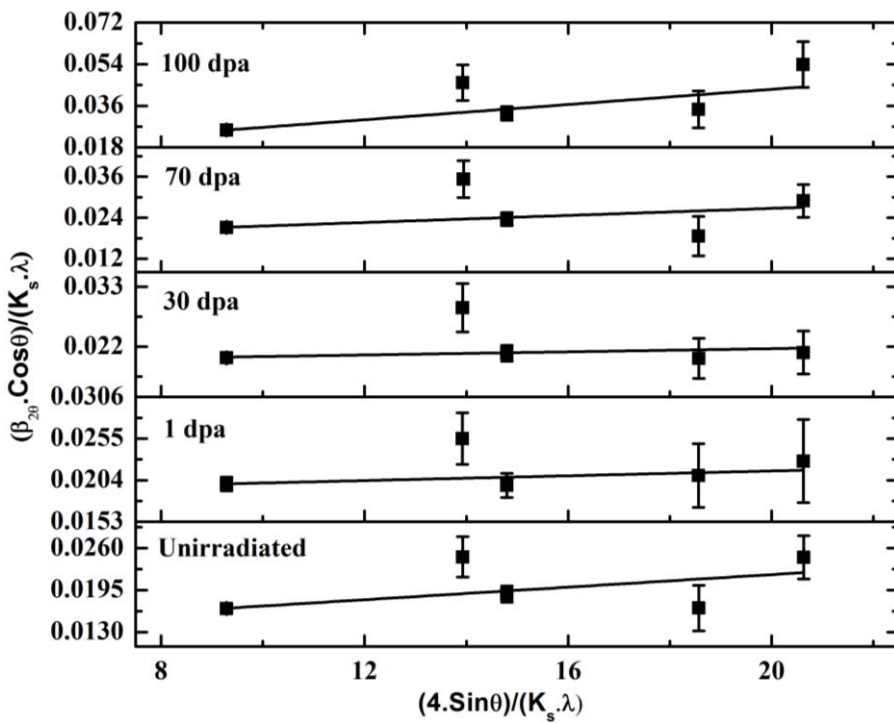


Figure 5.3 Williamson-Hall plot of unirradiated and irradiated samples.

Where $\beta_{2\theta}$ is the integral breadth in radians, θ is the Bragg angle in radians, λ is the wavelength of X-rays in nm, K_s is the Scherer constant, $\langle D \rangle_v$ is the average crystallite size or coherent domain size in nm, ε is the average micro-strain (in %) presented in the material. The θ and $\beta_{2\theta}$ values were obtained by fitting the individual peaks with a Pseudo-Voigt function. Figure 5.3 shows the Williamson-Hall plot obtained by using $(\beta_{2\theta} \cdot \cos\theta / K_s \cdot \lambda)$ along the Y-axis and $(4\sin\theta / K_s \cdot \lambda)$ along the X-axis which gives the micro-strain (ε) as slope and the coherent domain size ($\langle D \rangle_v$) as the inverse of intercept.

5.2.4. Nanoindentation studies

The nanoindentation measurements were carried out on as-irradiated samples from 1 to 100 dpa. The indentations were carried out with a maximum linear load of 50 mN, where the loading and unloading rates were maintained at 100 mN/min with a 5 seconds pause at the maximum load. The sinus frequency and amplitude were maintained at 1 Hz and 5 mN, respectively. Five indents were performed per sample, and the statistical average of the nanohardness data has been taken. A typical load profile of the indentation and the optical image of the indented surface have been shown in figure 5.4.

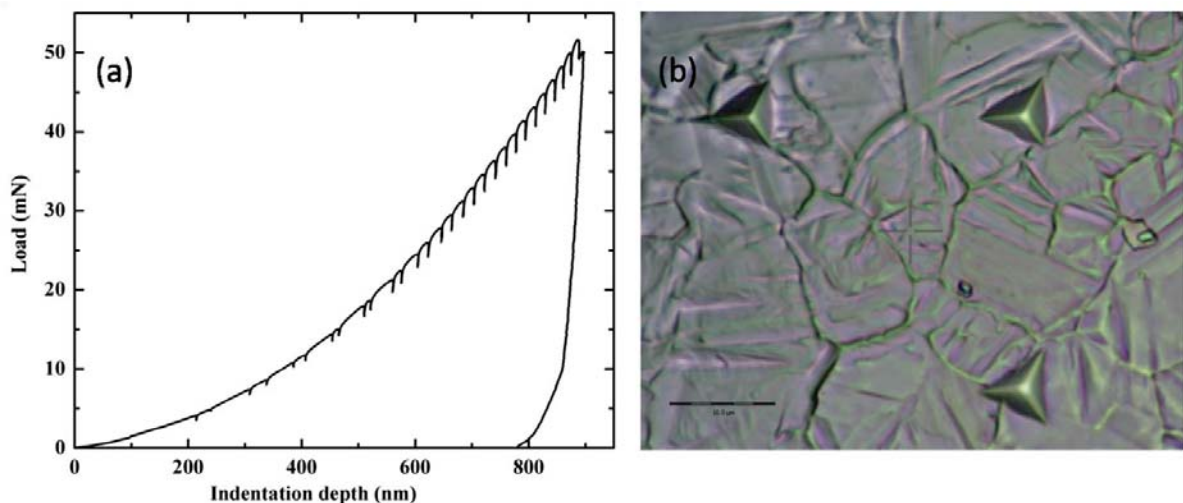


Figure 5.4 a) Typical load profile of the nanoindentation and b) optical micrograph of the indented surface.

5.3. Results and discussion

5.3.1. Defect recovery under isochronal annealing in low-dose (0.1 dpa) sample

The normalized S-parameter vs. positron beam energy plots of unirradiated, as-irradiated and isochronally annealed INRAFM samples irradiated to 0.1 dpa is shown in figure 5.5. The S-parameters were normalized with respect to the bulk-saturated S-parameter value of the unirradiated sample. The as-irradiated sample shows a higher S-parameter as

compared to the unirradiated sample. The ion irradiation at room temperature produces point defects such as vacancies and interstitials, which can aggregate to form higher-order defects such as point defect-clusters or dislocations. The presence of vacancy-type defects increases the S-parameter of as-irradiated sample as compared to the unirradiated sample. As the temperature increases from RT to 373 K, the S-parameter shows a narrow increase. This may be because of the migration and clustering of nearby vacancies at 373 K. The S-parameter shows an overall decreasing trend with further annealing from 373 to 673 K, followed by an almost stable region till 973 K, and finally coincides with the unirradiated values at 1073 K. The microstructure of INRAFM steel contains intrinsic defects such as dislocations, precipitates, laths, grain-boundaries and sub-grains, which act as sinks for irradiation-induced point defects. As the annealing temperature increases, in addition to the vacancy-interstitial recombination, the point defects migrate and annihilate at the surface and the sinks in the interior. This results in an overall reduction in S-parameter with respect to the annealing temperature, and complete recovery from irradiation-induced defects occurs at 1073 K.

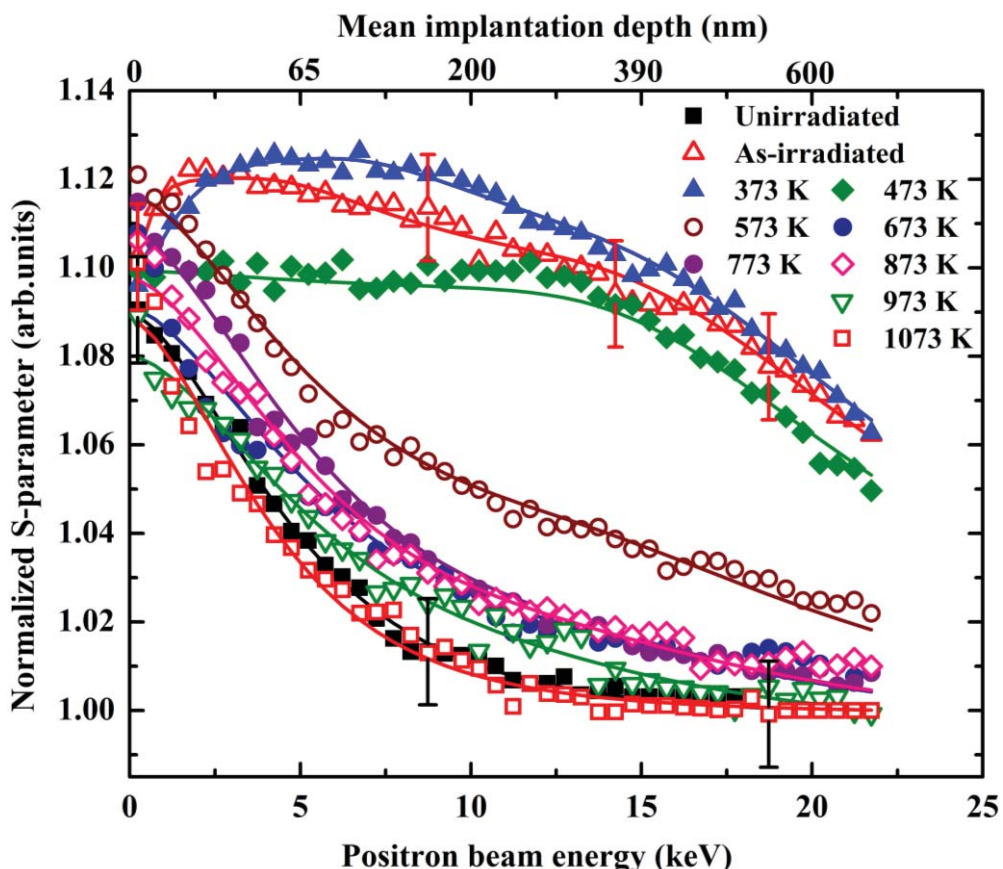


Figure 5.5 Normalized S-parameter vs. positron beam energy plots of INRAFM steel irradiated with a dose of 0.1 dpa. The lines are fits to the experimental data using VEPFIT programme. Positron mean implantation depth is shown on the top x-axis. Typical error bars are shown for selected data points.

Figure 5.6 shows the S-parameter as a function of sample depth obtained using VEPFIT analysis. The S-parameter and the diffusion length of positrons in the unirradiated sample are deduced by giving a single layer fit. The as-irradiated and 373 K annealed samples were fitted with three layers; two layers in the irradiated region and an unirradiated bulk layer. The irradiated region in as-irradiated sample consists of a near-surface layer of thickness 90 nm and a second defected layer that extends up to 845 nm. Both the layers in irradiated region widens as the annealing temperature increases to 373 K. The S-parameter and width of near-surface layer in 373 K sample is high as compared to the as-irradiated sample, which may be due to the migration and agglomeration of nearby vacancies in the near-surface region at 373 K. This near-surface layer completely disappears after annealing at 473 K. All the samples from 473 to 973 K are fitted with two layers- a defected layer and an unirradiated bulk layer. The sample at 1073 K is fitted with single layer since the damaged layer disappeared due to complete defect-recovery.

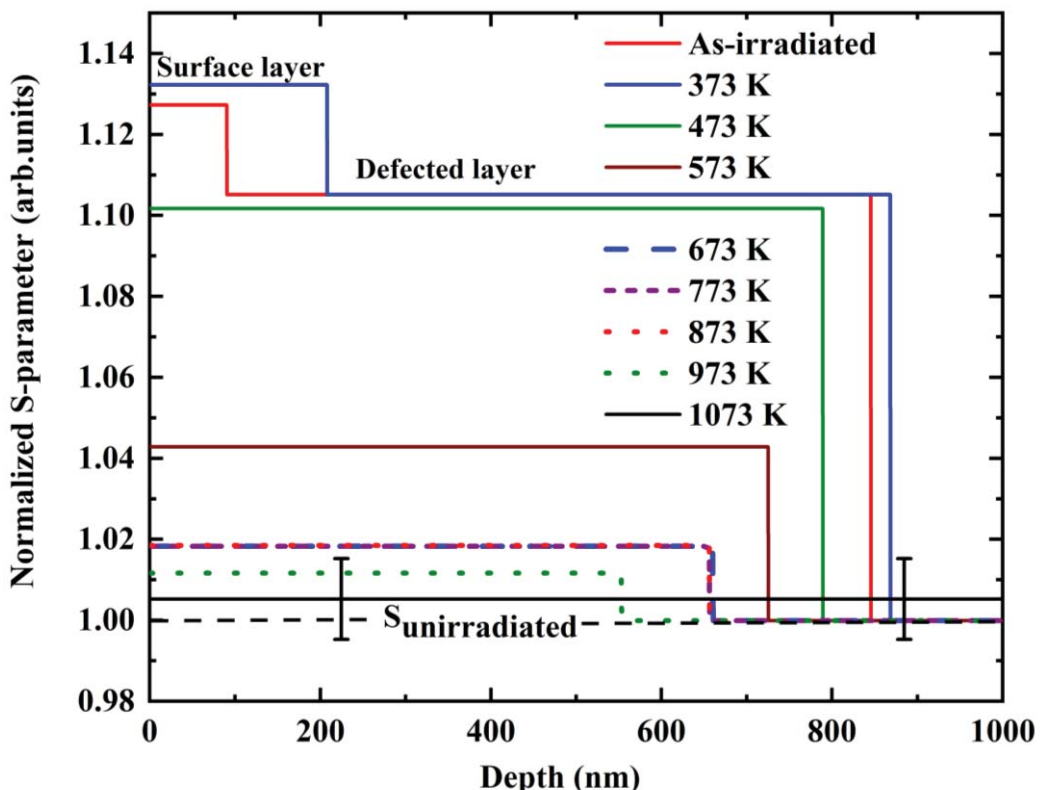


Figure 5.6 Normalized S-parameter vs. depth plot of 0.1 dpa irradiated sample deduced from VEPFIT analysis.

The normalized S-parameter (S_{defected}) and width of the defected layer obtained from figure 5.6 are plotted against the annealing temperature and is shown in figure 5.7. As the annealing temperature increases, an initial reduction is observed in both S_{defected} and width of

defected layer till 673 K, followed by a stable region from 673 to 873 K and then decreases with further annealing till 1073 K. The initial reduction in S_{defected} and width from as-irradiated state to 673 K is due to thermally enhanced migration and annihilation of vacancies at the sinks. The S_{defected} decreases due to vacancy annealing, whereas the reduction in width is due to the migration of vacancies towards the surface. An isochronal annealing study using PAS on EUROFER-97 steel, which was normalized and tempered at the same temperatures of INRAFM steel showed the formation and coarsening of additional carbide precipitates between 700 to 1000 K [198]. The additional carbide precipitates that formed below the tempering temperature (1033 K) can retard the movement of point defects, point defect clusters and dislocations. This makes the S_{defected} and width of defected layer stable between 673 to 873 K. Above 873 K, these carbide precipitates coarsen, which reduces their efficiency to trap and retard the movement of defects. Hence, at temperatures above 873 K, the enhanced mobility of these defects and their annihilation at the sinks reduce S_{defected} and width further.

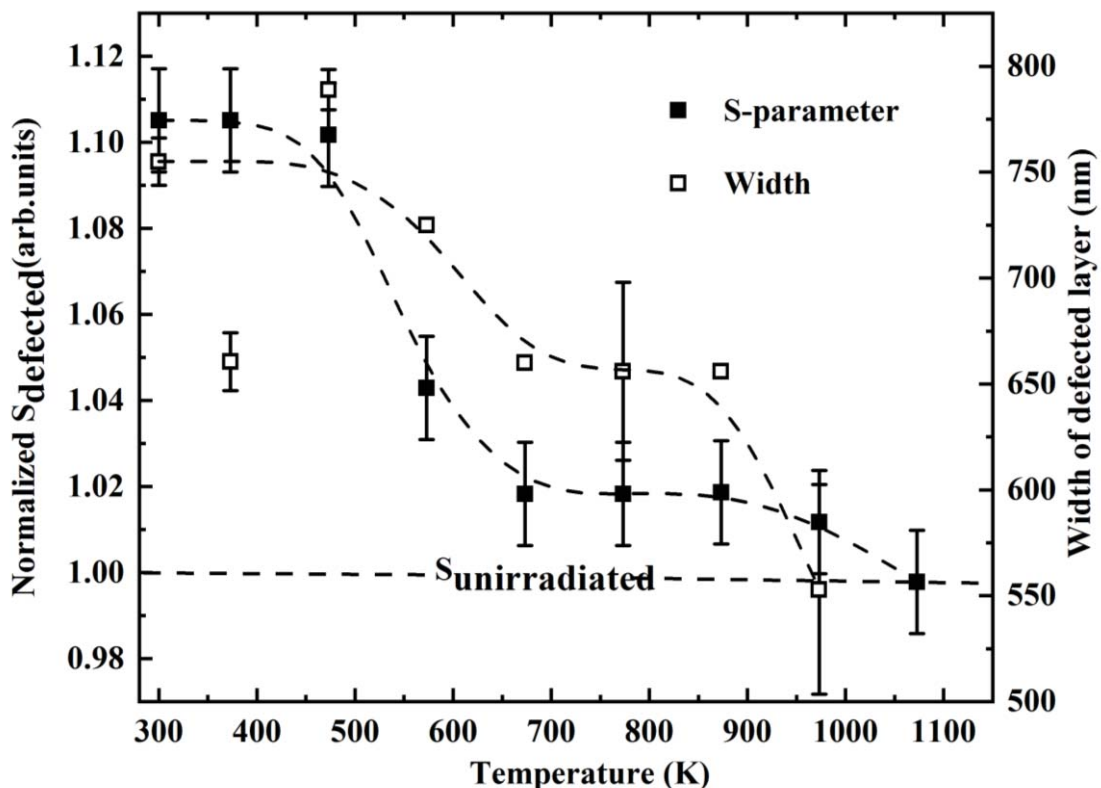


Figure 5.7 Variation of normalized S -parameter and width of the defected layer obtained from VEPFIT analysis (Figure 5.6) with respect to the annealing temperature. Data points are connected with dashed lines to guide the eye. Width of defected layer at 373 K does not fall in the trend shown by other temperatures due to the presence of a wider near-surface layer.

The average of normalized S and W-parameters are calculated from the region 310 ± 100 nm for all the samples and shown in the S-W correlation plot in figure 5.8. This region (210 to 410 nm) has been chosen to avoid the influence of near-surface region and unirradiated bulk, and to get the exact nature of S-W correlation from a region around the vacancy peak. The linear nature of S-W correlation plot indicates that similar kind of defects exists in the unirradiated and irradiated materials throughout the annealing temperatures. These defects may be vacancies or vacancies trapped at the interface of secondary precipitates or dislocations.

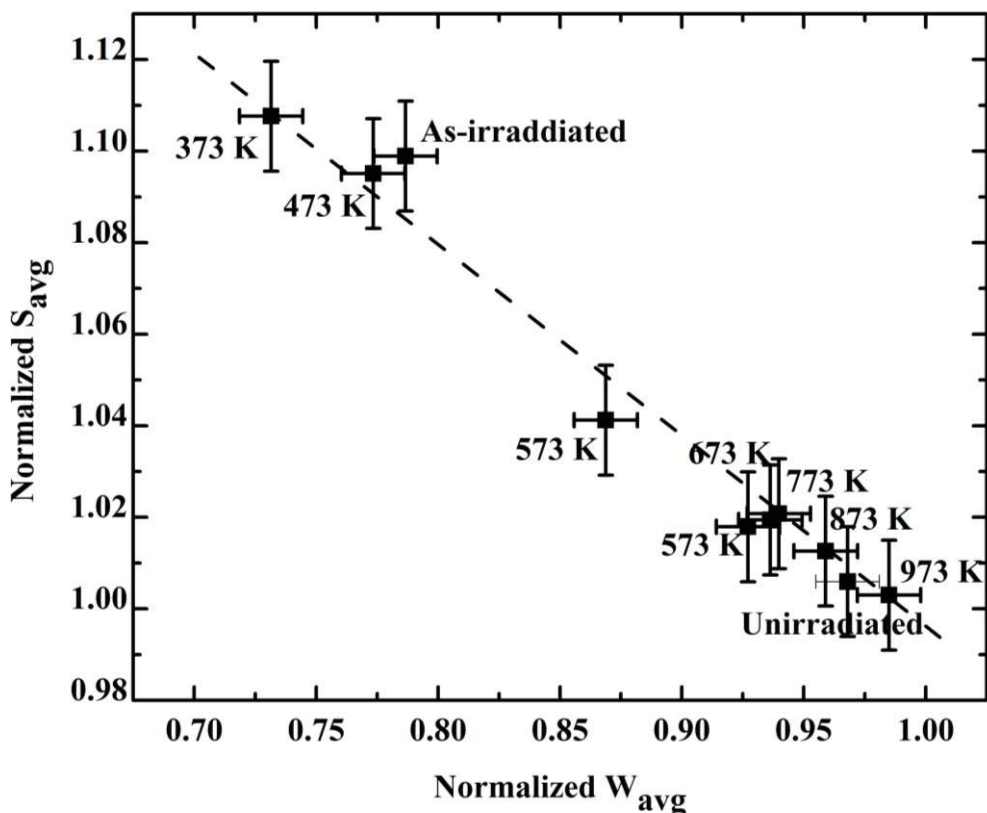


Figure 5.8 S-W correlation plot of 0.1 dpa sample obtained using the average of normalized S and W-parameters. The normalized S and W values were averaged around the depth region of 310 ± 100 nm.

5.3.2. Defect studies in as-irradiated high-dose (1-100 dpa) samples

5.3.2.1. Positron annihilation spectroscopic studies

5.3.2.1.1. S-parameter vs. positron beam energy plots

Figure 5.9 shows the normalized S-parameter vs. positron beam energy plots of INRAFM steel samples irradiated at different doses between 1 to 100 dpa. The experimental data points were fitted using VEPFIT programme [145]. In the case of 1 dpa sample, S-parameter shows an initial increase with increase in positron energy from 0 to 2 keV, and

remains stable from 2 to 8 keV, followed by a decrease with further increase in positron energy. The maximum S-parameter observed between 2 to 8 keV is due to the agglomeration of vacancies in the near-surface regions. The vacancy clustering in the near-surface region with helium irradiation was already observed in chapter-3. The S-parameter then decreases from 8 keV to 22 keV due to the reduction in number of vacancies with respect to the sample depth. Since the positrons are sensitive to open-volume defects, the S-parameter vs. positron beam energy plot is directly related to the distribution of vacancy-type defects in the irradiated material.

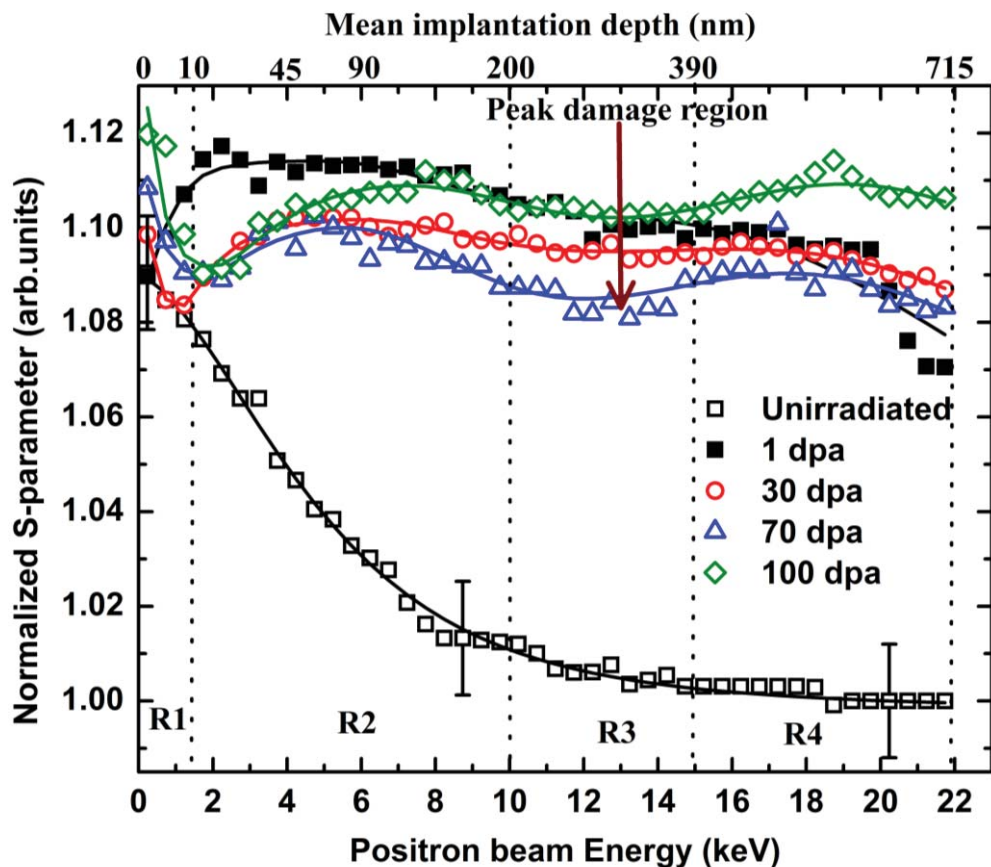


Figure 5.9 Normalized S-parameter vs. positron beam energy plots of the unirradiated and as-irradiated samples. Experimental data points were fitted using VEPFIT programme. Positron mean implantation depth is shown on the top axis.

As compared to the 1 dpa sample, different S-parameter behaviour is observed in the high-dose samples 30, 70 and 100 dpa. Based on the variations observed, the S-parameter vs. positron beam energy plots of these high-dose samples has been divided into four regions R1, R2, R3 and R4, as shown in figure 5.9. Region-1 (R1) extends from positron energy range 0 to 1.5 keV and exhibit a higher S-parameter at the surface followed by a decreasing trend, and reaches a minimum around 1.5 keV. Region-2 (R2) shows a hump in S-parameter due to

its increase and decrease in the energy range from 1.5 to 10 keV. Region-3 (R3) represents the region with a shallow dip in S-parameter from 10 to 15 keV, and the Region-4 (R4) shows another hump in S-parameter between the energy range 15 to 22 keV. As predicted by the SRIM calculation (figure 5.1), the irradiated region consists of a vacancy-rich and an injected-interstitial (Fe ion) rich region. The vacancy distribution peak occurs around 310 nm, whereas the injected-interstitial peak occurs at a depth around 450 nm. This constitutes a concentration gradient of vacancies and injected-interstitials near to the peak damage region. Due to this, the injected-interstitial atoms migrate towards the vacancy-rich region and recombine with the vacancies presented there. This reduces the number of vacancies or the size of vacancy clusters present at the peak damage region. This effect is known as injected-interstitial effect [194, 196, 197, 199, 200]. The dip in S-parameter at the middle of S-parameter vs. positron beam energy curves (Region-R3) observed at higher doses (30 to 100 dpa) is due to the reduction in concentration of vacancies or the size of vacancy clusters due to injected-interstitial effect. In ion-beam irradiation experiments, the recombination of vacancies and interstitials due to injected-interstitial effect reduces the super-saturation of vacancies at the peak damage region, which lead to a reduction in void swelling. Due to this, the damage profile obtained in ion beam irradiation experiments exhibits dual peaks (regions R2 and R4 in this study) [194]. The extent to which the experimental damage profile deviates from theoretically calculated profile is influenced by the parameters such as irradiation dose, dose rate, temperature, microstructure and chemical composition/purity of the material [194, 197, 200]. In this study, this effect is not observed in 1 dpa sample, less prominent in 30 dpa sample whereas clearly observed in 70 and 100 dpa samples. As the irradiation dose increases, the S-parameter and hence the vacancy concentration at the peak damage region (shown by an arrow in fig.5.9) initially decreases from 1 to 70 dpa due to the increase in vacancy-interstitial recombination, then a sudden increase is observed at 100 dpa due to the formation of larger vacancy clusters due to high-dose irradiation.

5.3.2.1.2. S-W correlation plot

The S-W correlation plot using the average of normalized S and W-parameters of the regions R1, R2, R3, and R4 is given in figure 5.10. As seen previously; the S-W plot of the unirradiated sample shows a linear nature due to the presence of single type of defects present in the sample. The data points of region R1 of all the doses show a linear nature and lie along with the data points of unirradiated sample. The S-W correlation plot of regions R2, R3 and R4 of all doses are also showing a linear nature and lie along another straight line. This shows that similar kind of defects present in these regions irrespective of the dose. The defects-

present in the regions R2, R3 and R4 are different from that of region R1 and unirradiated bulk.

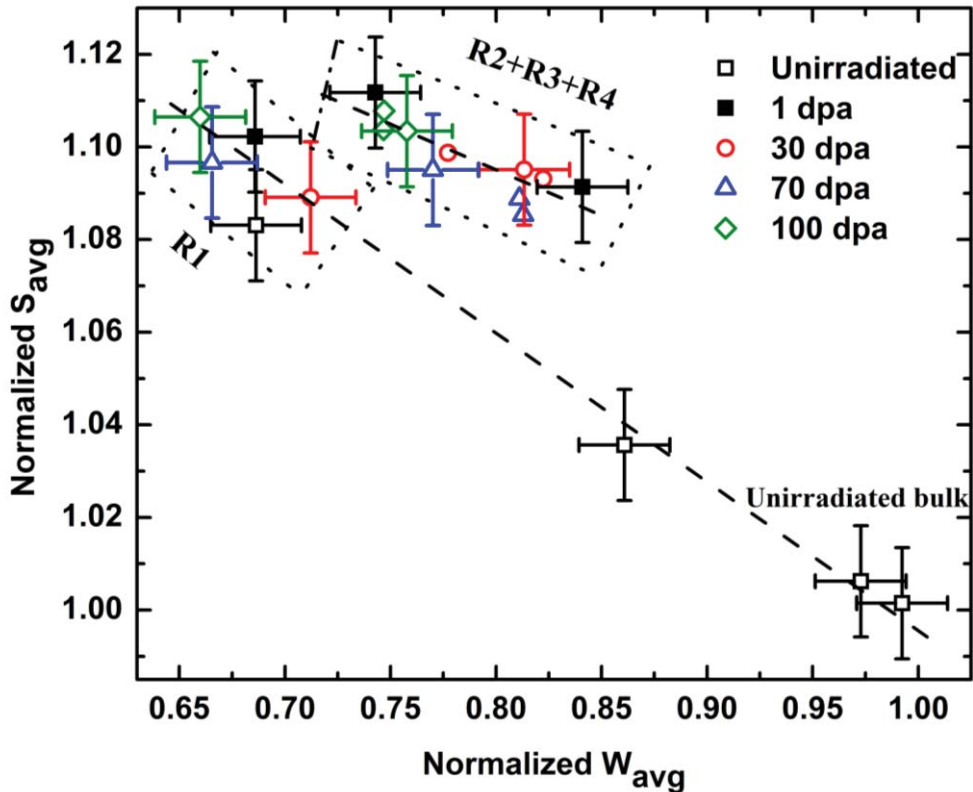


Figure 5.10 S-W correlation plot using the average of S and W-parameters from the regions R1, R2, R3, and R4 shown in figure 5.9.

5.3.2.1.3. VEPFIT Analysis

VEPFIT analysis has been employed to deduce the S-parameter values and the width of different regions observed in the normalized S-parameter vs. positron beam energy plots (figure 5.9). Figure 5.11 shows the normalized S-parameter vs. sample depth profile obtained from the VEPFIT analysis. The unirradiated sample was analysed by giving a single layer fit. The irradiated samples consist of an irradiated/damaged region followed by an unirradiated bulk region. The damaged region has been fitted with multiple layers according to the nature of the S-parameter variations observed in figure 5.9. The S-parameter and diffusion length values of the unirradiated bulk region of all the irradiated samples have been fixed to the bulk values of the unirradiated sample.

The 1 dpa sample is fitted with three layers (figure 5.11); two layers in the damaged region and an unirradiated bulk layer. The two layers observed in the damaged region consist of a near-surface layer where the vacancy agglomeration occurs and a second layer that pertains to a region where maximum damage is produced according to the SRIM calculation.

The near-surface layer is having a higher S-parameter ($S_{\text{normalized}}=1.118$) of width 150 nm due to the migration and agglomeration of vacancies towards the surface from the peak damage region. Hence contrary to SRIM predicted profile, the maximum damage accumulation is contained within the first 150 nm from the surface. The second damaged layer is having a lower S-parameter ($S_{\text{normalized}}=1.109$) and extends from 150 to 860 nm. This layer extends even beyond the maximum range of vacancies (650 nm, figure 5.1) predicted by SRIM, which is due to the thermal migration of irradiation-induced vacancies towards the unirradiated bulk region.

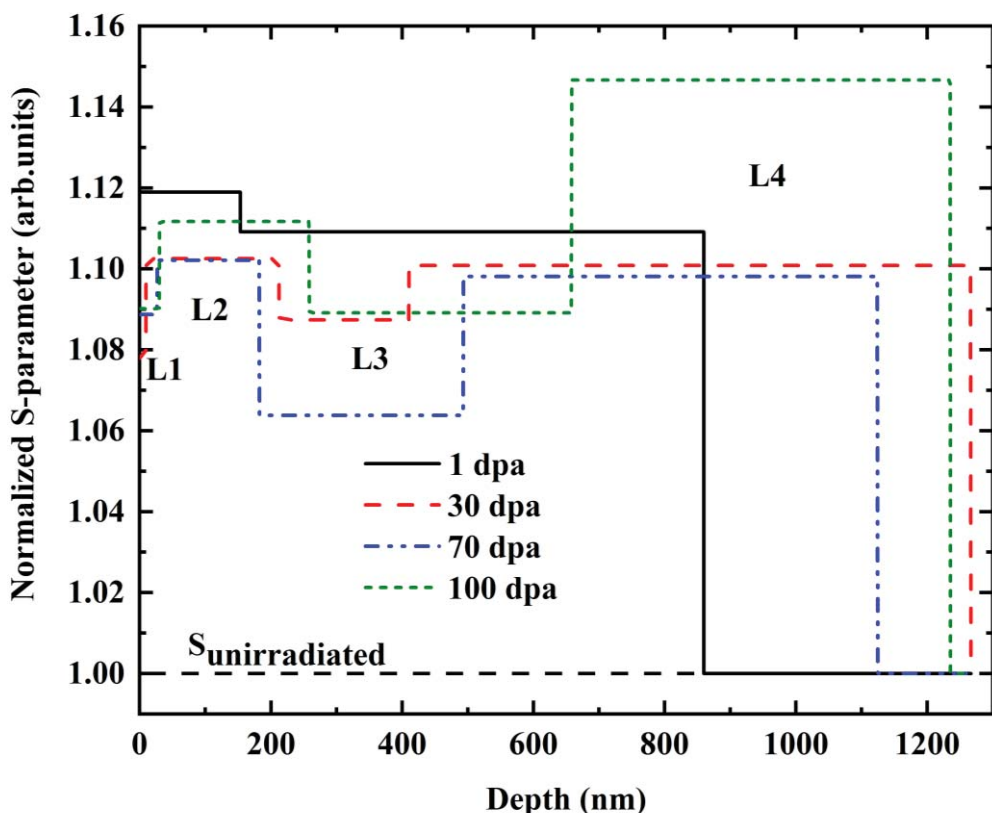


Figure 5.11 Normalized S-parameter vs. depth plot of the as-irradiated samples deduced from VEPFIT analysis.

The normalized S-parameter vs. positron beam energy curves of 30, 70 and 100 dpa samples were fitted with five layers: four layers in the damaged region (L1, L2, L3 and L4 as shown in figure 5.11) and an unirradiated bulk layer as the fifth layer. Four-layer (L1, L2, L3 and L4) modelling is adopted for the damaged region due to the presence of four different S-parameter regions (R1, R2, R3 and R4) in figure 5.9. Since the VEPFIT analysis consider the implantation profile and inter-layer diffusion of positrons while modelling the layered structure of S-parameter, the width of layers L1 to L4 may be different from the width of regions R1 to R4 (figure 5.9) that is obtained using the mean implantation depth of positrons.

Also, since the S-parameter value of the unirradiated bulk layer of all irradiated samples is fixed, the VEPFIT analysis extrapolates the data points to a depth beyond the mean implantation depth of positrons corresponding to the maximum energy (22 keV). Due to this, the upper boundary of layer L4 (> 1100 nm, figure 5.11) goes beyond the mean implantation depth of positrons that corresponds to the maximum energy (22 keV, 715 nm, figure 5.9). The width of layer L1 increases from 10 to 30 nm with increase in dose from 30 to 100 dpa. The width of vacancy-interstitial recombination-rich region (L3) is also increasing with an increase in dose from 30 to 100 dpa. Also, as the irradiation dose increases, the upper boundary of layer L3 shifts away from the surface towards the end of ion range. As shown in SRIM calculation (figure 5.1), the peak of injected Fe ion profile is closer to the end of ion range as compared to the peak of vacancy profile. Since the interstitials having low migration energy as compared to the vacancies, the injected-interstitials migrate faster towards the vacancy-rich region and recombine with vacancies along the path, thereby reducing the S-parameter. Due to this, with increase in dose, the upper boundary of vacancy-interstitial recombination-rich region (L3) shifts towards the end of ion range. Also, the size of vacancy clusters present in the interstitial-rich region (L4) may be different from the vacancy-rich region (L2). This is because; the critical size of vacancy-clusters that can survive vacancy-interstitial recombination in the interstitial-rich region is different from that of the vacancy-rich region. Hence, the S-parameter observed in the interstitial-rich region may be different from the vacancy-rich region. This is visible at 100 dpa where the high dose irradiation had introduced vacancy clusters, whose size is larger in the interstitial-rich region as compared to the vacancy-rich region.

5.3.2.2. GIXRD Results

As shown in figure 5.3, the Williamson-Hall plots of both unirradiated and irradiated samples show a positive slope due to the presence of tensile strain present in the material. The micro-strain and coherent domain size deduced from the Williamson-Hall plots are plotted as a function of the irradiation dose and shown in figure 5.12. A coherent domain size of 82 nm is observed in the unirradiated sample, which decreases with irradiation at 1dpa due to the presence of irradiation-induced defects and remains invariant with further increase in dose from 1 to 30 dpa. The coherent domain size increases with further increase in dose from 30 to 100 dpa, which may be an indication of the defect-recovery mechanism occurring at higher doses. Also, the micro-strain present in the samples does not show any appreciable change till 30 dpa, and increases with further increase in dose from 30 to 100 dpa. Unlike the

positron measurements, the interstitial-type defects also influence the coherent domain size and micro-strain variations observed in GIXRD studies. Hence, in addition to the distribution of vacancy-type defects as probed by positron, the interstitial-type defects must also be taken into account while explaining the results obtained in GIXRD studies. According to the $1/e$ penetration depth ($t_{1/e} = \sin \alpha / \mu$; α is the grazing angle of incidence and μ is the mass attenuation coefficient of x-rays) of x-rays [147], the depth probed by GIXRD in the present study is approximately 45 nm. This depth is approximately equal to the region probed by 0 to 4 keV positrons (in figure 5.9).

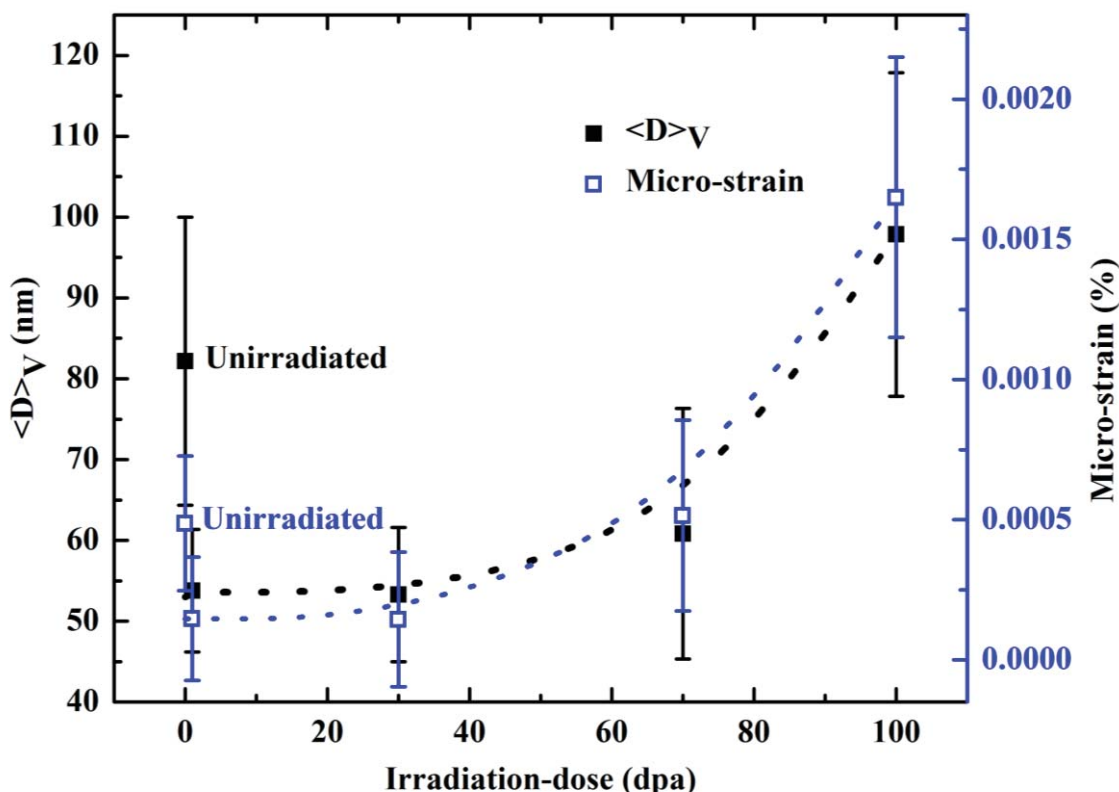


Figure 5.12 Coherent domain size $\langle D \rangle_v$ and micro-strain deduced from Williamson-Hall plot (figure 5.3) is plotted as a function of the irradiation dose. The dotted lines through the data points are just a guide to the eye.

In 1 dpa sample, as seen in the positron annihilation study (in figure 5.9), the GIXRD is probing the region where vacancy agglomeration is dominating. The interstitials produced along with the vacancies either move towards the sinks or agglomerate to form stable interstitial-loops. The irradiation-induced vacancy and interstitial-type defects can distort the crystallinity and hence, reduce the size of coherently scattering domains at 1 dpa as compared to the unirradiated sample. The micro-strain present in the unirradiated sample shows a tensile nature. The presence of vacancy-type defects may increase the tensile nature of the

micro-strain, whereas the interstitial-type defects can compress the lattice and reduce the tensile micro-strain. Hence, the net variation in micro-strain in irradiated samples is decided by the dominant mechanism among the above two processes. At 1 dpa, as the vacancies agglomerates to form bigger clusters at the near-surface regions (as seen in positron studies), the interstitials tend to segregate and form loops. Hence, the reduction in micro-strain observed at 1 dpa may be due to the presence of the interstitial loops. In the high-dose samples (30, 70 and 100 dpa), the GIXRD is probing the region where a dip in the S-parameter (from 0 to 4 keV positron energy) is observed in figure 5.9. The dip in S-parameter is due to the presence of a less-defected sub-surface layer which may be formed due to the migration of irradiation-induced defects towards the free surface. The increase in defect production due to irradiation is balanced by the defect-recovery mechanisms, which keeps both the coherent domain size and micro-strain invariant from 1 to 30 dpa. The presence of a less-defected sub-surface layer along with the defect-recovery processes that occur at higher doses keep the coherent domain size increasing from 30 to 100 dpa. When the defect recovery occurs, the concentration of both vacancy and interstitial-type defects decreases. The increase in micro-strain from 30 to 100 dpa may be influenced by the reduction in interstitial-loops.

5.3.2.3. Nanoindentation study

The variation of nanohardness with respect to indentation depth is shown in figure 5.13. The unirradiated sample shows high hardness at the surface, which decreases and saturate after 500 nm. The higher hardness at the surface is due to the indentation size effect [201, 202] or the surface defects present in the material. All the irradiated samples show higher hardness values as compared to the unirradiated sample due to the presence of irradiation-induced defects in the former. The irradiated sample does not show a monotonous variation in nanohardness with respect to dose. An overall increase in nanohardness observed with irradiation dose till 30 dpa, after which it decreases with further increase in dose from 30 to 70 dpa, and increases again at 100 dpa. The initial increase in nanohardness with an increase in dose up to 30 dpa due to the increase in irradiation-induced defects is well understood. But, in order to explain the reduction in nanohardness at 70 dpa and its further increase at 100 dpa, it is essential to invoke the defect-recovery due to injected-interstitial effect that was observed in positron annihilation study.

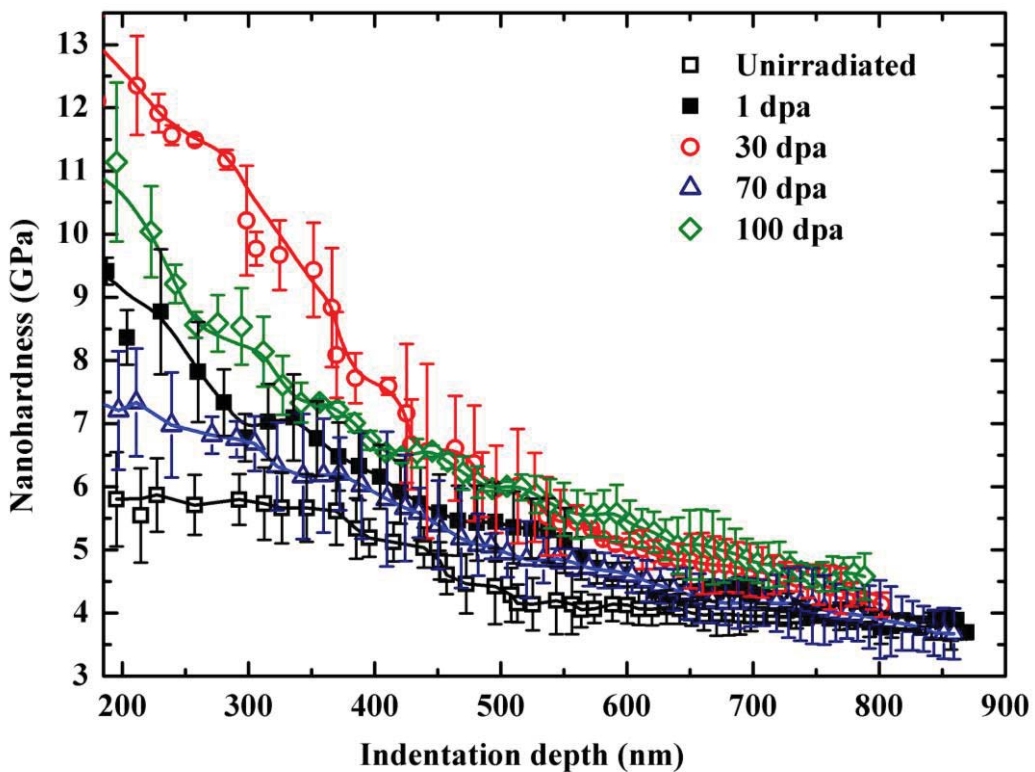


Figure 5.13 Nanohardness vs. indentation depth plot of the as-irradiated samples. The lines through the data points are just a guide to the eye.

The average of nanohardness and normalized S-parameter values around the peak damage region (310 ± 100 nm) is deduced and plotted against the irradiation dose is shown in figure 5.14. The initial increase observed in the average nanohardness and S-parameter values with increase in dose are due to the presence of irradiation-induced defects. The maximum of S-parameter and nanohardness is observed at 1 dpa and 30 dpa doses, respectively. The S-parameter variations are sensitive to open-volume/vacancy-type defects alone, whereas both interstitial and open-volume type defects are responsible for nanohardness variations. Hence, it is not always possible to have one to one correlation between the S-parameter and nanohardness variations. Both the S-parameter and nanohardness shows a minimum value at 70 dpa. As revealed by the positron study, the reduction in nanohardness at 70 dpa (figure 5.14) is due to the recovery of irradiation-induced defects due to injected interstitial effect. Further increase in S-parameter and nanohardness at 100 dpa is due to the formation of larger vacancy clusters.

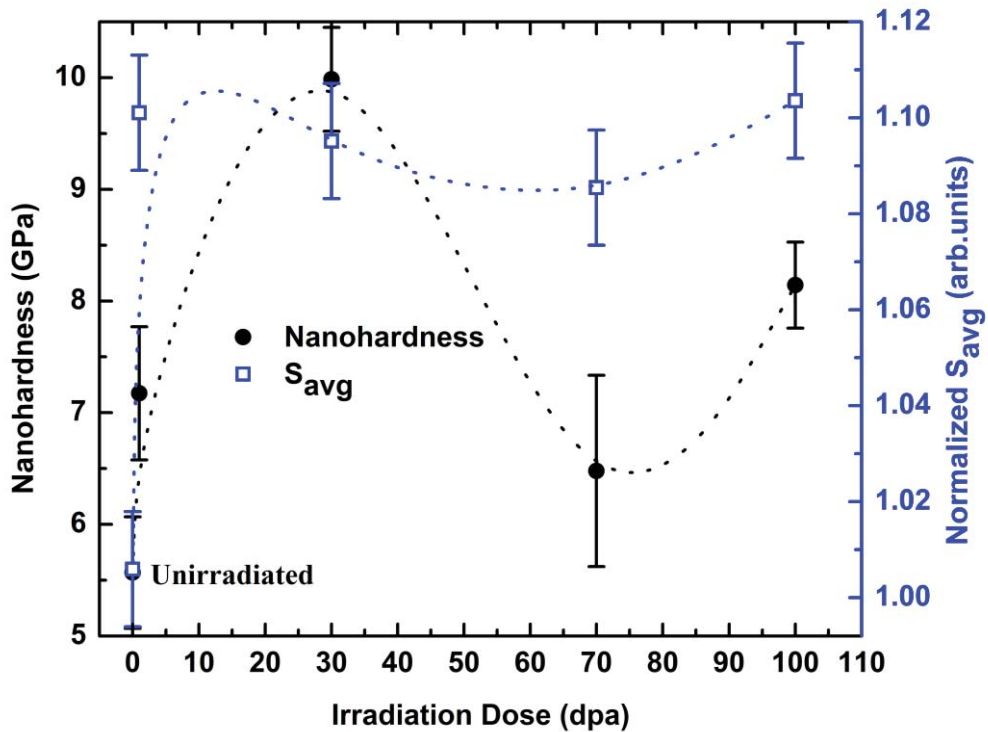


Figure 5.14 Variation of average of normalized S -parameter (from figure 5.9) and the average of Nanohardness from 310 ± 100 nm (from figure 5.13) region with respect to the irradiation dose. The line drawn through the data points is a guide to the eye.

5.3.3. Defect-recovery under isochronal annealing in 1 dpa and 100 dpa samples

The results of isochronal annealing studies performed on 1 and 100 dpa samples are shown in figure 5.15 (a) and (b). The 1 dpa sample shows an overall reduction in S -parameter with respect to the temperature, which is due to the annealing of vacancy-type defects. The complete defect recovery is observed at 673 K. The 100 dpa sample is also showing an overall reduction in S -parameter with respect to the annealing temperature and complete defect recovery occurred at 673 K. The dual hump observed in 100 dpa sample (figure 5.15 (b)) due to injected-interstitial effect is completely disappeared at 573 K. The dip in S -parameter observed at the near-surface region (Region R1) is also disappeared at 673 K. The normalized S -parameter vs. positron beam energy plots of figure 5.15 are analyzed using VEPFIT programme and the results obtained are given in figure 5.16 (a) and (b). For 1 dpa sample (figure 5.16 (a)), both the S -parameter and width of damaged layers (D_1 & D_2) decreases with annealing temperature due to the migration and recombination of point defects. At 573 K, the near-surface damaged layer (D_1) is almost diminished and the second damaged layer (D_2) is shortened to 490 nm. The damaged region except a narrow surface-

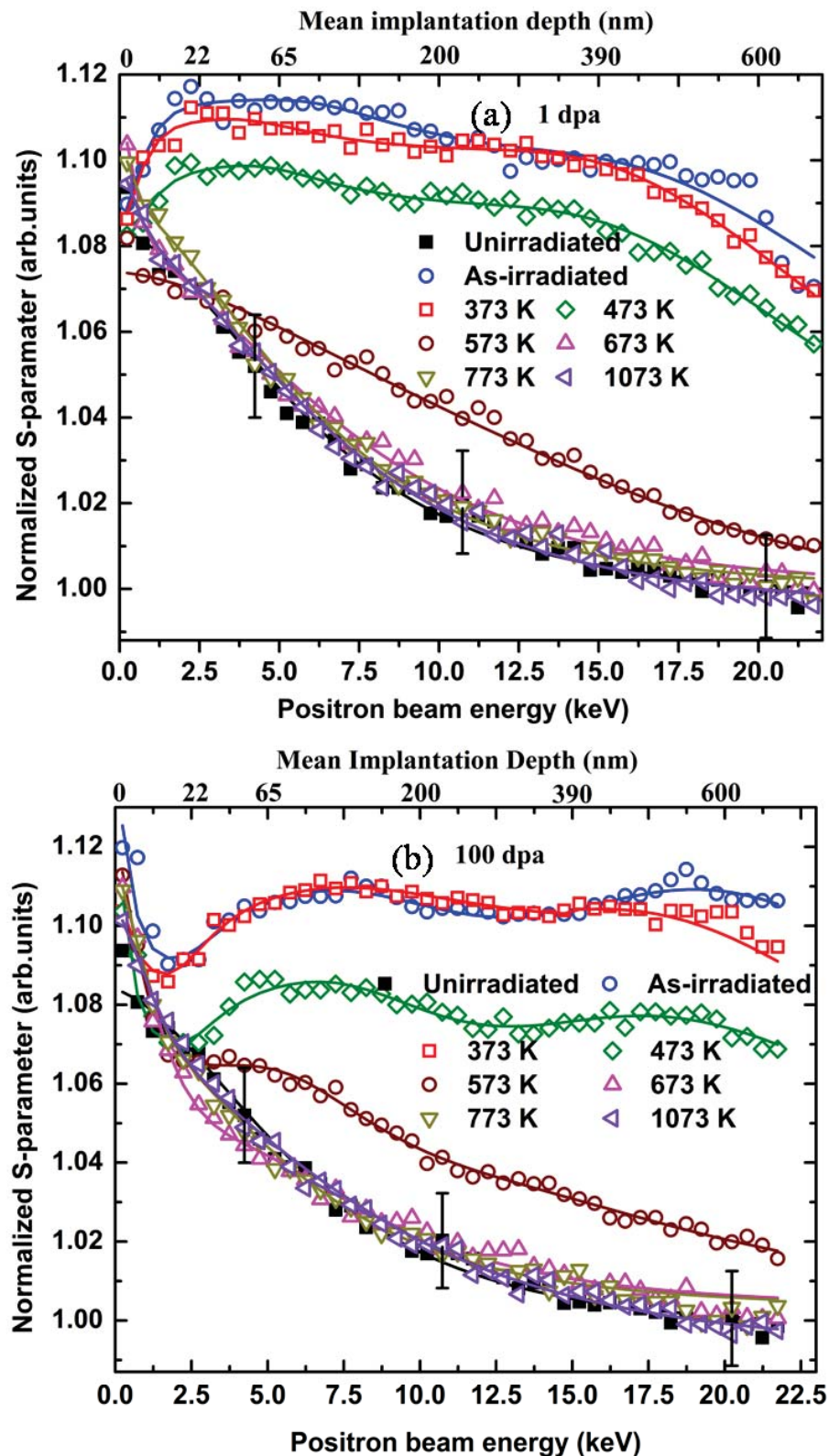


Figure 5.15 Normalized S-parameter vs. positron beam energy plots of a) 1 dpa and b) 100 dpa irradiated samples annealed from RT to 1073 K. The data points were fitted using VEPFIT programme.

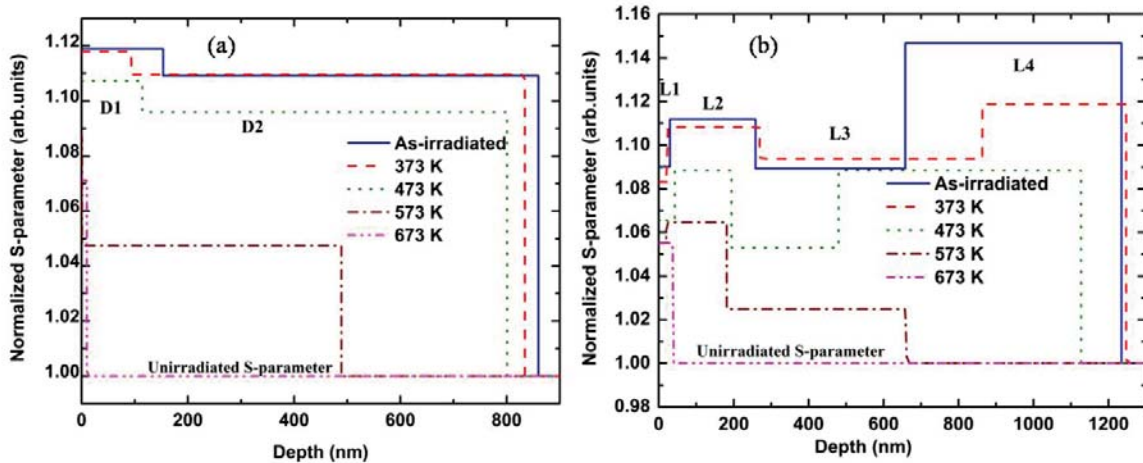


Figure 5.16 Normalized S-parameter vs. depth plot of a) 1 dpa and b) 100 dpa samples annealed from RT to 673 K.

layer having a width of few nanometers (~ 9 nm) is completely disappears after annealing at 673 K.

In the case of 100 dpa sample (Figure 5.16 (b)), all four layers (L1, L2, L3 and L4) in the damaged region exist till 473 K. At 373 K, the S-parameter and width of layer L4 decreases and layer L3 widen towards L4. This occurs because of the migration of point defects from layer L4 to L3. As the temperature increases to 473 K, the layers L3 and L4 shift towards the surface and completely merge to a single layer at 573 K. The layer L2 exists until 573 K which may be due to the presence of some stable vacancy clusters in the region, and the entire damaged region disappears at 673 K. Even at 673 K, in addition to the bulk-layer, a narrow surface-layer having a width of few nanometers is needed to get a better fit for the data points of both the samples. This may be due to the modification of sample surface by irradiation or oxide formation during annealing treatment.

The average of normalized S-parameter from regions R1, R2, R3, and R4 (as defined in figure 5.9) has been deduced for both doses at all annealing temperatures, and plotted as a function of temperature in figure 5.17. The S-parameter of the narrow region R1 shows fluctuations within the error bar and hence is neglected from further discussions. The regions R2, R3 and R4 shows a reduction in S-parameter with respect to the annealing temperature, and saturate at the bulk S-parameter value of the unirradiated sample at 673 K. The isochronal annealing study of 1 and 100 dpa samples does not show any stable S-parameter region as shown by the 0.1 dpa sample (figure 5.7, section 5.3.1). However, a small peak in the S-parameter (shown by an arrow, figure 5.17) observed in R2 at 873 K may be an indication for the secondary precipitates formed in this region. This is not visible in regions

R3 and R4, which may be due to the suppression of the formation of secondary carbide precipitates by high dose irradiation. It has been reported in an Atom Probe Tomography (APT) study by Tissot et al. [203] that, in Fe^{2+} ion irradiated FeCr alloys, the presence of injected interstitials can prevent the formation of Cr rich α' precipitates. Hence, further studies using APT or high-resolution electron microscopy need to be performed to confirm the present results.

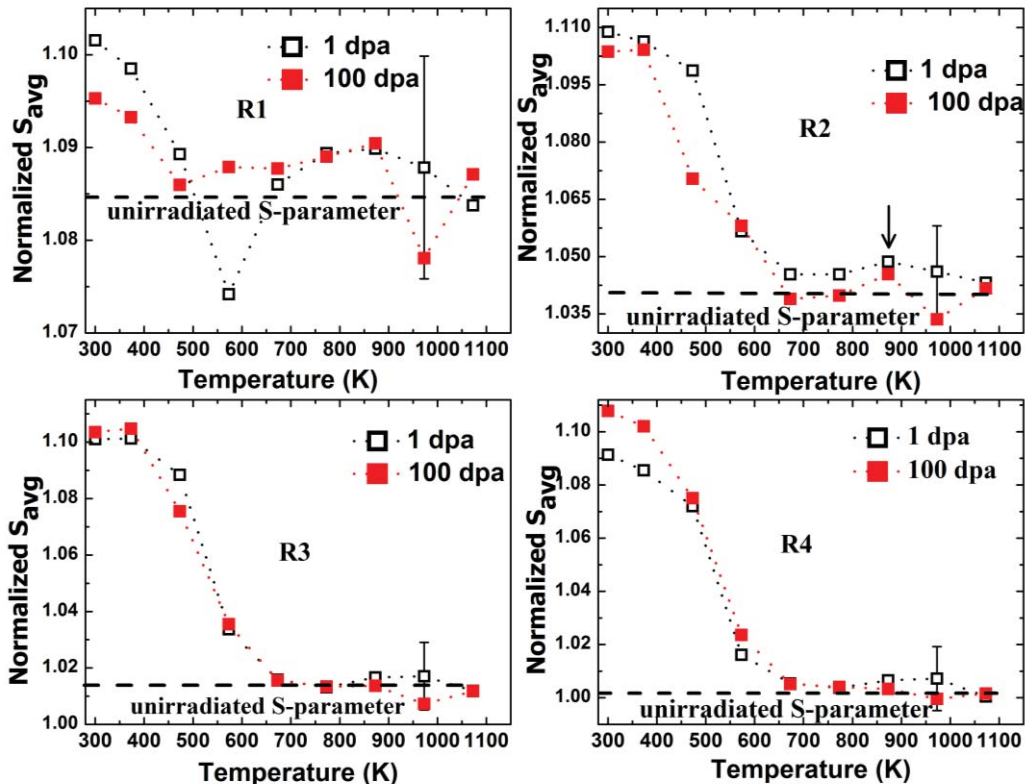


Figure 5.17 Average of normalized S -parameters from regions R1, R2, R3 and R4 are plotted as a function of annealing temperature for both 1 dpa and 100 dpa samples.

5.3.4. High-temperature irradiation studies

In this study, INRAFM steel samples were irradiated at higher temperatures with and without pre-injected helium. In the first study, the irradiations were performed with 1.1 MeV Fe ions to a dose of 70 dpa, without the presence of pre-injected helium. The second study was carried out by pre-injecting the samples with an uniform He concentration of 700 appm, and then irradiated with 1.1 MeV Fe ions to 70 dpa at temperatures RT, 473, 673 and 773 K. The above irradiation temperatures were chosen because they correspond to a defect annealing stage (473 K) as observed in chapter 3, bubble nucleation stage (chapter 3) and defect recovery stage in the previous study (673 K), and bubble growth stage in chapter 3

(773 K). Figure 5.18 shows the distribution of He ions and vacancies calculated using SRIM 2013 code [142]. Uniform concentration of He near to the peak damage region was obtained by implanting He ions at energies 50, 90 and 130 keV's to doses 5.5×10^{14} , 6.2×10^{14} , 6.4×10^{14} ions/cm² respectively.

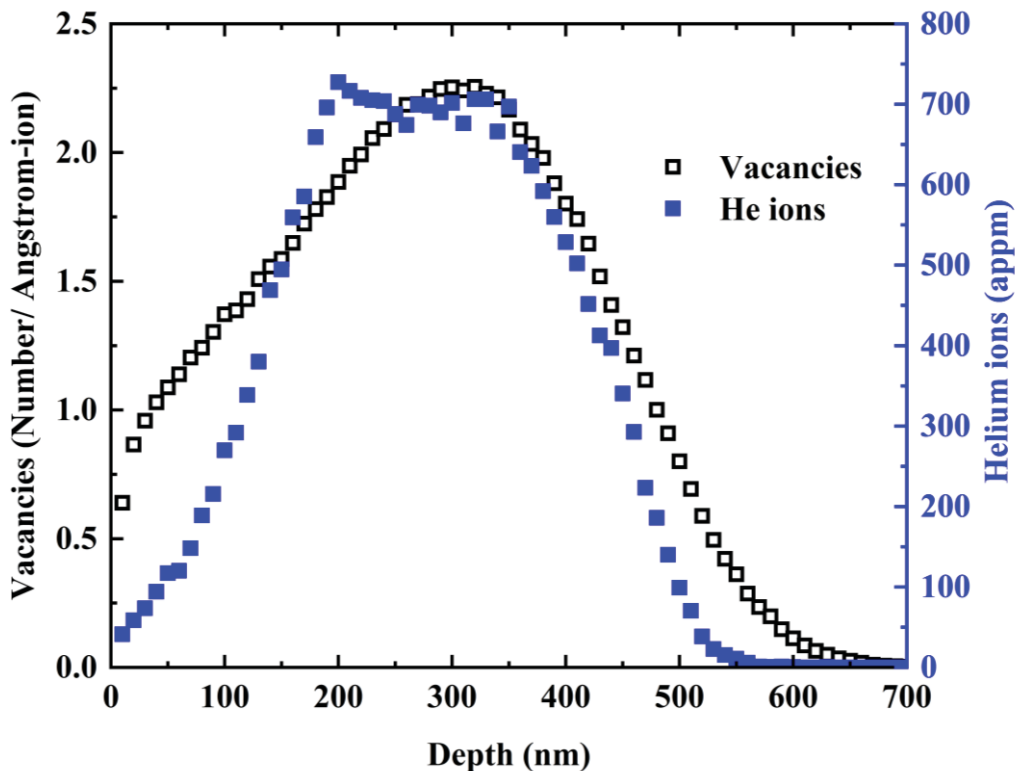


Figure 5.18 Vacancy distribution profile of 1.1 MeV Fe ions and the distribution of helium ions into INRAFM steel calculated using SRIM 2013 code. A uniform distribution of helium ions near to the vacancy peak is obtained by implanting with He ions at energies 50, 90 and 130 keV's.

5.3.4.1. High-temperature irradiation without pre-injected helium

Figure 5.19 shows the normalized S-parameter vs. positron beam energy plots of INRAFM steel samples irradiated with 1.1 MeV Fe ions to 70 dpa at various high-temperatures. Result of room-temperature irradiated sample from section 5.3.2 (figure 5.9) is also plotted for comparison. As compared to the sample irradiated at RT, a reduction in S-parameter is observed at 473 K due to the annealing of defects. Like the RT irradiated sample, a shallow dip is visible at the near-surface region of 473 K sample. As the temperature increases to 673 K, S-parameter curve shows further reduction and coincide with the unirradiated curve. Hence, as seen in the isochronal annealing study in section 5.3.3, complete defect recovery occurs at 673 K. The irradiation at 773 K does not show any further variation in S-parameter which shows the absence of any void growth without helium. This

study shows that, without pre-injected helium, all vacancy-type defects either move to sinks or recombine with interstitials; hence, a defect recovery is observed with high-temperature irradiation.

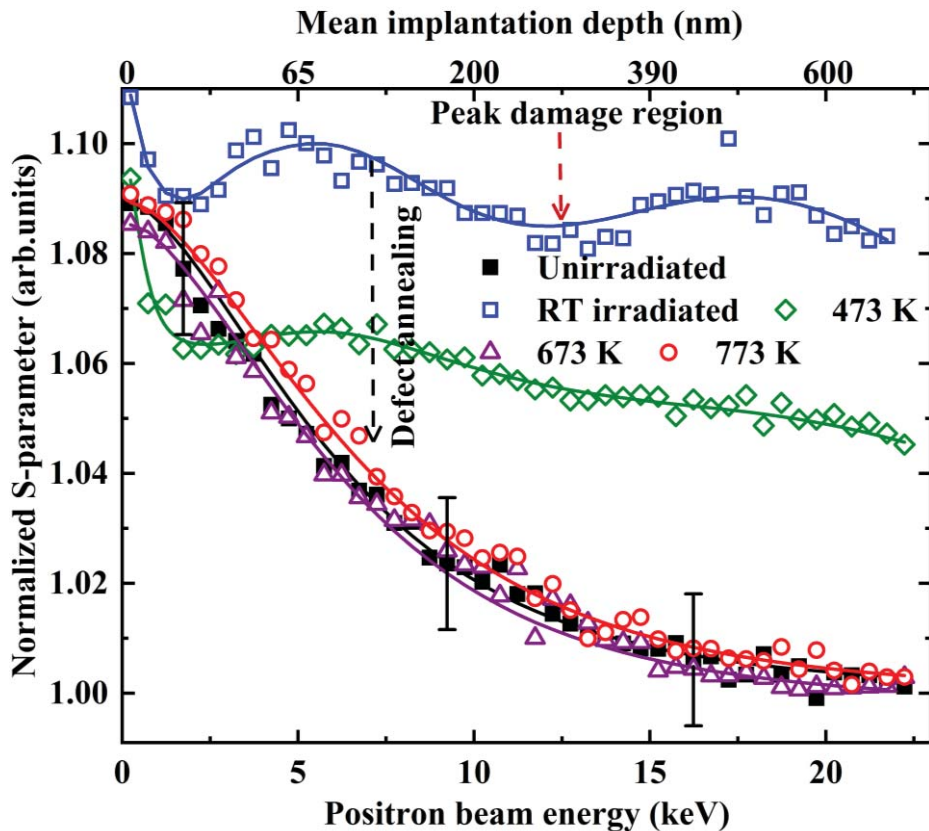


Figure 5.19 Normalized S-parameter vs. positron beam energy plots of INRAFM steel samples irradiated with 1.1 MeV Fe ions to 70 dpa at room temperature, 473, 673 and 773 K. The defect annealing from RT to 673 K is shown using an arrow.

5.3.4.2. High-temperature irradiation with pre-injected helium

The normalized S-parameter vs. positron beam energy plots of high-temperature irradiated samples with pre-injected helium is shown in figure 5.20 (a). The RT irradiated sample shows S-parameter values and trend similar to the sample that does not contain helium (as shown in figure 5.19). This is because of the saturation trapping of positrons at the vacancy-type defects induced by high dose Fe ion irradiation. In the presence of bare vacancies, positrons prefer to get trapped in a vacancy site rather than a helium-vacancy complex. The S-parameter decreases with increase in irradiation temperature from RT to 673 K, followed by an increase at 773 K. As the irradiation temperature increases, bare vacancies anneal out as seen in the previous section, or filled with helium thereby forming He_mV_n complexes. This reduces the S-parameter from RT to 673 K. As discussed previously, 473 K is the defect annealing stage at which some of the vacancies or clusters not stabilized by

helium are getting annealed out. The temperature 673 K is the bubble nucleation stage, and the increase in S-parameter at 773 K is due to helium bubble growth. The S-W correlation plots of the samples are shown in figure 5.20 (b) (Plots of RT irradiated sample is omitted due to scattering of data points). As compared to the unirradiated sample, the sample irradiated at 473 K deviate from a single straight line fit and shows two linear regions. This is because; the near-surface regions in 473 K samples contain He_mV_n complexes with a different m/n ratio as compared to the peak damage regions. Vacancy clustering at the near-surface regions observed in the previous irradiation studies also supports this. At 673 K, the S-W correlation plot shows a single straight line, which shows that a single type of defects presented in the sample. Since 673 K is the bubble nucleation stage, where critical He_mV_n nuclei have grown, the linear nature of S-W correlation plot shows that the critical He_mV_n nuclei having similar m/n ratio are distributed throughout the irradiated region. Further increase of irradiation temperature to 773 K again shows two linear regions in the S-W correlation plot. This is because, during helium bubble growth, those He_mV_n complexes or bubbles at the near-surface regions may de-trap helium easily as compared to the interior. Hence, their size or m/n ratio at the near-surface regions will be different from the interior. Due to this, two linear regions corresponding to the near-surface and peak damage regions are observed in the S-W correlation plot.

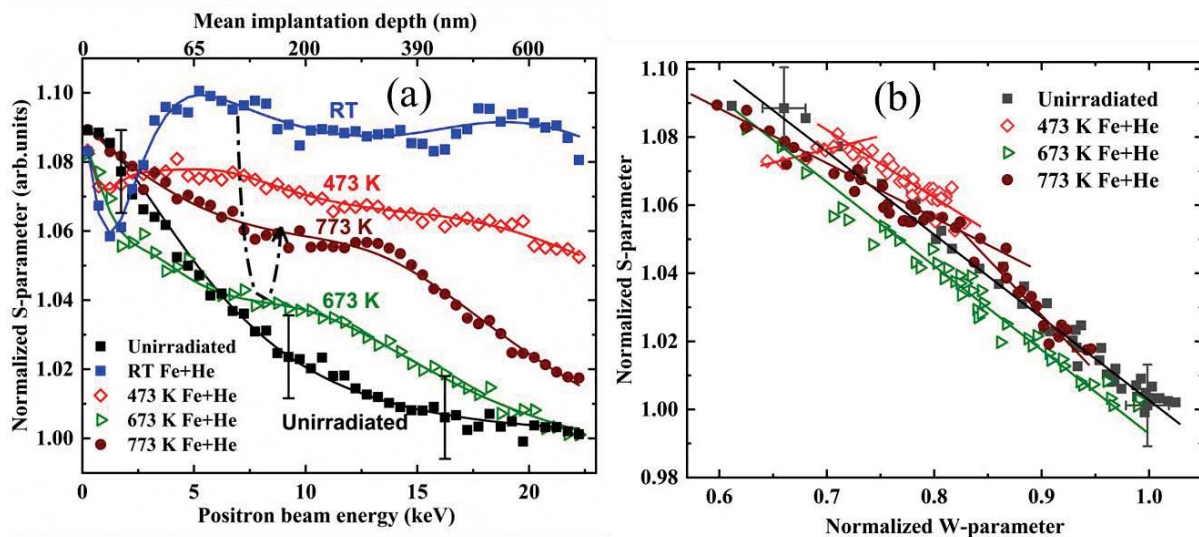


Figure 5.20 a) Normalized S-parameter vs. positron beam energy and b) S-W correlation plots of INRAFM steel samples pre-injected with helium and then with Fe ions at high-temperatures (Plot of RT irradiated sample is omitted from the S-W correlation due to scattering of data points). The overall change in S-parameter with respect to temperature is shown using a curved line with an arrow in figure (a).

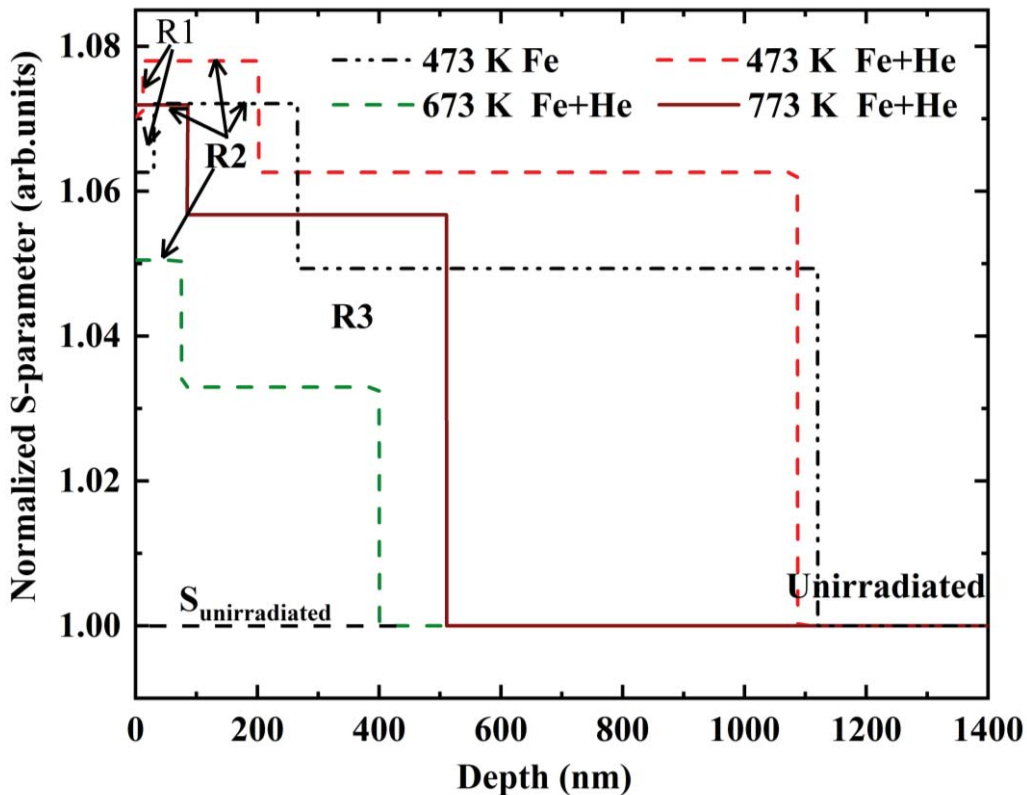


Figure 5.21 Normalized S-parameter vs. depth plot of the samples irradiated at high temperatures obtained from VEPFIT analysis. Samples with pre-injected helium are represented as Fe+He. The sample without pre-injected helium and irradiated at 473 K is represented as 473 K Fe. (RT irradiated sample data is omitted since it is already discussed in section 5.3.2).

The normalized S-parameter vs. depth plot of samples irradiated at high temperatures with pre-injected He (represented as Fe+He), and the sample irradiated at 473 K without pre-injected He (represented as 473 K Fe) is shown in figure 5.21. Samples irradiated at 473 K shows four layers- R1, R2, R3 and an unirradiated layer whereas other samples show only three layers. The narrow near-surface layer R1 is absent in 673 and 773 K samples. The narrow layer R1 shown by 473 K samples are due to the dip in S-parameter at the near-surface region. The 473 K Fe+He sample shows a higher S-parameter in the R2 and R3 regions as compared to the 473 K Fe sample. This is because, the pre-injected He atoms stabilize the vacancies produced by Fe irradiation, and prevents them from vacancy-interstitial recombination or their migration towards sinks. The higher number of surviving vacancies (in the form of He_mV_n complexes) makes the S-parameter of Fe+He sample high as compared to the Fe-irradiated sample at 473 K. The width shown by R2 and R3 regions of Fe and Fe+He samples are almost similar at 473K. Further increase in irradiation temperature to 673 K decreases both S-parameter and width of R2 and R3 regions in Fe+He sample due to

defect annealing. Helium bubble growth increases the S-parameter of R2 and R3 layers at 773 K in Fe+He sample. Increase in width of R3 region at 773 K is due to the enhanced migration of smaller He_mV_n clusters or bubbles at higher temperatures.

5.4. Conclusion

In this chapter, defect studies in INRAFM steel samples were carried out by irradiating with 1.1 MeV Fe ions at i) room temperature to different doses from 0.1 to 100 dpa followed by isochronal annealing and ii) high-temperatures with and without pre-injected helium. The irradiation-induced microstructural changes in room temperature irradiated samples were studied using GIXRD, Nanoindentation, and depth-resolved positron Doppler broadening spectroscopy. The positron annihilation studies show a non-uniform defect distribution in INRAFM steel, which is different from the SRIM predicted damage profile. At 0.1 dpa dose, the post-irradiation isochronal annealing study showed a stable S-parameter region from 673 to 873 K due to the formation of secondary carbide precipitates and complete defect recovery observed at 1073 K. At higher irradiation doses (30 to 100 dpa), a reduction in vacancy concentration at the peak damage region due to injected-interstitial effect is observed in the positron annihilation study. The widening of injected-interstitial effect dominating region towards the end of ion range is observed with increase in the dose. The GIXRD study shows the presence of tensile micro-strain in both unirradiated and irradiated samples. As the irradiation dose is increased, the micro-strain increases due to the increase in irradiation-induced defects. The presence of irradiation-induced defects increases nanohardness at low doses, whereas the defect recovery due to injected-interstitial effect decreases the overall nanohardness of the matrix at higher doses. The defect recovery under isochronal annealing in both 1 dpa and 100 dpa irradiated samples were studied, and complete defect recovery was observed in both the samples at 673 K, irrespective of the dose.

High-temperature irradiation studies show a reduction in S-parameter due to the annealing of irradiation-induced defects in the absence of pre-injected helium. Complete defect recovery is observed at 673 K in the absence of pre-injected helium. Helium stabilizes the vacancies against vacancy-interstitial recombination and enhances the growth of bubbles. A defect annealing stage at 473 K, bubble nucleation at 673 K and the growth of helium bubbles at 773 K is observed with pre-injection of helium followed by high- temperature irradiation with Fe ions. The S-W correlation plot indicates the presence of He_mV_n complexes with similar m/n ratio during the bubble nucleation stage at 673 K.

Chapter 6

Summary and future scope

6.1. Summary of the thesis

Reduced Activation Ferritic/Martensitic (RAFM) steels have been considered as a potential candidate for the structural material of first-wall plasma-facing materials in fusion reactors. In the present thesis, irradiation damage studies were carried out on Indian Reduced Activation Ferritic/Martensitic (INRAFM) steel, which has been considered as the core structural material for Indian Lead-Lithium Ceramic cooled Test Blanket Module (LLCB-TBM) in International Thermonuclear Experimental Research (ITER) situated in France. In fusion reactors, high displacement damage induced by 14 MeV fusion neutrons is associated with large amount of hydrogen and helium, which deteriorate the favourable mechanical properties and leads to premature failure of core structural materials. Defects and defect-complexes that are induced in INRAFM steel by irradiation that are relevant to fusion reactor first-wall conditions have been studied using positron beam based Doppler broadening spectroscopy.

Nucleation and growth studies of helium bubbles in INRAFM steel has been carried out by irradiating the sample with 130 keV helium ions to two different doses; 300 appm (low-dose) and 5600 appm (high-dose). Positron annihilation studies observed three distinct stages of annealing corresponding to defect annealing, bubble nucleation, and bubble growth. Both the doses showed similar behaviour in S-parameter variations in the defect annealing and bubble nucleation stage. The bubble nucleation stage shows similar S-parameter for both the samples irrespective of the irradiation dose. This shows that during the nucleation stage, irrespective of the irradiation dose, the nucleated helium-vacancy embryos are having similar size or helium/vacancy ratio. An increase in S-parameter due to helium bubble growth is observed in high-dose sample at 773 K whereas in low-dose sample at 973 K. TEM study on high-dose sample shows the presence of helium bubbles having an average size of ~ 1.4 nm at 773 K.

Thermal stability of hydrogen-associated defects and the interaction of hydrogen with helium-vacancy complexes is yet another concern in fusion first-wall materials. In order to study this, individual and sequential irradiations with hydrogen and helium ions have been performed on INRAFM steel samples. As compared to helium-vacancy complexes, the hydrogen-vacancy complexes are thermally unstable and dissociate at lower temperatures.

Complete recovery from hydrogen-induced defects was observed at 673 K. Even though similar displacement damage is present in both the sequential irradiated samples, the S-parameter values vary based on the sequence of irradiation. The sample irradiated with helium first and then with hydrogen shows a lower S-parameter as compared to the other one. Interaction of hydrogen with already existing helium-vacancy complexes and the formation of hydrogen-helium-vacancy complexes is one of the possibilities to explain for such a variation in S-parameter. However, the presence of hydrogen does not seem to influence helium bubble growth in the present study.

In order to simulate the high displacement damage induced by 14 MeV fusion neutrons, INRAFM steel samples were irradiated with 1.1 MeV Fe ions at doses, temperatures and He/dpa ratio equivalent to fusion first-wall conditions. Samples irradiated at room temperature shows a reduction in S-parameter at the peak damage region due to the enhanced recombination of vacancies and interstitials due to injected-interstitial effect with doses from 30 to 100 dpa. The injected-interstitial effect is an artefact of ion irradiation, which leads to a reduction in void swelling at the peak damage region. The defect recovery due to injected interstitial-effect increases the coherent-domain size in GIXRD measurements and reduces the nanohardness. A dose dependency on the annealing of irradiation-induced defects has also been observed in the samples. Sample irradiated to a dose of 0.1 dpa shows a delayed defect-recovery (at 1073 k) due to the formation and coarsening of additional carbide precipitates around the tempering temperature. Whereas the samples irradiated at 1 and 100 dpa shows complete defect recovery at 673 K. High-temperature irradiation studies shows that, in the absence of pre-injected helium, all the irradiation-induced defects are getting annealed out, and complete defect recovery is observed at 673 K. Presence of pre-injected helium stabilizes the vacancies and promotes the growth of helium bubbles during high-temperature irradiation. An increase in S-parameter due to helium bubble growth is observed at 773 K.

6.2. Future scope

Positron annihilation lifetime spectroscopy can provide more quantitative information on the nature and relative concentration of defect complexes associated with helium and hydrogen irradiation. Nature of defects present in different stages of annealing, helium/vacancy ratio of the critical nuclei formed during the nucleation stage, size of the bubbles formed during the growth stage etc. can be obtained from positron lifetime studies.

Hence, it is planned to carry out high energy alpha-particle irradiation on INRAFM steel, followed by an isochronal annealing study using positron annihilation spectroscopy.

In order to simulate exact fusion reactor first-wall conditions, a simultaneous dual-beam irradiation study with both helium and Fe ions is proposed. A simultaneous triple beam irradiation study using hydrogen, helium and Fe ions at fusion relevant irradiation conditions is also prospective investigation.

Another potential area to be probed is the irradiation-induced segregation of alloying elements and precipitate evolution in INRAFM steel. Since some of the carbide precipitates present in the matrix play a crucial role in high-temperature mechanical properties of the material, their tolerance against radiation damage is a matter of concern. The irradiation-induced modifications of already existing precipitates and the interaction of defects with precipitates need detailed investigation. Hence, a detailed study on the irradiated INRAFM steel samples using high-resolution transmission electron microscopy and atom probe tomography will also shed much light on this important aspect of precipitate-defect interactions.

References

- [1] P. Yvon, M. Le Flem, C. Cabet, and J.L. Seran, *Structural materials for next generation nuclear systems: Challenges and the path forward*, Nuclear Engineering and Design 294 (2015), pp. 161-169.
- [2] G.R. Odette, M.J. Alinger, and B.D. Wirth, *Recent Developments in Irradiation-Resistant Steels*, Annual Review of Materials Research 38 (2008), pp. 471-503.
- [3] A.A.F. Tavassoli, E. Diegele, R. Lindau, N. Luzginova, and H. Tanigawa, *Current status and recent research achievements in ferritic/martensitic steels*, Journal of Nuclear Materials 455 (2014), pp. 269-276.
- [4] O. Anderoglu, T.S. Byun, M. Toloczko, and S.A. Maloy, *Mechanical Performance of Ferritic Martensitic Steels for High Dose Applications in Advanced Nuclear Reactors*, Metallurgical and Materials Transactions A 44 (2013), pp. 70-83.
- [5] A.A.F. Tavassoli, *Present limits and improvements of structural materials for fusion reactors – a review*, Journal of Nuclear Materials 302 (2002), pp. 73-88.
- [6] K.L. Murty, and I. Charit, *Structural materials for Gen-IV nuclear reactors: Challenges and opportunities*, Journal of Nuclear Materials 383 (2008), pp. 189-195.
- [7] J.S. Cheon, C.B. Lee, B.O. Lee, J.P. Raison, T. Mizuno, F. Delage, and J. Carmack, *Sodium fast reactor evaluation: Core materials*, Journal of Nuclear Materials 392 (2009), pp. 324-330.
- [8] S.J. Zinkle, and G.S. Was, *Materials challenges in nuclear energy*, Acta Materialia 61 (2013), pp. 735-758.
- [9] T. Jayakumar, M.D. Mathew, K. Laha, and R. Sandhya, *Materials development for fast reactor applications*, Nuclear Engineering and Design 265 (2013), pp. 1175-1180.
- [10] R.L. Klueh, and A.T. Nelson, *Ferritic/martensitic steels for next-generation reactors*, Journal of Nuclear Materials 371 (2007), pp. 37-52.
- [11] A. Kohyama, A. Hishinuma, D.S. Gelles, R.L. Klueh, W. Dietz, and K. Ehrlich, *Low-activation ferritic and martensitic steels for fusion application*, Journal of Nuclear Materials 233–237, Part 1 (1996), pp. 138-147.
- [12] S. Saroja, A. Dasgupta, R. Divakar, S. Raju, E. Mohandas, M. Vijayalakshmi, K. Bhanu Sankara Rao, and B. Raj, *Development and characterization of advanced 9Cr*

- ferritic/martensitic steels for fission and fusion reactors*, Journal of Nuclear Materials 409 (2011), pp. 131-139.
- [13] N. Baluc, R. Schäublin, P. Spätiq, and M. Victoria, *On the potentiality of using ferritic/martensitic steels as structural materials for fusion reactors*, Nuclear Fusion 44 (2003), pp. 56-61.
- [14] S.J. Zinkle, and J.T. Busby, *Structural materials for fission & fusion energy*, Materials Today 12 (2009), pp. 12-19.
- [15] E.E. Bloom, S.J. Zinkle, and F.W. Wiffen, *Materials to deliver the promise of fusion power – progress and challenges*, Journal of Nuclear Materials 329–333, Part A (2004), pp. 12-19.
- [16] N. Baluc, *Materials for fusion power reactors*, Plasma Physics and Controlled Fusion 48 (2006), p. B165.
- [17] R. Lindau, A. Möslang, M. Rieth, M. Klimiankou, E. Materna-Morris, A. Alamo, A.A.F. Tavassoli, C. Cayron, A.M. Lancha, P. Fernandez, N. Baluc, R. Schäublin, E. Diegele, G. Filacchioni, J.W. Rensman, B.v.d. Schaaf, E. Lucon, and W. Dietz, *Present development status of EUROFER and ODS-EUROFER for application in blanket concepts*, Fusion Engineering and Design 75-79 (2005), pp. 989-996.
- [18] S. Cierjacks, K. Ehrlich, E.T. Cheng, H. Conrads, and H. Ullmaier, *High-Intensity Fast Neutron Sources and Neutron Fields for Fusion Technology and Fusion Materials Research*, Nuclear Science and Engineering 106 (1990), pp. 99-113.
- [19] K. Laha, S. Saroja, A. Moitra, R. Sandhya, M.D. Mathew, T. Jayakumar, and E. Rajendra Kumar, *Development of India-specific RAFM steel through optimization of tungsten and tantalum contents for better combination of impact, tensile, low cycle fatigue and creep properties*, Journal of Nuclear Materials 439 (2013), pp. 41-50.
- [20] L.W.G. Morgan, J. Shimwell, and M.R. Gilbert, *Isotopically enriched structural materials in nuclear devices*, Fusion Engineering and Design 90 (2015), pp. 79-87.
- [21] L. Tan, Y. Katoh, A.A.F. Tavassoli, J. Henry, M. Rieth, H. Sakasegawa, H. Tanigawa, and Q. Huang, *Recent status and improvement of reduced-activation ferritic-martensitic steels for high-temperature service*, Journal of Nuclear Materials 479 (2016), pp. 515-523.
- [22] Q. Huang, N. Baluc, Y. Dai, S. Jitsukawa, A. Kimura, J. Konys, R.J. Kurtz, R. Lindau, T. Muroga, G.R. Odette, B. Raj, R.E. Stoller, L. Tan, H. Tanigawa, A.A.F. Tavassoli, T. Yamamoto, F. Wan, and Y. Wu, *Recent progress of R&D activities on*

- reduced activation ferritic/martensitic steels*, Journal of Nuclear Materials 442 (2013), pp. S2-S8.
- [23] B. Raj, and T. Jayakumar, *Development of Reduced Activation Ferritic–Martensitic Steels and fabrication technologies for Indian test blanket module*, Journal of Nuclear Materials 417 (2011), pp. 72-76.
- [24] N. Baluc, D.S. Gelles, S. Jitsukawa, A. Kimura, R.L. Klueh, G.R. Odette, B. van der Schaaf, and J. Yu, *Status of reduced activation ferritic/martensitic steel development*, Journal of Nuclear Materials 367–370, Part A (2007), pp. 33-41.
- [25] S. Banerjee, *Overview of Indian activities on fusion reactor materials*, Journal of Nuclear Materials 455 (2014), pp. 217-224.
- [26] B. Raj, K.B.S. Rao, and A.K. Bhaduri, *Progress in the development of reduced activation ferritic-martensitic steels and fabrication technologies in India*, Fusion Engineering and Design 85 (2010), pp. 1460-1468.
- [27] Ravikirana, R. Mythili, S. Raju, S. Saroja, T. Jayakumar, and E. Rajendra Kumar, *Decomposition modes of austenite in 9Cr–W–V–Ta reduced activation ferritic–martensitic steels*, Materials Science and Technology 31 (2015), pp. 448-459.
- [28] R. Kirana, S. Raju, R. Mythili, S. Saibaba, T. Jayakumar, and E. Rajendra Kumar, *High-Temperature Phase Stability of 9Cr–W–Ta–V–C Based Reduced Activation Ferritic–Martensitic (RAFM) Steels: Effect of W and Ta Additions*, steel research international 86 (2015), pp. 825-840.
- [29] T. Jayakumar, and E. Rajendra Kumar, *Current status of technology development for fabrication of Indian Test Blanket Module (TBM) of ITER*, Fusion Engineering and Design 89 (2014), pp. 1562-1567.
- [30] R. Bhattacharyay, *Status of Indian LLCB TBM program and R&D activities*, Fusion Engineering and Design 89 (2014), pp. 1107-1112.
- [31] G.S. Was, *Fundamentals of Radiation Materials Science*, 1 ed., Springer-Verlag Berlin Heidelberg, New York, 2007.
- [32] A. Aitkaliyeva, L. He, H. Wen, B. Miller, X.M. Bai, and T. Allen, *7 - Irradiation effects in Generation IV nuclear reactor materials*, in *Structural Materials for Generation IV Nuclear Reactors*, P. Yvon ed., Woodhead Publishing, 2017, pp. 253-283.
- [33] R. Hu, G.D.W. Smith, and E.A. Marquis, *Atom probe study of radiation induced grain boundary segregation/depletion in a Fe-12%Cr alloy*, Progress in Nuclear Energy 57 (2012), pp. 14-19.

- [34] Z. Jiao, and G.S. Was, *Segregation behavior in proton- and heavy-ion-irradiated ferritic-martensitic alloys*, Acta Materialia 59 (2011), pp. 4467-4481.
- [35] V. Kuksenko, C. Pareige, P. Pareige, and Y. Dai, *Production and segregation of transmutation elements Ca, Ti, Sc in the F82H steel under mixed spectrum irradiation of high energy protons and spallation neutrons*, Journal of Nuclear Materials 447 (2014), pp. 189-196.
- [36] C. Pareige, V. Kuksenko, and P. Pareige, *Behaviour of P, Si, Ni impurities and Cr in self ion irradiated Fe-Cr alloys – Comparison to neutron irradiation*, Journal of Nuclear Materials 456 (2015), pp. 471-476.
- [37] C. Zheng, and D. Kaoumi, *Radiation-induced swelling and radiation-induced segregation & precipitation in dual beam irradiated Ferritic/Martensitic HT9 steel*, Materials Characterization 134 (2017), pp. 152-162.
- [38] A. Vehanen, P. Hautojärvi, J. Johansson, J. Yli-Kauppila, and P. Moser, *Vacancies and carbon impurities in alpha- iron: Electron irradiation*, Physical Review B 25 (1982), pp. 762-780.
- [39] Y.W. You, Y. Zhang, X. Li, Y. Xu, C.S. Liu, J.L. Chen, and G.N. Luo, *Point defect induced segregation of alloying solutes in α -Fe*, Journal of Nuclear Materials 479 (2016), pp. 11-18.
- [40] G. Amarendra, B.K. Panigrahi, S. Abhaya, C. David, R. Rajaraman, K.G.M. Nair, C.S. Sundar, and B. Raj, *Positron beam studies of void swelling in ion irradiated Ti-modified stainless steel*, Applied Surface Science 255 (2008), pp. 139-141.
- [41] C. David, B.K. Panigrahi, G. Amarendra, S. Abhaya, S. Balaji, A.K. Balamurugan, K.G.M. Nair, B. Viswanathan, C.S. Sundar, and B. Raj, *Void swelling in ion irradiated (15Ni-14Cr), Ti-modified stainless steel: A study using positron annihilation and step height measurements*, Surface and Coatings Technology 203 (2009), pp. 2363-2366.
- [42] H. Ogiwara, H. Sakasegawa, H. Tanigawa, M. Ando, Y. Katoh, and A. Kohyama, *Void swelling in reduced activation ferritic/martensitic steels under ion-beam irradiation to high fluences*, Journal of Nuclear Materials 307–311, Part 1 (2002), pp. 299-303.
- [43] M.J. Norgett, M.T. Robinson, and I.M. Torrens, *A proposed method of calculating displacement dose rates*, Nuclear Engineering and Design 33 (1975), pp. 50-54.

- [44] D. Terentyev, N. Juslin, K. Nordlund, and N. Sandberg, *Fast three dimensional migration of He clusters in bcc Fe and Fe–Cr alloys*, Journal of Applied Physics 105 (2009), p. 103509.
- [45] C.C. Fu, and F. Willaime, *Interaction between helium and self-defects in α -iron from first principles*, Journal of Nuclear Materials 367-370 (2007), pp. 244-250.
- [46] H. Trinkaus, and B.N. Singh, *Helium accumulation in metals during irradiation – where do we stand?*, Journal of Nuclear Materials 323 (2003), pp. 229-242.
- [47] C.-C. Fu, and F. Willaime, *Ab initio study of helium in alpha-Fe: Dissolution, migration, and clustering with vacancies*, Physical Review B 72 (2005), p. 064117.
- [48] H. Trinkaus, *On the modeling of the high-temperature embrittlement of metals containing helium*, Journal of Nuclear Materials 118 (1983), pp. 39-49.
- [49] B.N. Singh, and H. Trinkaus, *An analysis of the bubble formation behaviour under different experimental conditions*, Journal of Nuclear Materials 186 (1992), pp. 153-165.
- [50] H. Trinkaus, *The effect of internal pressure on the coarsening of inert gas bubbles in metals*, Scripta Metallurgica 23 (1989), pp. 1773-1778.
- [51] W.A. Counts, C. Wolverton, and R. Gibala, *First-principles energetics of hydrogen traps in α -Fe: Point defects*, Acta Materialia 58 (2010), pp. 4730-4741.
- [52] S.M. Myers, P.M. Richards, W.R. Wampler, and F. Besenbacher, *Ion-beam studies of hydrogen-metal interactions*, Journal of Nuclear Materials 165 (1989), pp. 9-64.
- [53] E. Hayward, and C.-C. Fu, *Interplay between hydrogen and vacancies in alpha-Fe*, Physical Review B 87 (2013), p. 174103.
- [54] Y. Tateyama, and T. Ohno, *Stability and clusterization of hydrogen-vacancy complexes alpha-Fe: An ab initio study*, Physical Review B 67 (2003), p. 174105.
- [55] S.M. Myers, S.T. Picraux, and R.E. Stoltz, *Defect trapping of ion-implanted deuterium in Fe*, Journal of Applied Physics 50 (1979), pp. 5710-5719.
- [56] J.K. Nørskov, F. Besenbacher, J. Bøttiger, B.B. Nielsen, and A.A. Pisarev, *Interaction of Hydrogen with Defects in Metals: Interplay between Theory and Experiment*, Physical Review Letters 49 (1982), pp. 1420-1423.
- [57] S.M. Myers, F. Besenbacher, and J. Bo/ttiger, *Deuterium in He-implanted Fe: Trapping and the surface permeation barrier*, Applied Physics Letters 39 (1981), pp. 450-452.

- [58] F. Besenbacher, J. Bottiger, and S.M. Myers, *Defect trapping of ion-implanted deuterium in nickel*, Journal of Applied Physics 53 (1982), pp. 3536-3546.
- [59] F. Besenbacher, J. Bottiger, and S.M. Myers, *Deuterium trapping in helium-implanted nickel*, Journal of Applied Physics 53 (1982), pp. 3547-3551.
- [60] K.Q. Chen, Y.S. Wang, J.M. Quan, J.G. Sun, C.H. Zhang, and Z.Y. Zhao, *The formation of helium bubbles in 316L SS irradiated with helium ions at different temperatures*, Journal of Nuclear Materials 212 (1994), pp. 345-351.
- [61] F. Kano, Y. Arai, K. Fukuya, N. Sekimura, and S. Ishino, *The effect of hydrogen on microstructural changes using dual ion irradiation*, Journal of Nuclear Materials 203 (1993), pp. 151-157.
- [62] Z.H. Luklinska, G. von Bradsky, and P.J. Goodhew, *Helium bubble growth in ferritic stainless steel*, Journal of Nuclear Materials 135 (1985), pp. 206-214.
- [63] I. Carvalho, H. Schut, A. Fedorov, N. Luzginova, and J. Sietsma, *Characterization of helium ion implanted reduced activation ferritic/martensitic steel with positron annihilation and helium thermal desorption methods*, Journal of Nuclear Materials 442 (2013), pp. S48-S51.
- [64] K. Takai, H. Shoda, H. Suzuki, and M. Nagumo, *Lattice defects dominating hydrogen-related failure of metals*, Acta Materialia 56 (2008), pp. 5158-5167.
- [65] T. Zhu, X.Z. Cao, S.X. Jin, J.P. Wu, Y.H. Gong, E.Y. Lu, B.Y. Wang, R.S. Yu, and L. Wei, *Helium retention and thermal desorption from defects in Fe9Cr binary alloys*, Journal of Nuclear Materials 466 (2015), pp. 522-525.
- [66] F. Besenbacher, J. Bottiger, and S.M. Myers, *Deuterium trapping in helium-implanted nickel*, Journal of Applied Physics 53 (1982), pp. 3547-3551.
- [67] A. Debelle, M.F. Barthe, T. Sauvage, R. Belamhawal, A. Chelgoum, P. Desgardin, and H. Labrim, *Helium behaviour and vacancy defect distribution in helium implanted tungsten*, Journal of Nuclear Materials 362 (2007), pp. 181-188.
- [68] S.K. Das, and M. Kaminsky, *Radiation blistering of structural materials for fusion devices and reactors*, Journal of Nuclear Materials 53 (1974), pp. 115-122.
- [69] M. Braun, J.L. Whitton, and B. Emmoth, *Helium induced surface exfoliation of aluminum and the correlation between flake thickness and ion energy in the range 10 – 80 keV*, Journal of Nuclear Materials 85-86 (1979), pp. 1091-1094.

- [70] M. Thompson, P. Kluth, R.P. Doerner, N. Kirby, and C. Corr, *Probing helium nanobubble formation in tungsten with grazing incidence small angle x-ray scattering*, Nuclear Fusion 55 (2015), p. 042001.
- [71] S. Fréchard, M. Walls, M. Kociak, J.P. Chevalier, J. Henry, and D. Gorse, *Study by EELS of helium bubbles in a martensitic steel*, Journal of Nuclear Materials 393 (2009), pp. 102-107.
- [72] C.A. Walsh, J. Yuan, and L.M. Brown, *A procedure for measuring the helium density and pressure in nanometre-sized bubbles in irradiated materials using electron-energy-loss spectroscopy*, Philosophical Magazine A 80 (2000), pp. 1507-1543.
- [73] G. Amarendra, B. Viswanathan, and K.P. Gopinathan, *Positron annihilation study of helium clustering in alpha irradiated copper*, Radiation Effects and Defects in Solids 118 (1991), pp. 357-369.
- [74] G. Amarendra, B. Viswanathan, A. Bharathi, and K.P. Gopinathan, *Nucleation and growth of helium bubbles in nickel studied by positron-annihilation spectroscopy*, Physical Review B 45 (1992), pp. 10231-10241.
- [75] R. Rajaraman, B. Viswanathan, M.C. Valsakumar, and K.P. Gopinathan, *Anomalous helium-bubble growth in palladium*, Physical Review B 50 (1994), pp. 597-600.
- [76] T. Ishizaki, Q. Xu, T. Yoshiie, S. Nagata, and T. Troev, *The effect of hydrogen and helium on microvoid formation in iron and nickel*, Journal of Nuclear Materials 307-311 (2002), pp. 961-965.
- [77] R.M. Hengstler-Eger, P. Baldo, L. Beck, J. Dorner, K. Ertl, P.B. Hoffmann, C. Hugenschmidt, M.A. Kirk, W. Petry, P. Pikart, and A. Rempel, *Heavy ion irradiation induced dislocation loops in AREVA's M5® alloy*, Journal of Nuclear Materials 423 (2012), pp. 170-182.
- [78] E. Gaganidze, C. Petersen, E. Materna-Morris, C. Dethloff, O.J. Weiß, J. Aktaa, A. Povstyanko, A. Fedoseev, O. Makarov, and V. Prokhorov, *Mechanical properties and TEM examination of RAFM steels irradiated up to 70 dpa in BOR-60*, Journal of Nuclear Materials 417 (2011), pp. 93-98.
- [79] K. Ono, M. Miyamoto, and K. Arakawa, *Dynamical interaction of helium bubbles with grain boundaries in Fe and Fe–9Cr ferritic alloy*, Journal of Nuclear Materials 367-370 (2007), pp. 522-526.
- [80] E. Wakai, T. Sawai, K. Furuya, A. Naito, T. Aruga, K. Kikuchi, S. Yamashita, S. Ohnuki, S. Yamamoto, H. Naramoto, and S. Jistukawa, *Effect of triple ion beams in*

- ferritic/martensitic steel on swelling behavior*, Journal of Nuclear Materials 307–311, Part 1 (2002), pp. 278-282.
- [81] H. Tanigawa, H. Sakasegawa, H. Ogiwara, H. Kishimoto, and A. Kohyama, *Radiation induced phase instability of precipitates in reduced-activation ferritic/martensitic steels*, Journal of Nuclear Materials 367-370 (2007), pp. 132-136.
- [82] H. Lefaix-Jeuland, S. Moll, F. Legendre, and F. Jomard, *SIMS depth profiling of implanted helium in pure iron using CsHe⁺ detection mode*, Nuclear Instruments and Methods in Physics Research Section B: Beam Interactions with Materials and Atoms 295 (2013), pp. 69-71.
- [83] M. Roldán, P. Fernández, J. Rams, D. Jiménez-Rey, E. Materna-Morris, and M. Klimenkov, *Comparative study of helium effects on EU-ODS EUROFER and EUROFER97 by nanoindentation and TEM*, Journal of Nuclear Materials 460 (2015), pp. 226-234.
- [84] Y. Chang, J. Zhang, X. Li, Q. Guo, F. Wan, and Y. Long, *Microstructure and nanoindentation of the CLAM steel with nanocrystalline grains under Xe irradiation*, Journal of Nuclear Materials 455 (2014), pp. 624-629.
- [85] R.E. Clausing, L. Heatherly, R.G. Faulkner, A.F. Rowcliffe, and K. Farrell, *Radiation-induced segregation in HT-9 martensitic steel*, Journal of Nuclear Materials 141-143 (1986), pp. 978-981.
- [86] Z. Jiao, and G.S. Was, *Novel features of radiation-induced segregation and radiation-induced precipitation in austenitic stainless steels*, Acta Materialia 59 (2011), pp. 1220-1238.
- [87] R. Krause-Rehberg, and H.S. Leipner, *Positron Annihilation in Semiconductors: Defect Studies*, Springer, Berlin, 1999.
- [88] P.E. Lhuillier, M.F. Barthe, P. Desgardin, W. Egger, and P. Sperr, *Positron annihilation studies on the nature and thermal behaviour of irradiation induced defects in tungsten*, physica status solidi c 6 (2009), pp. 2329-2332.
- [89] M. Eldrup, and B.N. Singh, *Study of defect annealing behaviour in neutron irradiated Cu and Fe using positron annihilation and electrical conductivity*, Journal of Nuclear Materials 276 (2000), pp. 269-277.
- [90] H. Matsui, K. Kuji, M. Hasegawa, and A. Kimura, *Effects of temperature history during neutron irradiation on the microstructure of vanadium alloys*, Journal of Nuclear Materials 212-215 (1994), pp. 784-789.

- [91] V. Sabelová, V. Kršjak, J. Kuriplach, M. Petriska, V. Slugeň, and J. Šimeg Vaterníková, *Characterization of helium implanted Fe–Cr alloys by means of positron annihilation methods*, Journal of Nuclear Materials 450 (2014), pp. 54-58.
- [92] T.M. Wang, M. Shimotomai, and M. Doyama, *Study of vacancies in the intermetallic compound Ni₃Al by positron annihilation*, Journal of Physics F: Metal Physics 14 (1984), pp. 37-45.
- [93] Y. Nagai, K. Takadate, Z. Tang, H. Ohkubo, H. Sunaga, H. Takizawa, and M. Hasegawa, *Positron annihilation study of vacancy-solute complex evolution in Fe-based alloys*, Physical Review B 67 (2003), p. 224202.
- [94] H.E. Hassan, T. Sharshar, M.M. Hessien, and O.M. Hemeda, *Effect of γ -rays irradiation on Mn–Ni ferrites: Structure, magnetic properties and positron annihilation studies*, Nuclear Instruments and Methods in Physics Research Section B: Beam Interactions with Materials and Atoms 304 (2013), pp. 72-79.
- [95] M. Lambrecht, and A. Almazouzi, *Positron annihilation study of neutron irradiated model alloys and of a reactor pressure vessel steel*, Journal of Nuclear Materials 385 (2009), pp. 334-338.
- [96] R. Harding, G. Davies, J. Tan, P.G. Coleman, C.P. Burrows, and J. Wong-Leung, *Identification by photoluminescence and positron annihilation of vacancy and interstitial intrinsic defects in ion-implanted silicon*, Journal of Applied Physics 100 (2006), p. 073501.
- [97] J. Makinen, P. Hautojarvi, and C. Corbel, *Positron annihilation and the charge states of the phosphorus-vacancy pair in silicon*, Journal of Physics: Condensed Matter 4 (1992), pp. 5137-5154.
- [98] X.D. Pi, C.P. Burrows, and P.G. Coleman, *Fluorine in Silicon: Diffusion, Trapping, and Precipitation*, Physical Review Letters 90 (2003), p. 155901.
- [99] J.C. Bourgoin, H.J. von Bardeleben, and D. Stievenard, *Irradiation Induced Defects in III–V Semiconductor Compounds*, physica status solidi (a) 102 (1987), pp. 499-510.
- [100] A. Kawasuso, H. Itoh, T. Ohshima, K. Abe, and S. Okada, *Vacancy production by 3 MeV electron irradiation in 6H-SiC studied by positron lifetime spectroscopy*, Journal of Applied Physics 82 (1997), pp. 3232-3238.
- [101] L.J. Cheng, and C.K. Yeh, *Positron lifetimes in proton-irradiated silicon*, Solid State Communications 12 (1973), pp. 529-531.

- [102] V. Balitska, Y. Shpotyuk, J. Filipecki, O. Shpotyuk, and M. Iovu, *Post-irradiation relaxation in vitreous arsenic/antimony trisulphides*, Journal of Non-Crystalline Solids 357 (2011), pp. 487-489.
- [103] O.I. Shpotyuk, J. Filipecki, A. Kozdras, and T.S. Kavetskyy, *Radiation-induced defect formation in chalcogenide glasses*, Journal of Non-Crystalline Solids 326-327 (2003), pp. 268-272.
- [104] Y. Fukumoto, A. Ishii, A. Iwase, Y. Yokoyama, and F. Hori, *Behavior of free volume in ZrCuAl bulk metallic glass after irradiation*, Journal of Physics: Conference Series 225 (2010), p. 012010.
- [105] F. Hori, N. Onodera, Y. Fukumoto, A. Ishii, A. Iwase, A. Kawasuso, A. Yabuuchi, M. Maekawa, and Y. Yokoyama, *A study of defects in electron- and ion-irradiated ZrCuAl bulk glassy alloy using positron annihilation techniques*, Journal of Physics: Conference Series 262 (2011), p. 012025.
- [106] V.M. Shkapa, A.M. Shalaev, V.V. Polotnjuk, S.P. Likhtorovich, V.V. Nemoshkalenko, and V.V. Kotov, *Positron, Mössbauer and NMR studies of γ -irradiated FeCoB metallic glasses*, Journal of Non-Crystalline Solids 155 (1993), pp. 90-94.
- [107] Y. Kobayashi, I. Kojima, S. Hishita, T. Suzuki, E. Asari, and M. Kitajima, *Damage-depth profiling of an ion-irradiated polymer by monoenergetic positron beams*, Physical Review B 52 (1995), pp. 823-828.
- [108] T. Suzuki, Y. Oki, M. Numajiri, T. Miura, K. Kondo, N. Oshima, and Y. Ito, *Radiation effect on polypropylene studied by the relaxational behaviour at low temperature using positron annihilation*, Polymer 37 (1996), pp. 5521-5524.
- [109] A. Buttafava, G. Consolati, L. Di Landro, and M. Mariani, *γ -Irradiation effects on polyethylene terephthalate studied by positron annihilation lifetime spectroscopy*, Polymer 43 (2002), pp. 7477-7481.
- [110] Ismayil, V. Ravindrachary, R.F. Bhajantri, S.D. Praveena, B. Poojary, D. Dutta, and P.K. Pujari, *Optical and microstructural studies on electron irradiated PMMA: A positron annihilation study*, Polymer Degradation and Stability 95 (2010), pp. 1083-1091.
- [111] R. Ramani, and C. Ranganathaiah, *Degradation of acrylonitrile-butadiene-styrene and polycarbonate by UV irradiation*, Polymer Degradation and Stability 69 (2000), pp. 347-354.

- [112] A. Harisha, V. Ravindrachary, R.F. Bhajantri, Ismayil, G. Sanjeev, B. Poojary, D. Dutta, and P.K. Pujari, *Electron irradiation induced microstructural modifications in BaCl₂ doped PVA: A positron annihilation study*, Polymer Degradation and Stability 93 (2008), pp. 1554-1563.
- [113] S.K. Sharma, P. Maheshwari, D. Dutta, K. Sudarshan, and P.K. Pujari, *Modification of microstructure of the surface and the bulk in ion-irradiated membrane studied using positron annihilation spectroscopy*, Radiation Physics and Chemistry 79 (2010), pp. 1115-1119.
- [114] T. Iwai, and H. Tsuchida, *In situ positron beam Doppler broadening measurement of ion-irradiated metals – Current status and potential*, Nuclear Instruments and Methods in Physics Research Section B: Beam Interactions with Materials and Atoms 285 (2012), pp. 18-23.
- [115] T. Iwai, K. Murakami, T. Iwata, and Y. Katano, *Defect formation in iron by MeV ion beam investigated with a positron beam and electrical resistivity measurement*, Nuclear Instruments and Methods in Physics Research Section B: Beam Interactions with Materials and Atoms 315 (2013), pp. 153-156.
- [116] A. Kinomura, R. Suzuki, T. Ohdaira, N. Oshima, B.E. O'Rourke, and T. Nishijima, *Development of a Slow Positron Beam System for in-situ Lifetime Measurements During Ion Beam Irradiation*, Physics Procedia 35 (2012), pp. 111-116.
- [117] K. Petersen, N. Thrane, and R.M.J. Cotterill, *A positron annihilation study of the annealing of, and void formation in, neutron-irradiated molybdenum*, The Philosophical Magazine: A Journal of Theoretical Experimental and Applied Physics 29 (1974), pp. 9-23.
- [118] M. Eldrup, J.H. Evans, O.E. Mogensen, and B.N. Singh, *A positron annihilation investigation of defects in neutron irradiated copper*, Radiation Effects 54 (1981), pp. 65-80.
- [119] M. Eldrup, and B.N. Singh, *Accumulation of point defects and their complexes in irradiated metals as studied by the use of positron annihilation spectroscopy – a brief review*, Journal of Nuclear Materials 323 (2003), pp. 346-353.
- [120] S. Mantl, and W. Triftshäuser, *Defect annealing studies on metals by positron annihilation and electrical resistivity measurements*, Physical Review B 17 (1978), pp. 1645-1652.

- [121] B. Lengeler, S. Mantl, and W. Triftshauser, *Interaction of hydrogen and vacancies in copper investigated by positron annihilation*, Journal of Physics F: Metal Physics 8 (1978), pp. 1691-1698.
- [122] P. Hautojärvi, and J. Yli-Kauppila, *Positron annihilation in amorphous metals*, Nuclear Instruments and Methods in Physics Research 199 (1982), pp. 75-86.
- [123] C.L. Snead, A.N. Goland, and F.W. Wiffen, *Tracing the evolution of bubbles in helium-injected aluminum by means of positron annihilation*, Journal of Nuclear Materials 64 (1977), pp. 195-205.
- [124] T. Troev, E. Popov, P. Staikov, and N. Nankov, *Positron lifetime studies of defects in α -Fe containing helium*, physica status solidi c 6 (2009), pp. 2373-2375.
- [125] P.M.G. Nambissan, P. Sen, and B. Viswanathan, *Helium bubbles in molybdenum investigated by positron annihilation spectroscopy*, Radiation Effects and Defects in Solids 116 (1991), pp. 125-135.
- [126] S.V. Naidu, A. Sen Gupta, and P. Sen, *Positron annihilation studies on alpha-irradiated and deformed niobium*, Journal of Nuclear Materials 148 (1987), pp. 86-91.
- [127] T. Troev, A. Markovski, S. Peneva, and T. Yoshiie, *Positron lifetime calculations of defects in chromium containing hydrogen or helium*, Journal of Nuclear Materials 359 (2006), pp. 93-101.
- [128] S. Pecko, S. Sojak, and V. Slugeň, *Comparative study of irradiated and hydrogen implantation damaged German RPV steels from PAS point of view*, Applied Surface Science 312 (2014), pp. 172-175.
- [129] M. Lambrecht, L. Malerba, and A. Almazouzi, *Influence of different chemical elements on irradiation-induced hardening embrittlement of RPV steels*, Journal of Nuclear Materials 378 (2008), pp. 282-290.
- [130] G. Brauer, L. Liszkay, B. Molnar, and R. Krause, *Microstructural aspects of neutron embrittlement of reactor pressure vessel steels - A view from positron annihilation spectroscopy*, Nuclear Engineering and Design 127 (1991), pp. 47-68.
- [131] J. Jiang, Y.C. Wu, X.B. Liu, R.S. Wang, Y. Nagai, K. Inoue, Y. Shimizu, and T. Toyama, *Microstructural evolution of RPV steels under proton and ion irradiation studied by positron annihilation spectroscopy*, Journal of Nuclear Materials 458 (2015), pp. 326-334.
- [132] A. Kuramoto, T. Toyama, T. Takeuchi, Y. Nagai, M. Hasegawa, T. Yoshiie, and Y. Nishiyama, *Post-irradiation annealing behavior of microstructure and hardening of a*

- reactor pressure vessel steel studied by positron annihilation and atom probe tomography*, Journal of Nuclear Materials 425 (2012), pp. 65-70.
- [133] G. Brauer, M.J. Puska, M. Sob, and T. Korhonen, *Positron affinity for precipitates in reactor pressure vessel steels*, Nuclear Engineering and Design 158 (1995), pp. 149-156.
- [134] Q. Xu, K. Fukumoto, Y. Ishi, Y. Kuriyama, T. Uesugi, K. Sato, Y. Mori, and T. Yoshiie, *Irradiation damage from low-dose high-energy protons on mechanical properties and positron annihilation lifetimes of Fe–9Cr alloy*, Journal of Nuclear Materials 468 (2016), pp. 260-263.
- [135] M. Lambrecht, and L. Malerba, *Positron annihilation spectroscopy on binary Fe–Cr alloys and ferritic/martensitic steels after neutron irradiation*, Acta Materialia 59 (2011), pp. 6547-6555.
- [136] S.S. Huang, T. Yoshiie, Q. Xu, K. Sato, and T.D. Troev, *Positron annihilation studies of electron-irradiated F82H model alloys*, Journal of Nuclear Materials 440 (2013), pp. 617-621.
- [137] W. Anwand, T. Leguey, M. Scepanovic, F.J. Sanchez, I. García-Cortés, and A. Wagner, *Fe+ Implantation Induced Damage in Oxide Dispersion Strengthened Steels Investigated by Doppler Broadening Spectroscopy*, Defect and Diffusion Forum 373 (2017), pp. 113-116.
- [138] M. Šćepanović, V. de Castro, T. Leguey, M.A. Auger, S. Lozano-Perez, and R. Pareja, *Microstructural stability of ODS Fe–14Cr (–2W–0.3Ti) steels after simultaneous triple irradiation*, Nuclear Materials and Energy 9 (2016), pp. 490-495.
- [139] Y. Xin, X. Ju, J. Qiu, L. Guo, J. Chen, Z. Yang, P. Zhang, X. Cao, and B. Wang, *Vacancy-type defects and hardness of helium implanted CLAM steel studied by positron-annihilation spectroscopy and nano-indentation technique*, Fusion Engineering and Design 87 (2012), pp. 432-436.
- [140] Q. Cao, X. Ju, L. Guo, and B. Wang, *Helium-implanted CLAM steel and evolutionary behavior of defects investigated by positron-annihilation spectroscopy*, Fusion Engineering and Design 89 (2014), pp. 1101-1106.
- [141] I. Carvalho, H. Schut, A. Fedorov, N. Luzginova, P. Desgardin, and J. Sietsma, *Helium implanted Eurofer97 characterized by positron beam Doppler broadening and Thermal Desorption Spectroscopy*, Journal of Nuclear Materials 442 (2013), pp. 377-381.
- [142] Z. James, *The Stopping and Range of Ions in Matter*, 2013, pp. www.srim.org.

- [143] G. Amarendra, B. Viswanathan, G.V. Rao, J. Parimala, and B. Purniah, *Variable Energy Slow Positron Beams for Depth Resolved Defect Spectroscopy in Thin film Structures*, Current Science 73 (1997), pp. 409-417.
- [144] J. Parimala, S. Abhaya, R. Ramachandran, R. Rajaraman, and G. Amarendra, *Automation of variable low energy positron beam experiments using LabVIEW based program*, 14th biennial DAE-BRNS symposium on nuclear and radiochemistry (NUCAR 2019), Mumbai, India, 2019.
- [145] A. van Veen, H. Schut, M. Clement, J.M.M. de Nijs, A. Kruseman, and M.R. Ijpma, *VEPFIT applied to depth profiling problems*, Applied Surface Science 85 (1995), pp. 216-224.
- [146] A.M. Belu, D.J. Graham, and D.G. Castner, *Time-of-flight secondary ion mass spectrometry: techniques and applications for the characterization of biomaterial surfaces*, Biomaterials 24 (2003), pp. 3635-3653.
- [147] B. Mario, *Thin Film Analysis by X-ray Scattering*, Wiley-VCH Verlag GmbH & Co. KGaA, Weinheim, Germany, 2006.
- [148] W.C. Oliver, and G.M. Pharr, *Measurement of hardness and elastic modulus by instrumented indentation: Advances in understanding and refinements to methodology*, Journal of Materials Research 19 (2004), pp. 3-20.
- [149] X. Li, and B. Bhushan, *A review of nanoindentation continuous stiffness measurement technique and its applications*, Materials Characterization 48 (2002), pp. 11-36.
- [150] G.M. Pharr, and A. Bolshakov, *Understanding nanoindentation unloading curves*, Journal of Materials Research 17 (2002), pp. 2660-2671.
- [151] D. R.Olander, *Fundamental Aspects of Nuclear Reactor Fuel elements*, Technical Information Center, Office of Public Affairs, Energy Research and Development Administration, United States of America, 1976.
- [152] B.N. Singh, T. Leffers, W.V. Green, and M. Victoria, *Nucleation of helium bubbles on dislocations, dislocation networks and dislocations in grain boundaries during 600 MeV proton irradiation of aluminium*, Journal of Nuclear Materials 125 (1984), pp. 287-297.
- [153] K.Y. Yu, Y. Liu, C. Sun, H. Wang, L. Shao, E.G. Fu, and X. Zhang, *Radiation damage in helium ion irradiated nanocrystalline Fe*, Journal of Nuclear Materials 425 (2012), pp. 140-146.

- [154] R. Rajaraman, G. Amarendra, B. Viswanathan, C.S. Sundar, and K.P. Gopinathan, *Suppression of helium bubble growth in palladium by prior cold working*, Journal of Nuclear Materials 231 (1996), pp. 55-62.
- [155] Y.P. Wei, P.P. Liu, Y.M. Zhu, Z.Q. Wang, F.R. Wan, and Q. Zhan, *Evaluation of irradiation hardening and microstructure evolution under the synergistic interaction of He and subsequent Fe ions irradiation in CLAM steel*, Journal of Alloys and Compounds 676 (2016), pp. 481-488.
- [156] B. Kaiser, E. Gaganidze, C. Dethloff, R. Schwaiger, D. Brimbal, M. Payet, L. Beck, and J. Aktaa, *Investigation of microstructure defects in EUROFER97 under He+/Fe3+ dual ion beam irradiation*, Nuclear Materials and Energy 15 (2018), pp. 148-153.
- [157] R. Sugano, K. Morishita, A. Kimura, H. Iwakiri, and N. Yoshida, *Microstructural evolution in Fe and Fe-Cr model alloys after He+ ion irradiations*, Journal of Nuclear Materials 329–333, Part B (2004), pp. 942-946.
- [158] A. Kimura, R. Kasada, R. Sugano, A. Hasegawa, and H. Matsui, *Annealing behavior of irradiation hardening and microstructure in helium-implanted reduced activation martensitic steel*, Journal of Nuclear Materials 283–287, Part 2 (2000), pp. 827-831.
- [159] A. Kimura, R. Sugano, Y. Matsushita, and S. Ukai, *Thermal helium desorption behavior in advanced ferritic steels*, Journal of Physics and Chemistry of Solids 66 (2005), pp. 504-508.
- [160] G. Dobmann, S.N. Korshunov, M. Kroening, Y.V. Martynenko, I.D. Skorlupkin, and A.S. Surkov, *Helium and radiation defect accumulation in metals under stress*, Vacuum 82 (2008), pp. 856-866.
- [161] A. Vehanen, P. Hautojärvi, J. Johansson, J. Yli-Kauppila, and P. Moser, *Vacancies and carbon impurities in α -iron: Electron irradiation*, Physical Review B 25 (1982), pp. 762-780.
- [162] H.B. Sata, *Positron annihilation studies of model Fe-Cr alloys and ferritic/martensitic steels*. PhD thesis, Homi Bhabha National Institute, 2013.
- [163] C.-C. Fu, and F. Willaime, *Ab initio*, Physical Review B 72 (2005), p. 064117.
- [164] K. Morishita, R. Sugano, B.D. Wirth, and T. Diaz de la Rubia, *Thermal stability of helium-vacancy clusters in iron*, Nuclear Instruments and Methods in Physics Research Section B: Beam Interactions with Materials and Atoms 202 (2003), pp. 76-81.

- [165] V.A. Borodin, and P.V. Vladimirov, *Diffusion coefficients and thermal stability of small helium–vacancy clusters in iron*, Journal of Nuclear Materials 362 (2007), pp. 161-166.
- [166] V. Borodin, and P. Vladimirov, *Kinetic properties of small He–vacancy clusters in iron*, Journal of Nuclear Materials 386-388 (2009), pp. 106 - 108.
- [167] J. Knaster, A. Moeslang, and T. Muroga, *Materials research for fusion*, Nat Phys 12 (2016), pp. 424-434.
- [168] T. Zhu, S. Jin, L. Guo, Y. Hu, E. Lu, J. Wu, B. Wang, L. Wei, and X. Cao, *Helium/hydrogen synergistic effect in reduced activation ferritic/martensitic steel investigated by slow positron beam*, Philosophical Magazine 96 (2016), pp. 253-260.
- [169] V.V. Kirsanov, M.V. Musina, and V.V. Rybin, *The influence of hydrogen on the formation of helium vacancy voids in metal*, Journal of Nuclear Materials 191–194, Part B (1992), pp. 1318-1322.
- [170] T. Tanaka, K. Oka, S. Ohnuki, S. Yamashita, T. Suda, S. Watanabe, and E. Wakai, *Synergistic effect of helium and hydrogen for defect evolution under multi-ion irradiation of Fe–Cr ferritic alloys*, Journal of Nuclear Materials 329–333, Part A (2004), pp. 294-298.
- [171] J. Marian, T. Hoang, M. Fluss, and L.L. Hsiung, *A review of helium–hydrogen synergistic effects in radiation damage observed in fusion energy steels and an interaction model to guide future understanding*, Journal of Nuclear Materials 462 (2015), pp. 409-421.
- [172] W. Hu, L. Guo, J. Chen, F. Luo, T. Li, Y. Ren, J. Suo, and F. Yang, *Synergistic effect of helium and hydrogen for bubble swelling in reduced-activation ferritic/martensitic steel under sequential helium and hydrogen irradiation at different temperatures*, Fusion Engineering and Design 89 (2014), pp. 324-328.
- [173] Y. Wen, S. Jin, Z. Yang, F. Luo, Z. Zheng, L. Guo, and J. Suo, *Positron beam Doppler broadening spectra and nano-hardness study on helium and hydrogen irradiated RAFM steel*, Radiation Physics and Chemistry 107 (2015), pp. 19-22.
- [174] J. Yu, X. Zhao, W. Zhang, W. Yang, and F. Chu, *Defect production and accumulation under hydrogen and helium ion irradiation*, Journal of Nuclear Materials 251 (1997), pp. 150-156.
- [175] E. Abramov, and D. Eliezer, *Trapping of hydrogen in helium-implanted metals*, Journal of Materials Science Letters 7 (1988), pp. 108-110.

- [176] S.M. Myers, D.M. Follstaedt, F. Besenbacher, and J. Bottiger, *Trapping and surface permeation of deuterium in He-implanted Fe*, Journal of Applied Physics 53 (1982), pp. 8734-8744.
- [177] W. Zhang, F. Luo, Y. Yu, Z. Zheng, Z. Shen, L. Guo, Y. Ren, and J. Suo, *Synergistic effects on dislocation loops in reduced-activation martensitic steel investigated by single and sequential hydrogen/helium ion irradiation*, Journal of Nuclear Materials 479 (2016), pp. 302-306.
- [178] D. Erin Hayward and Chaitanya, *Energetics of small hydrogen–vacancy clusters in bcc iron*, Journal of Physics: Condensed Matter 23 (2011), p. 425402.
- [179] V.A. Borodin, and P.V. Vladimirov, *Kinetic properties of small He–vacancy clusters in iron*, Journal of Nuclear Materials 386-388 (2009), pp. 106-108.
- [180] D.M.F. S. M. Myers, F. Besenbacher, and J. Bottiger, *Trapping and surface permeation of deuterium in He-implanted Fe*, Journal of Applied Physics 53 (1982), pp. 8734-8744.
- [181] J. Shi, and N. Hashimoto, *Study on synergistic effects of H and He in α -Fe*, Nuclear Materials and Energy 16 (2018), pp. 212-216.
- [182] Y.-L. Liu, Y. Zhang, H.-B. Zhou, G.-H. Lu, F. Liu, and G.N. Luo, *Vacancy trapping mechanism for hydrogen bubble formation in metal*, Physical Review B 79 (2009), p. 172103.
- [183] S. Linderoth, and A.V. Shishkin, *Hydrogen interactions with defects in Fe*, Philosophical Magazine A 55 (1987), pp. 291-300.
- [184] R. Ramachandran, S. Chakravarty, S. Balaji, P. Panda, C. David, R. Rajaraman, R. Ramaseshan, R. Govindaraj, and G. Amarendra, *Study of vacancy defects and their thermal stability in MeV Fe ion irradiated RAFM steel using positron beam Doppler broadening spectroscopy*, Philosophical Magazine (2018), pp. 1-17.
- [185] D. Erin Hayward and Chaitanya, *Synergistic effects in hydrogen–helium bubbles*, Journal of Physics: Condensed Matter 24 (2012), p. 265402.
- [186] H. Tanigawa, K. Shiba, A. Möslang, R.E. Stoller, R. Lindau, M.A. Sokolov, G.R. Odette, R.J. Kurtz, and S. Jitsukawa, *Status and key issues of reduced activation ferritic/martensitic steels as the structural material for a DEMO blanket*, Journal of Nuclear Materials 417 (2011), pp. 9-15.
- [187] S. Jitsukawa, A. Kimura, A. Kohyama, R.L. Klueh, A.A. Tavassoli, B. van der Schaaf, G.R. Odette, J.W. Rensman, M. Victoria, and C. Petersen, *Recent results of*

- the reduced activation ferritic/martensitic steel development*, Journal of Nuclear Materials 329–333, Part A (2004), pp. 39-46.
- [188] H. Tanigawa, H. Sakasegawa, N. Hashimoto, R.L. Klueh, M. Ando, and M.A. Sokolov, *Irradiation effects on precipitation and its impact on the mechanical properties of reduced-activation ferritic/martensitic steels*, Journal of Nuclear Materials 367–370, Part A (2007), pp. 42-47.
- [189] I. Sacksteder, H.C. Schneider, and E. Materna-Morris, *Determining irradiation damage and recovery by instrumented indentation in RAFM steel*, Journal of Nuclear Materials 417 (2011), pp. 127-130.
- [190] C. Dethloff, E. Gaganidze, and J. Aktaa, *Microstructural defects in EUROFER 97 after different neutron irradiation conditions*, Nuclear Materials and Energy 9 (2016), pp. 471-475.
- [191] D. Christian, G. Ermile, and A. Jarir, *Quantitative TEM analysis of precipitation and grain boundary segregation in neutron irradiated EUROFER97*, Journal of Nuclear Materials 454 (2014), pp. 323-331.
- [192] L. Tan, T.S. Byun, Y. Katoh, and L.L. Snead, *Stability of MX-type strengthening nanoprecipitates in ferritic steels under thermal aging, stress and ion irradiation*, Acta Materialia 71 (2014), pp. 11-19.
- [193] Y. Dai, G.S. Bauer, F. Carsughi, H. Ullmaier, S.A. Maloy, and W.F. Sommer, *Microstructure in Martensitic Steel DIN 1.4926 after 800 MeV proton irradiation*, Journal of Nuclear Materials 265 (1999), pp. 203-207.
- [194] M.P. Short, D.R. Gaston, M. Jin, L. Shao, and F.A. Garner, *Modeling injected interstitial effects on void swelling in self-ion irradiation experiments*, Journal of Nuclear Materials 471 (2016), pp. 200-207.
- [195] L.K. Mansur, and M.H. Yoo, *Advances in the theory of swelling in irradiated metals and alloys*, Journal of Nuclear Materials 85 (1979), pp. 523-532.
- [196] J. Wang, M.B. Toloczko, N. Bailey, F.A. Garner, J. Gigax, and L. Shao, *Modification of SRIM-calculated dose and injected ion profiles due to sputtering, injected ion buildup and void swelling*, Nuclear Instruments and Methods in Physics Research Section B: Beam Interactions with Materials and Atoms 387 (2016), pp. 20-28.
- [197] L. Shao, C.C. Wei, J. Gigax, A. Aitkaliyeva, D. Chen, B.H. Sencer, and F.A. Garner, *Effect of defect imbalance on void swelling distributions produced in pure iron irradiated with 3.5 MeV self-ions*, Journal of Nuclear Materials 453 (2014), pp. 176-181.

- [198] V. Ragunanthan, S.H. Babu, V.A. Chirayath, R. Rajaraman, G. Amarendra, S. Saroja, C.S. Sundar, A. Alamo, and B. Raj, *Positron annihilation studies on 9Cr reduced activation ferritic/martensitic steels*, physica status solidi c 6 (2009), pp. 2307-2309.
- [199] A.D. Brailsford, and L.K. Mansur, *Effect of self-ion injection in simulation studies of void swelling*, Journal of Nuclear Materials 71 (1977), pp. 110-116.
- [200] F.A. Garner, *Impact of the injected interstitial on the correlation of charged particle and neutron-induced radiation damage*, Journal of Nuclear Materials 117 (1983), pp. 177-197.
- [201] W.D. Nix, and H. Gao, *Indentation size effects in crystalline materials: A law for strain gradient plasticity*, Journal of the Mechanics and Physics of Solids 46 (1998), pp. 411-425.
- [202] Y.V. Milman, A.A. Golubenko, and S.N. Dub, *Indentation size effect in nanohardness*, Acta Materialia 59 (2011), pp. 7480-7487.
- [203] O. Tissot, C. Pareige, E. Meslin, B. Décamps, and J. Henry, *Influence of injected interstitials on α' precipitation in Fe–Cr alloys under self-ion irradiation*, Materials Research Letters 5 (2017), pp. 117-123.

ABSTRACT

Reduced Activation Ferritic/Martensitic (RAFM) steels have been considered as a promising candidate for the first-wall structural materials of fusion reactors due to their low-induced radioactivity and exceptional resistance against irradiation damage. Indian Reduced Activation Ferritic/ Martensitic (INRAFM) steel has been developed in India as a proposed candidate for the structural material of Indian Lead-Lithium Ceramic Breeder Test Blanket Module (LLCB-TBM) in International Thermonuclear Experimental Research (ITER) situated in France. Severe displacement damage of the order of 20-30 dpa/year is introduced into the first-wall materials by 14 MeV fusion neutrons. Apart from this, large amount of hydrogen and helium at the rate of 40-50 appm H/dpa and 10-15 appm He/dpa have also been introduced by nuclear transmutation reactions and fusion plasma. Helium promotes the growth of voids by stabilizing the irradiation-induced vacancies, which leads to void swelling and premature failure of the material. In fusion reactors, hydrogen interacts with helium-vacancy complexes and promotes void swelling. Synergistic effect of irradiation-induced vacancies, hydrogen and helium, is having detrimental effects on the first-wall materials of fusion reactors. Investigation of defects and defect-complexes induced by helium and hydrogen irradiation, helium bubble nucleation and growth, thermal stability of hydrogen associated defects, interaction of hydrogen with helium-vacancy complexes and its influence in promoting helium bubble growth are the prime focus of this thesis. Positron beam based Doppler broadening spectroscopy has been used as a major technique to carry out the study of depth profiling of irradiation-induced defects.

In order to study the dependence of the nucleation and growth of helium bubbles on irradiation dose, INRAFM samples were irradiated with two different helium doses of 5600 appm (high-dose) and 300 appm (low-dose). Isochronal annealing study of helium irradiated samples show three different S-parameter regions corresponding to defect annealing, bubble nucleation, and bubble growth stages. The defect annealing stage is associated with a reduction in S-parameter due to the increase in helium/vacancy ratio associated with the formation of He_mV_n complexes. The bubble nucleation stage shows similar S-parameter values, irrespective of the irradiation dose, which is due to the presence of He_mV_n embryos having similar m/n ratio. Helium bubble growth is associated with an increase in S-parameter at 773 K in high-dose sample, whereas at 973 K in low-dose sample. The delayed bubble growth in low-dose sample is due to lesser number of helium and vacancies available for

bubble growth. TEM study showed the presence of helium bubbles having size around 1.4 nm at 773 K in high-dose sample.

Formation of hydrogen-helium-vacancy complexes has been studied by performing individual and sequential irradiations with hydrogen and helium ions on INRAFM samples. The hydrogen irradiated sample showed an increase in S-parameter from RT to 373 K due to the release of hydrogen from H_mV_n complexes having high hydrogen to vacancy ratio. Complete defect-recovery is observed in hydrogen irradiated sample at 673 K. Even though both sequential irradiated samples contain an equal amount of displacement damage (dpa), the S-parameter showed a dependency on the sequence of ion irradiation. A reduced S-parameter is observed in the sample irradiated with helium first and then with hydrogen, which may be due to the formation of hydrogen-helium-vacancy complexes. However, the isochronal annealing study does not show any influence of hydrogen in the growth of helium bubbles. Helium bubble growth occurred in all helium containing samples at 773 K.

Vacancy-type defects induced by irradiation, their thermal stability and the influence of helium at irradiation conditions relevant to first-wall of fusion reactor have been studied using Fe heavy ion irradiation. A dependency of irradiation dose on the depth-wise distribution of defects and their thermal stability has been observed. INRAFM sample irradiated to a very low dose (0.1 dpa) showed a reduction in S-parameter from RT to 673 K, followed by a stable region from 673 to 873 K associated with the nucleation and coarsening of additional carbide precipitates, and complete defect-recovery at 1073 K. The samples irradiated at 1dpa shows a higher S-parameter in the near-surface region due to vacancy clustering, on the other hand, a reduction in S-parameter at the peak-damage region due to injected-interstitial effect is observed in samples irradiated at 30, 70 and 100 dpa. VEPFIT code based analysis showed an increase in width of the region influenced by injected-interstitial effect with an increase in irradiation dose. Complete defect recovery is observed in 1 and 100 dpa sample at 673 K. High-temperature irradiation at 70 dpa without pre-injected helium showed the annealing of defects, and no growth of higher-order vacancy-type defects or voids. The sample pre-injected with 700 appm helium followed by high-temperature irradiation at 70 dpa showed the growth of helium bubbles at 773 K.

LIST OF FIGURES

- Figure 1.1** a) Specific dose rate vs. cooling time of twelve technologically important elements (reused with permission from ref [18], Copyright: Taylor and Francis (1990)) and b) variation of surface gamma dose rate with respect to cooling time for conventional austenitic steel (316L), ferritic steel (T91/P91) and different RAFM steels under fusion reactor first-wall demo conditions (reused with permission from ref [17], Copyright: Elsevier (2005)). 3
- Figure 1.2** Schematic of the a) major components and b) cross-sectional view of Indian LLCB-TBM at ITER. The figures were adopted with permission from ref [25, 29] (Copyrights: Elsevier (2014)). 6
- Figure 1.3** Schematic representation of various events caused by irradiation and their consequent effects on the performance of materials. This figure is reused with permission from ref [32] (Copyright: Elsevier (2017)). 8
- Figure 1.4** Variation of the number of displaced atoms as a function of PKA energy as predicted by the K-P model [31]. E_D is the displacement energy and E_C is the cut- off energy for electronic energy loss. 10
- Figure 1.5** Schematic representation of helium diffusion mechanisms in materials. (1) Interstitial migration of helium, (2) migration of vacancy, (3) thermally activated dissociation of a substitutional helium atom from a vacancy to the interstitial position, (4) jumping of helium from one vacancy to another, (5) replacement of substitutional helium atom from a lattice site to interstitial by a SIA atom and (6) collisional displacement of helium atom. This figure is reused with permission from ref [46] (Copyright: Elsevier (2003)). 12
- Figure 1.6** Schematic representation of the time-dependence of different quantities characterizing bubble nucleation during helium production/implantation and bubble coarsening during annealing. Here, C_{He} is the time-dependent concentration of helium atoms in the material, dN_b/dt is the nucleation rate, N_b is the density and r_b is the average size of the nucleated bubbles. Logarithmic representation is used to approximate the power-law behaviour of some individual curves to straight lines [46]. This figure is reused with permission from ref [46] (Copyright: Elsevier (2003)). 16
- Figure 1.7** Schematic representation of thermalization and diffusion of positrons in solids followed by trapping at a vacancy site. 23
- Figure 1.8** Schematic of major positron annihilation spectroscopic techniques. 24
- Figure 2.1** Schematic of the 150 keV ion accelerator used for He and H irradiations showing all major components. 32
- Figure 2.2** Schematic of 1.7 MV tandemron accelerator (M/S HVEM, Netherlands) at IGCAR, Kalpakkam. 34
- Figure 2.3** Illustration of the working principle of variable low-energy positron beam based Doppler broadening set up. 35
- Figure 2.4** a) ^{22}Na e+ emission spectrum b) interaction of e+ with a 2 μm thick W(100) thin-film moderator and (c) emission spectrum of moderated e+ from a

W(100) moderator. The figures were reused with permission from ref [87] (Copyright: Springer (1999)). 36

Figure 2.5 Photograph of the variable low-energy positron beam based Doppler broadening spectroscopic technique at IGCAR, kalpakkam [143]. 37

Figure 2.6 Implantation profile (Makhovian) of positrons into INRAFM steel at various energies. 38

Figure 2.7 Typical S-W correlation plot of a sample containing similar kind of defects. 41

Figure 2.8 Schematic illustration of a) indentation load vs. displacement curve and b) the deformation pattern of the elastic-plastic sample during and after indentation. The figures were adopted from ref [149] with permission (Copyright: Elsevier(2002)). 44

Figure 3.1 Helium ion and vacancy distribution profiles of 130 keV helium ions into INRAFM steel calculated using SRIM 2013 code. Vacancy and helium distribution peaks are shown using dotted lines. 49

Figure 3.2 Distribution of He ions into the irradiated INRAFM steel samples measured using SIMS. Peak of He distribution in the as-irradiated and 973 K samples are shown using dotted lines. 51

Figure 3.3 Normalized S-parameter vs. positron beam energy plots of as-irradiated and unirradiated reference samples. S-parameter values were normalized with respect to the unirradiated bulk value. The data points were fitted using VEPFIT programme. Positron mean implantation depth is shown on the top x-axis. The peak damage region is indicated on top axis. 52

Figure 3.4 S-W correlation plot of the as-irradiated samples. The S and W parameters were normalized with respect to the unirradiated bulk values. The unirradiated sample exhibits linear behaviour throughout the measurement depths, whereas the irradiated samples deviate from the linear trend indicating the presence of higher defect species. 54

Figure 3.5 Normalized S-parameter vs. positron beam energy plots of the low-dose samples. Positron mean implantation depth is shown along the top x-axis. The data points were fitted using VEPFIT programme. 55

Figure 3.6 The average of normalized S and W parameters from the region 360 ± 150 nm of low-dose sample is plotted against the annealing temperature. The dashed lines through the data points are just a guide to the eye. 56

Figure 3.7 Normalized S-parameter vs. positron beam energy plots of the high-dose samples. Positron mean implantation depth is shown along the top x-axis. The data points were fitted using VEPFIT programme. 57

Figure 3.8 The average S and W parameters from the depth region 360 ± 150 nm of high-dose sample is plotted as a function of annealing temperature. S and W parameters were normalized with respect to the unirradiated bulk values. The dashed lines through the data points are just an aid to the eye. 59

Figure 3.9 Normalized S-parameter vs. depth profile of (a) low-dose and (b) high-dose samples obtained from the VEPFIT analysis. Three-layer fit consists of a

| | |
|----------------------------------------------------------------------------------------------------------------------------------------------------------------------------------------------------------------------------------------------------------------------------------------------------------|----|
| surface layer, defected layer, and an unirradiated bulk was used in the VEPFIT modelling. | 60 |
| Figure 3.10 Normalized S-parameter of defected layer (deduced from VEPFIT analysis) for both doses as a function of annealing temperature is plotted for comparison. | 61 |
| Figure 3.11 Variation of width of the irradiated layer (deduced from VEPFIT analysis) of both doses as a function of the annealing temperature. | 62 |
| Figure 3.12 S-W correlation plots of (a) low-dose and (b) high-dose sample using average of normalized S and W-parameters from the region 360 ± 150 nm. | 63 |
| Figure 3.13 TEM images of the high-dose sample annealed at 773 K. Helium bubbles having an average size of around 1.4 nm are observed. The bubbles appear as white dots surrounded by a dark fringe in underfocus, and dark dots surrounded by a bright fringe in overfocus condition. | 64 |
| Figure 4.1 Distribution of total vacancies and ions into INRAFM steel calculated using SRIM 2013 code. Vacancy and ion peaks are shown using dotted lines. | 68 |
| Figure 4.2 Normalized S-parameter vs. positron beam energy plots of the unirradiated and as-irradiated samples. The data points were fitted using VEPFIT programme. Typical error bars are shown at selected data points. | 70 |
| Figure 4.3 Variation of normalized S-parameter vs. positron beam energy curves of H-irradiated samples under isochronal annealing. The data points were fitted using VEPFIT programme. | 72 |
| Figure 4.4 Variation of normalized S-parameter vs. positron beam energy curves of He-irradiated samples under isochronal annealing. The S-parameter values were normalized with respect to the unirradiated bulk value. Some of the plots were omitted from the figure for better visual clarity. | 73 |
| Figure 4.5 Variation of normalized S-parameter vs. positron beam energy curves of a) H+He-irradiated and b) He+H-irradiated samples under isochronal annealing. The S-parameter values were normalized with respect to the unirradiated bulk value. | 75 |
| Figure 4.6 Normalized S-parameter vs. depth plot of H-irradiated sample deduced from VEPFIT analysis. | 76 |
| Figure 4.7 Normalized S-parameter vs. depth plot of He-irradiated sample deduced from VEPFIT analysis. | 77 |
| Figure 4.8 Normalized S-parameter vs. depth plot of a) H+He-irradiated and b) He+H-irradiated samples deduced from VEPFIT analysis. | 78 |
| Figure 4.9 Variation of normalized S-parameter of defected region of irradiated samples deduced from VEPFIT analysis against the annealing temperature. | 79 |
| Figure 4.10 S-W correlation plot using the average of normalized S and W-parameters. | 81 |
| Figure 5.1 Vacancy and ion distribution profile of 1.1 MeV Fe ions into INRAFM steel calculated using SRIM 2013 code. Vacancy and ion peaks are shown using dotted lines. | 84 |

- Figure 5.2** GIXRD spectra of unirradiated and irradiated INRAFM samples. The individual plots are up-shifted along the Y-axis for clarity. The peaks were identified and indexed. 86
- Figure 5.3** Williamson-Hall plot of unirradiated and irradiated samples. 86
- Figure 5.4** a) Typical load profile of the nanoindentation and b) optical micrograph of the indented surface. 87
- Figure 5.5** Normalized S-parameter vs. positron beam energy plots of INRAFM steel irradiated with a dose of 0.1 dpa. The lines are fits to the experimental data using VEPFIT programme. Positron mean implantation depth is shown on the top x-axis. Typical error bars are shown for selected data points. 88
- Figure 5.6** Normalized S-parameter vs. depth plot of 0.1 dpa irradiated sample deduced from VEPFIT analysis. 89
- Figure 5.7** Variation of normalized S-parameter and width of the defected layer obtained from VEPFIT analysis (Figure 5.6) with respect to the annealing temperature. Data points are connected with dashed lines to guide the eye. Width of defected layer at 373 K does not fall in the trend shown by other temperatures due to the presence of a wider near-surface layer. 90
- Figure 5.8** S-W correlation plot of 0.1 dpa sample obtained using the average of normalized S and W-parameters. The normalized S and W values were averaged around the depth region of 310 ± 100 nm. 91
- Figure 5.9** Normalized S-parameter vs. positron beam energy plots of the unirradiated and as-irradiated samples. Experimental data points were fitted using VEPFIT programme. Positron mean implantation depth is shown on the top axis. 92
- Figure 5.10** S-W correlation plot using the average of S and W-parameters from the regions R1, R2, R3, and R4 shown in figure 5.9. 94
- Figure 5.11** Normalized S-parameter vs. depth plot of the as-irradiated samples deduced from VEPFIT analysis. 95
- Figure 5.12** Coherent domain size $\langle D \rangle v$ and micro-strain deduced from Williamson-Hall plot (figure 5.3) is plotted as a function of the irradiation dose. The dotted lines through the data points are just a guide to the eye. 97
- Figure 5.13** Nanohardness vs. indentation depth plot of the as-irradiated samples. The lines through the data points are just a guide to the eye. 99
- Figure 5.14** Variation of average of normalized S-parameter (from figure 5.9) and the average of Nanohardness from 310 ± 100 nm (from figure 5.13) region with respect to the irradiation dose. The line drawn through the data points is a guide to the eye. 100
- Figure 5.15** Normalized S-parameter vs. positron beam energy plots of a) 1 dpa and b) 100 dpa irradiated samples annealed from RT to 1073 K. The data points were fitted using VEPFIT programme. 101
- Figure 5.16** Normalized S-parameter vs. depth plot of a) 1 dpa and b) 100 dpa samples annealed from RT to 673 K. 102

Figure 5.17 Average of normalized S-parameters from regions R1, R2, R3 and R4 are plotted as a function of annealing temperature for both 1 dpa and 100 dpa samples. 103

Figure 5.18 Vacancy distribution profile of 1.1 MeV Fe ions and the distribution of helium ions into INRAFM steel calculated using SRIM 2013 code. A uniform distribution of helium ions near to the vacancy peak is obtained by implanting with He ions at energies 50, 90 and 130 keV's. 104

Figure 5.19 Normalized S-parameter vs. positron beam energy plots of INRAFM steel samples irradiated with 1.1 MeV Fe ions to 70 dpa at room temperature, 473, 673 and 773 K. The defect annealing from RT to 673 K is shown using an arrow. 105

Figure 5.20 a) Normalized S-parameter vs. positron beam energy and b) S-W correlation plots of INRAFM steel samples pre-injected with helium and then with Fe ions at high-temperatures (Plot of RT irradiated sample is omitted from the S-W correlation due to scattering of data points). The overall change in S-parameter with respect to temperature is shown using a curved line with an arrow in figure (a). 106

Figure 5.21 Normalized S-parameter vs. depth plot of the samples irradiated at high temperatures obtained from VEPFIT analysis. Samples with pre-injected helium are represented as Fe+He. The sample without pre-injected helium and irradiated at 473 K is represented as 473 K Fe. (RT irradiated sample data is omitted since it is already discussed in section 5.3.2). 107

LIST OF TABLES

Table 1.1 Composition of Indian Reduced Activation Ferritic/Martensitic (INRAFM) steel used in this study [19]. 4

Table 1.2 Approximate time scale for the production of defects under irradiation in metals. This table is adopted from ref [31] with permission (Copyright: Springer Nature (2007)). 7

